Simulation and Manufacture of Gallium Nitride Integrated Photonics

Cobi William Maynard

A thesis presented for the degree of

Doctor of Philosophy

September 2024

Abstract

This thesis presents the simulation and fabrication of gallium nitride (GaN) integrated photonic devices for use at a wavelength of 1550 nm. We have developed fabrication processes for GaN on sapphire ridge waveguides, using e-beam lithography, nickel lift-off, and inductively-coupled plasma (ICP) reactive ion etching (RIE). The simulation of waveguides allowed for the determination of waveguide widths and thicknesses for which optical modes are supported, and to identify geometries for which higher order modes are supported, as well as an investigation into the effects a non-vertical etch profile has on the waveguide modes.

Nanobeams of GaN with an equilateral triangular cross-section were simulated and found to support waveguide modes at $\lambda = 1550\,\text{nm}$, with a lateral width $w > 400\,\text{nm}$ required for optical confinement. Confined waveguide modes were found for both orthogonal TE and TM polarisations to be degenerate in effective index. This degeneracy was lifted and waveguides became birefringent when the simulated etch angle was increased or decreased, and when the waveguide had varying degrees of asymmetry introduced, showing insight into how asymmetry and etch angle affects a waveguide mode in a triangular waveguide, which are important when considering fabrication tolerances.

We have discussed the results of three-dimensional simulations of GaN photonic crystal nanobeam cavities (PCNCs), where we use Distributed Bragg Reflectors (DBRs) as mirrors in the cavity, calculating the mirror strength as a function of filling fraction using the spatial electric field profile. We compare and contrast two methods of calculating cavity Q factor, determining the ringdown method to be more accurate and appropriate than the spectral method for the simulations considered. A method of analysing the effect of loss on Q is presented using the imaginary refractive index n_i of the device, finding that Q decreases exponentially with n_i.

Acknowledgments

I would like to thank Dr. Daryl Beggs, Prof. Anthony Bennett and Prof. Michael Wale for their continued supervision and support, and to Daryl for originally sparking my interest in the world of semiconductor manufacturing with his undergraduate course. I would also like to thank Dr. JP Hadden for his support and collaboration throughout. I would like to thank all the ICS cleanroom staff, particularly Dr. Tom Peach, for helping me throughout the years with process development and teaching me e-beam lithography. I would like to thank everyone at QLab, in no particular order: Joseph, Bilge, Sherif, Rachel, Annie, Yanzhao, Matthew, Sam, Davey, Reza, Katie, Miguel, Nick, and Petros; and to the CDT staff and Cohort 1 of the Compound Semiconductor Manufacturing CDT: Paradeisa, Rachel, Tristan, Seyed/Oorman, Bogdan, and Will, for their support, friendship, and advice throughout the years. I would also like to thank Phil Buckle, the first person I talked to about applying to the CDT. And thanks to my friends and family for keeping me going. To my Mum, Ryan, Jaydn, Lawrence, and Ella. And to my Granddad, for teaching me about subatomic particles and black holes all those years ago, if only you knew at the time what you had caused.

"The only way out is through"

Contents

Chapter 1

Introduction

Photonics is the study of light and its interactions with matter; photonics scientists and engineers study and create devices which harness and manipulate light for a wide range of applications such as optical communications [1]–[6], medicine [4], [7]–[11], agriculture [12]–[15], consumer products [16]–[21], and quantum information processing [22]–[27]. One branch of photonics is integrated photonics, or photonic integrated circuits. Photonic integrated circuits (PICs) consist of multiple semiconductor photonic devices integrated for combined functionality. Examples of devices which may be on a PIC are waveguides [28], [29], couplers [30]–[33], multiplexers [34]–[36], and interferometers [37]–[39]. Analogous to the miniaturisation of transistors in electronic integrated circuits (EICs), integrated photonics is the genesis of a new age. Scientists are now able to condense and miniaturise large, bench-top optical components and circuits onto a single chip weighing barely a few grams. Like EICs, PICs may form the basis of important and ubiquitous technologies in modern life, in ways impossible to fully grasp at its genesis.

1.1 Telecommunications C-band, $\lambda = 1550\,\mathbf{nm}$

When beginning an investigation into developing integrated photonic devices, a key question is which wavelength of light to investigate. Although many wavelengths would be preferable, this is not practically possible due to the wide range of lab equipment required (for each wavelength). Wavelengths around 1550 nm (also known as the C-band) are the most commonly used wavelength of light in telecommunications. The reason for this is historical - the attenuation of light in silica optical fibres

is lowest at this wavelength, as shown in figure 1.1 taken from Ref. [40]. As optical data (e.g., the internet) is propagated over very large distances - hundreds and thousands of km - selecting the lowest attenuation/absorption regimes as possible is vital. As a result of this, technological aspects surrounding optical data transfer such as laser sources, detectors and fibres, have been commonly manufactured for this wavelength regime. Infrastructure and equipment in this wavelength regime is readily available, and for a new technology in optical communications/optical data transfer to successfully propagate, it should look to embed itself in already existing supply chains, for minimal uptake friction.

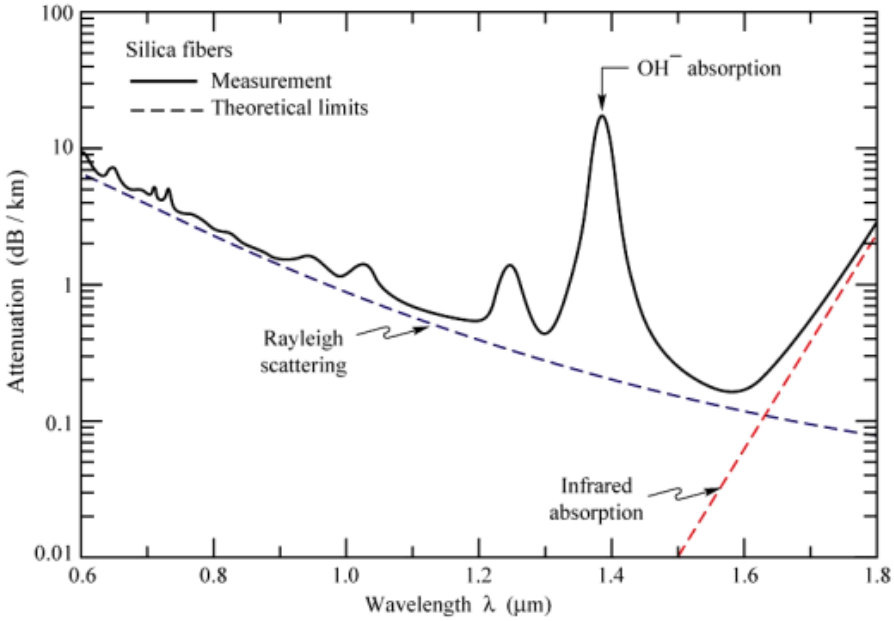

Figure 1.1: Attenuation of light in a silica optical fibre across a range of wavelengths, showing the lowest attenuation at a wavelength of 1550 nm. Image taken from [40].

1.2 Integrated Photonics

Integrated photonics is the study of nano- or micron-scale optical and photonic devices onto a single chip, combining the functionality of multiple sub-devices and/or sub-components onto a single, convenient, chip, called a photonic integrated circuit (PIC). PICs allow for reduced coupling losses between components, as light does not need to be coupled in and out to multiple different devices; they can all be combined onto a single chip via waveguides. This on-chip integration means devices can be condensed, or "miniaturised" onto a single small, lightweight chip. Applications of PICs may include optical interconnects in data centres [41] "lab-on-chip" medical sensor devices [39], [42], [43], and

quantum key distribution chips [22]. Figure 1.2 shows examples of PICs from literature to highlight the diversity of sub-components and sub-devices in PICs. Figure 1.2a shows an InP PIC, consisting of a grating coupler coupled to a nanopillar cavity, designed for use in optical interconnects; figure 1.2b shows a large-scale silicon optical phased array of grating emitters, for the generation of arbitrary high resolution far-field patterns; figure 1.2c shows a ring resonator coupled to waveguides and grating couplers, for the purpose of down-conversion of light from 1550 nm to 780 nm, with false-colour CCD images of light of different resonance frequencies propagating around the ring resonator; figure 1.2d shows silicon switching PIC for implantable optogenetic neuromodulation probe, designed to optically excite the neurons of mice, and record brain activity with electrode adjacent to grating couplers; bottom left inset: multimode interferometer switch to direct light between two ports, top right inset: vertical grating coupler and recording electrode.

Figure 1.3 shows examples of common PIC components, which we will now discuss. The simplest but most fundamental component on a PIC is a waveguide, shown in the left half of figure 1.3. Waveguides are structures designed to confine and guide light along a specific path via total internal reflection, allowing for the efficient transmission of optical signals. They are a keystone in all of integrated photonics, allowing light to propagate around a chip, and they also form the geometric basis of many other PIC components. For this reason, waveguides are the main focus of the work carried out in this thesis.

Resonators are devices which trap light, enhancing light-matter interactions, and may be integrated onto a PIC. Resonators on a PIC can be either ring resonators (round and round, e.g., racetrack resonators, seen in figure 1.3b), or Fabry-Perot (back and forth); photonic crystal nanobeam cavities (PCNCs), an example of which is shown in figure 1.3c, are a form of Fabry-Perot resonator, with light being reflected and bounced between two sets of mirrors and the light remaining in the cavity for an extended time (figure 1.3d shows a simulation of the cavity mode of the PCNC in figure c). The characteristics and design of PCNCs will be discussed and explored further in §6.

Grating couplers are optical devices used to efficiently couple light between an optical waveguide and free space or an optical fibre. They are widely employed in integrated photonics for the input/output coupling of light into and out of on-chip waveguides. The working principle of grating couplers involves the use of a periodic structure of equally spaced parallel lines or ridges engraved on a waveguide surface. Figure 1.3a shows a scanning electron micrograph (SEM) of a grating coupler consisting of concentric parallel arcs. These lines act as refracting elements that are created by a periodic variation in the

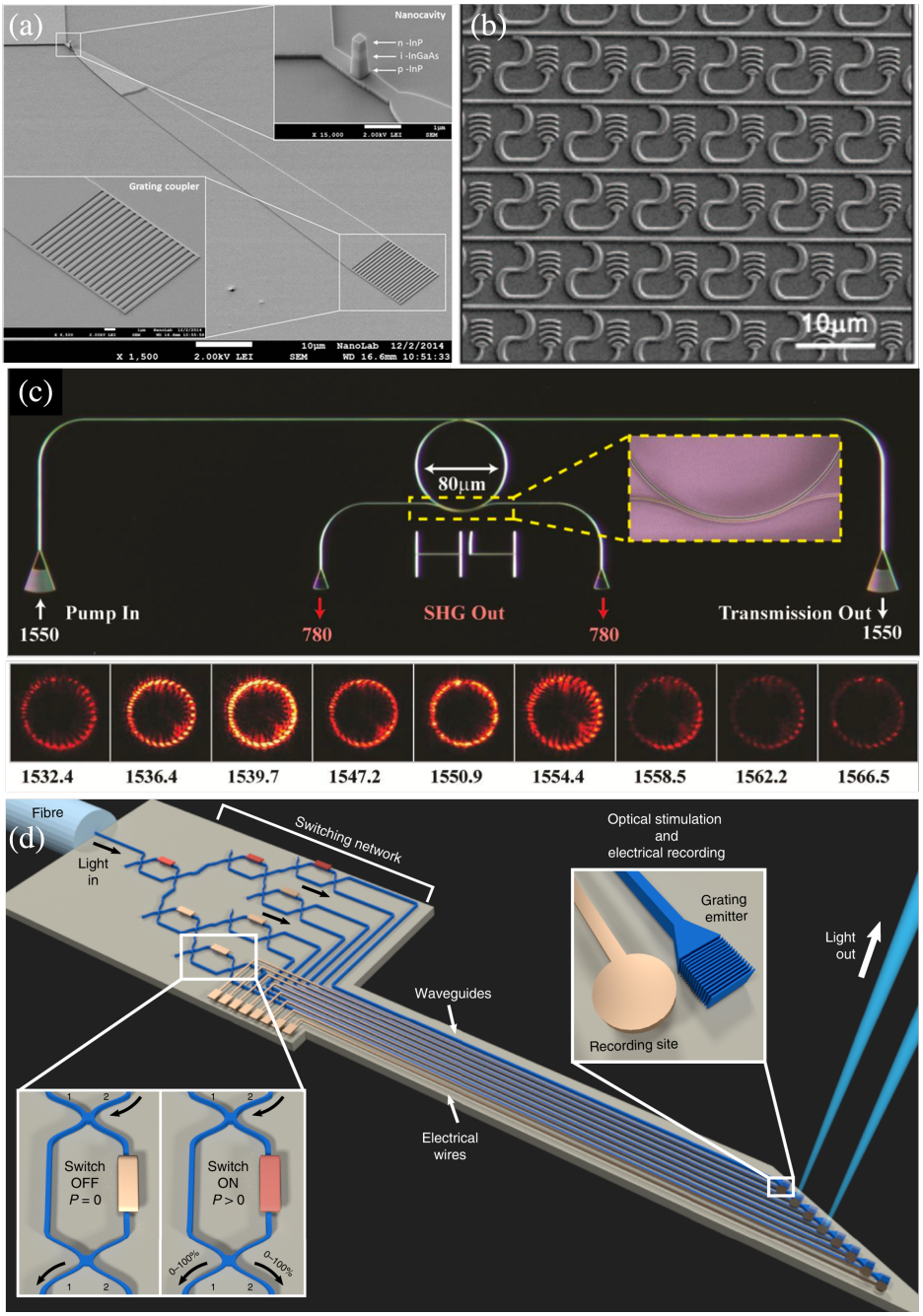

Figure 1.2: Examples of photonic integrated circuits. (a) InP grating coupler coupled to a InP/InGaAs nanopillar cavity, for use in optical interconnects [35]. (b) Large-scale silicon optical phased array of emission gratings, for the generation of arbitrary high resolution far-field patterns. The emitted phase of each pixel is adjusted by the length of the optical delay line within the pixel [33]. (c) Ring resonator coupled to waveguides and grating couplers, for the purpose of down-conversion of light from 1550 nm to 780 nm, with false-colour CCD images of light of different resonance frequencies propagating around the ring resonator [36]. (d) Silicon switching PIC for implantable optogenetic neuromodulation probe, designed to optically excite the neurons of mice, and record brain activity with electrode adjacent to grating couplers. Bottom left inset: multimode interferometer switch to direct light between two ports. Top right inset: vertical grating coupler and recording electrode [39].

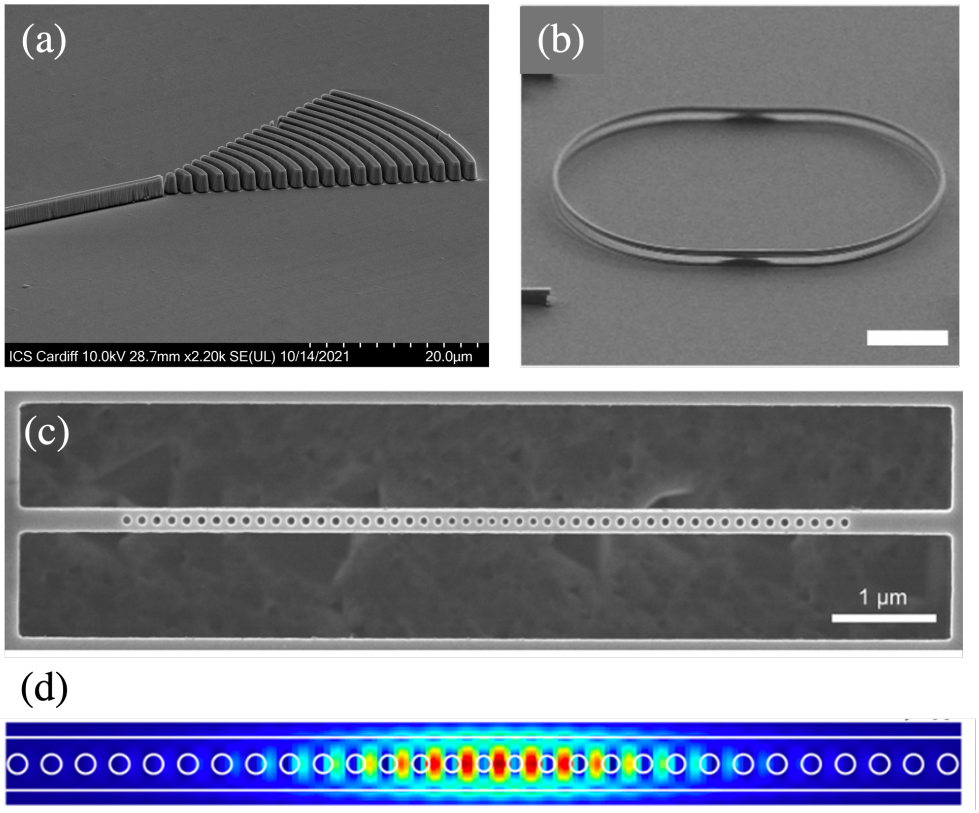

Figure 1.3: Examples of PIC components: SEMs of (a) a waveguide (left) and grating coupler (right), (b) racetrack resonator [44], (c) photonic crystal nanobeam cavity (PCNC); (d) shows a simulation of the cavity mode of c [45].

refractive index along the waveguide. When light propagates towards the grating coupler from a vertical or near vertical angle of incidence, it interacts with the grating structure. The incident light can be considered as a superposition of multiple plane waves with different incident angles and wavelengths. As the light is incident on the grating, it undergoes diffraction, leading to the constructive or destructive interference of the various diffracted orders. The efficiency of grating couplers is maximized when the diffracted orders interfere constructively at a specific angle and wavelength, known as the Bragg condition. For a grating coupler with coupling angle θ, the periodicity p of the gratings is equal to

$$p = \frac{m\lambda_0}{n_{eff} - n_{clad}\sin(\theta)}, \tag{1.1}$$

where m is the diffraction order, λ_0 is the wavelength of light, n_{eff} is the effective refractive index of the waveguide mode, and n_{clad} is the refractive index of the cladding material. Grating couplers will feature in chapter 4, where we will fabricate them in GaN on a sapphire substrate.

1.3 GaN

Compound semiconductors represent a menagerie of dielectric materials available with excellent passive and active optical properties. One such material, and the material which will be investigated in this thesis, is gallium nitride (GaN). GaN is a compound semiconductor with a direct bandgap of 3.4 eV, and has already achieved great success as an active material in LEDs and lasers, with the 2014 Nobel prize being awarded to Nakamura, Akasaki and Amano [46], [47] for producing the world's first blue LEDs, enabling efficient white light sources to be made. The refractive index of GaN at communications wavelengths ($\lambda = 1550\,\text{nm}$) is 2.32 [48], which is sufficient to provide the index contrast needed for optical confinement with an air cladding and a sapphire substrate, the typical substrate of choice for GaN that makes up the majority of devices in the literature [49]. Table 1.1 shows how GaN compares to other semiconductors.

Material	Bandgap (eV)	Bandgap type	n	Pockels coefficient
Silicon	1.12	Indirect	3.48	0
InP	1.34	Direct	3.16	1.4 pm/V [50]
GaAs	1.42	Direct	3.38	1.5 pm/V [51]
GaN	3.40	Direct	2.32	1.9 pm/V [52]

Table 1.1: Properties of GaN compared to other optical semiconductors. Index n is at a wavelength of 1550 nm.

Silicon is currently the de-facto material for PICs [53], [54] due to its low cost and high manufacturability, and although silicon is a good passive optical material with transparency at 1550 nm and low losses - typically less than -2 dB/cm [55] - silicon is a poor active optical material. GaN has some key advantages over silicon.

Firstly, its wide and direct bandgap: GaN has a wider bandgap compared to silicon, which means it can efficiently emit, detect, and manipulate light across a broader range of wavelengths, useful for various applications. Its bandgap is also sufficiently large to prevent two photon absorption (for wavelengths of 730 nm and above), a power dependent non-linear optical loss; although one photon may not have sufficient energy to promote an electron over silicon's 1.12 eV (1110 nm) bandgap, two photons (with wavelength between 555 nm and 1110 nm) together do.

Secondly, is its crystal structure, which, as opposed to silicon, is non-centrosymmetric. This structure means that it exhibits a high linear (Pockels) electro-optic effect. In the Pockels effect, the material refractive index is modified in proportion to the applied electric field strength, making it appealing for PICs with electrically-tuned applications. GaN also exhibits high nonlinear optical effects, where the light-induced polarisation in the dielectric medium is nonlinearly dependent on the intensity of the propagating light, with the second order nonlinear effect enabling frequency doubling ($f \rightarrow 2f$), and the third order nonlinear effect enabling four-wave mixing ($f_1 \pm f_2 \pm f_3 = f_4$). As the nonlinear refractive index of GaN has been shown to be an order of magnitude larger than that of conventional platforms such as Si_3N_4, AlN and $LiNbO_3$ [56], GaN is an attractive platform for PIC-based nonlinear photonic applications such as frequency conversion, supercontinuum generation and frequency comb generation.

1.4 GaN Integrated Photonics

GaN integrated photonics is a novel use of an already successful optical material. Despite being a successful optical material commonly used in solid state lighting, research and applications of GaN in integrated photonics is lacking compared to some other compound semiconductors, such as GaAs [57] [58] and InP [59]. The thriving industry in GaN solid state optics and power electronics could be a benefit for making PICs, helping to drive demand for larger wafer sizes and lower costs, making it more accessible to use the range of favourable material properties which make GaN attractive for PICs.

To the best of our knowledge, the first devices with GaN waveguides were multi quantum well

(MQW) structures (ridge waveguides) on GaN on sapphire for all-optical switching, which were first proposed by Suzuki in 1997 [60]. Similar studies [61]–[65] followed this work with waveguides on GaN/AlGaN MQWs, with a device fabricated by Ref. [65] shown in figure 1.4a.

Since then, several groups have demonstrated GaN on sapphire ridge waveguide devices, namely ring resonators [56], [66], [67] and electro-optic modulators [68], [69]. GaN's favourable optical nonlinearity has been applied in devices, being used for frequency comb generation [56] and supercontinuum light sources [66]. Ref. [66] also measured the propagation loss of their GaN waveguides to be 0.53 dB, comparable to silicon photonics. Groups have also simulated electro-optic modulators [68], including Mach-Zehnder modulators [69]. Some of these devices are shown in figure 1.4.

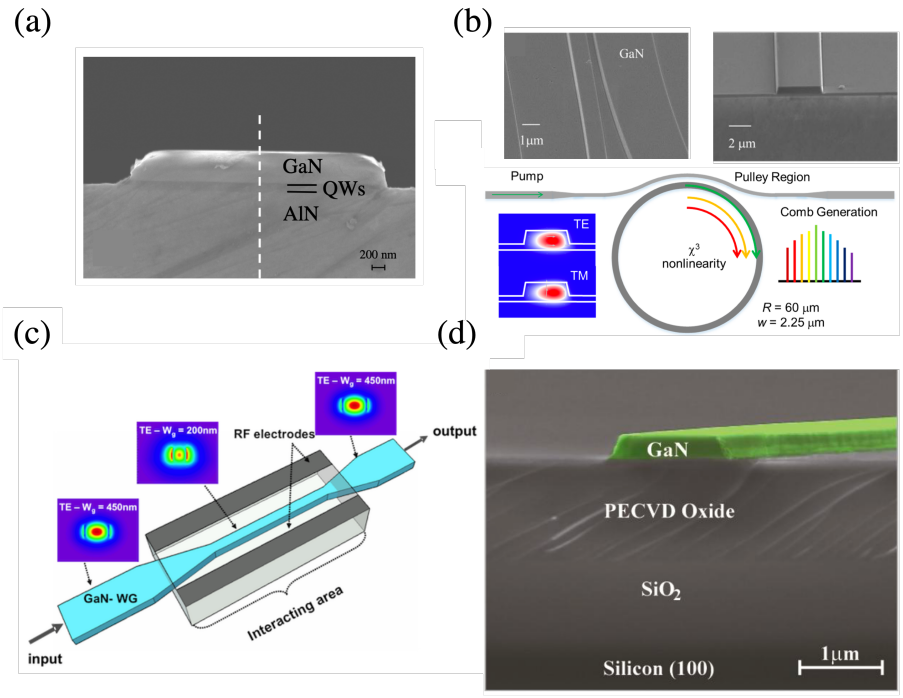

Figure 1.4: Examples of GaN waveguide devices. (a) GaN on sapphire multi quantum well (MQW) optical switch [65]. (b) GaN on sapphire ring resonator for frequency comb generation [56]. (c) GaN on sapphire electro-optic modulator [68]. (d) GaN on silicon waveguide, used to make a ring resonator for second harmonic generation [36].

As well as sapphire, silicon is also a common substrate for GaN, and has been used in integrated photonics; silicon is available in very large (e.g. 12 inch) wafer sizes [70], and is relatively cheap. However, GaN on silicon does not intrinsically have optical confinement, needed for waveguides. The refractive index n of silicon and GaN are 3.5 and 2.3 at $\lambda = 1550\,\text{nm}$, respectively. However, groups have circumvented this through using a low index oxide epilayer [36], [71] (with these devices again

using GaN's nonlinearity, this time for second harmonic generation), seen in figure 1.4d, or through using the silicon as a sacrificial layer, removing parts of the silicon to 'suspend' GaN nanobeams above the remaining silicon substrate [45], [72], [73], confining light with the index contrast from air. This technique has been used to fabricate waveguides [72], [74], [75], PCNC lasers [45], [73], microdisk lasers [75], and grating couplers [75], all shown in figure 1.5.

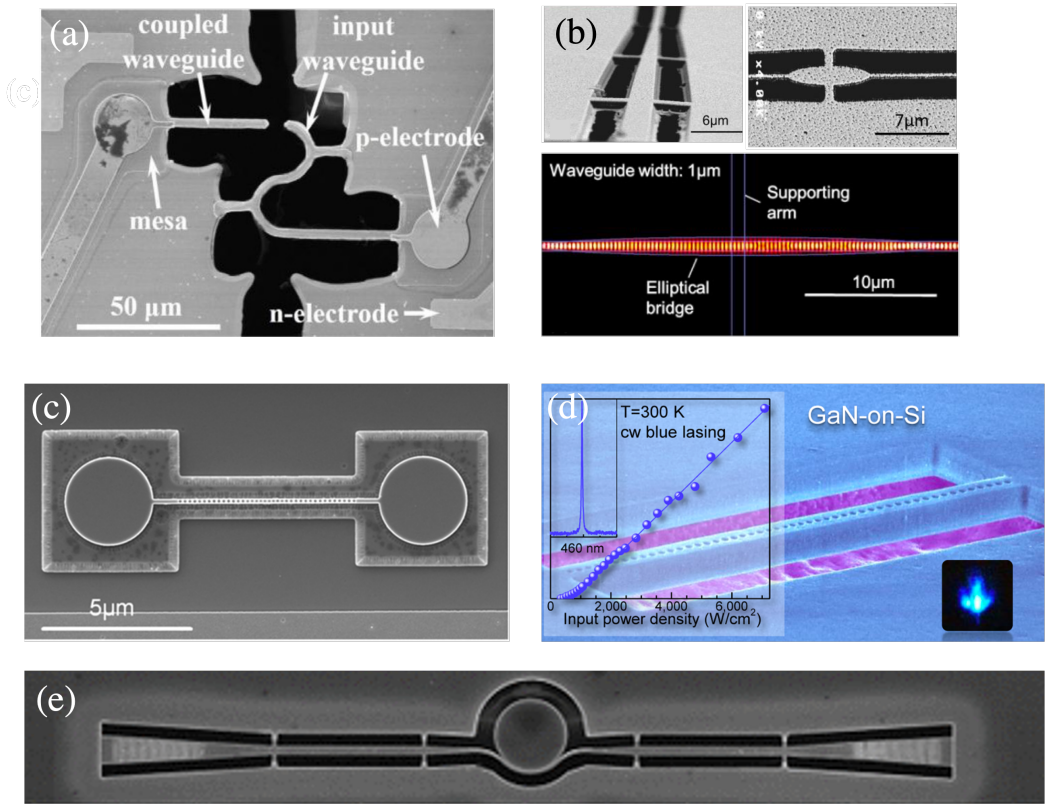

Figure 1.5: Examples of devices made using GaN nanobeams suspended above silicon substrates. (a) GaN/InGaN MQW LED (emitter), waveguide and MQW photodiode (detector) on a single chip [74]. (b) Ref. [72] fabricated suspended nanobeams intended for on-chip LED integration, with the mode $|E|^2$ profile shown. (c) and (d)Suspended photonic crystal nanobeam cavities capable of efficient lasing of blue light [45], [73]. (e) Grating couplers and microdisk laser [75].

1.5 Outline of the Thesis

In this thesis, we will present our work on investigating GaN as a platform for integrated photonics at 1550 nm. We will simulate and fabricate GaN on sapphire ridge waveguides, investigating the effects of waveguide geometry on fundamental modes, as well as studying GaN triangular cross-section nanobeams and how they behave as waveguides and width-modulated PCNCs. Chapter 2 presents electromagnetic theory relevent to the results presented in this thesis. Chapter 3 outlines the simulation and manufacturing methods used for the results in this thesis. Chapter 4 details the simulation and fabrication of GaN ridge waveguides on a commercial GaN on sapphire substrate, analysing waveguide dimensions suitable for fabrication at 1550 nm, and evaluating our fabrication process. Chapter 5 presents simulation results investigating the capability of GaN triangular cross-section nanobeams as waveguides, where we perform eigenmode calculations and investigate how features in geometry including etch angle and asymmetry affect the modes supported. Chapter 6 describes 3D FDTD simulations of GaN width-modulated triangular PCNCs, where we detail a cavity design consisting of two Bragg mirrors either side of a central half-wavelength spacer region. We calculate the Q factor as a function of cavity length, and compare and contrast calculating Q using the spectra and the ringdowns of the cavities. We also present a method of simulating the effect of loss on Q factor. Finally, we conclude the thesis in chapter 7 with a summary of the key findings and suggest some recommendations for further study.

Chapter 2

Electromagnetic Theory

2.1 Maxwell's Equations and The Wave Equation

In this thesis, much of the work is based on numerical simulations of the optical properties of, and light propagation in, optical components in PICs. These numerical simulations rely on solving Maxwell's equations in various ways, so this section introduces Maxwell's equations of electromagnetism, and derives the wave equation from them.

Maxwell's equations of electromagnetism relate five vector quantities, $\mathbf{E}$, $\mathbf{D}$, $\mathbf{H}$, $\mathbf{J}$ and $\mathbf{B}$, and one scalar (ρ), where $\mathbf{E}$ is the electric field, $\mathbf{D}$ is the electric displacement, $\mathbf{H}$ is the magnetic field, $\mathbf{J}$ is the current vector, $\mathbf{B}$ is the magnetic flux density, and ρ is current density. In dielectric materials, it is usual to assume there are no charges or current, so $\rho = 0$ and $\mathbf{J} = 0$. Maxwell's equations are then:

$$\boldsymbol{\nabla} \cdot \mathbf{D} = 0 \tag{2.1}$$

$$\boldsymbol{\nabla} \cdot \mathbf{B} = 0 \tag{2.2}$$

$$\boldsymbol{\nabla} \times \mathbf{E} = -\frac{\partial \mathbf{B}}{\partial t} \tag{2.3}$$

$$\boldsymbol{\nabla} \times \mathbf{H} = \frac{\partial \mathbf{D}}{\partial t} \tag{2.4}$$

where $\boldsymbol{\nabla}\cdot$ is the divergence and $\boldsymbol{\nabla}\times$ is the curl of a scalar or vector field. To progress, the relationships between $\mathbf{D}$ and $\mathbf{E}$ and $\mathbf{B}$ and $\mathbf{H}$ are needed. Such relationships are known as the material or constitutive relations. In linear materials they are simple linear relationships:

$$\mathbf{D} = \varepsilon_0 \varepsilon \mathbf{E}, \tag{2.5}$$

and

$$\mathbf{B} = \mu_0 \mu \mathbf{H}. \tag{2.6}$$

$\varepsilon_0\varepsilon$ is the electric permittivity of the material, where ε_0 is the permittivity of free space and ε is the relative permittivity of the material. $\mu_0\mu$ is the magnetic permeability of the material, where μ_0 is the permeability of free space and μ is the relative permeability.

Taking the curl $\boldsymbol{\nabla}\times$ of equation 2.3:

$$\boldsymbol{\nabla} \times [\boldsymbol{\nabla} \times \mathbf{E}] = \boldsymbol{\nabla} \times \left[-\frac{\partial \mathbf{B}}{\partial t} \right] \tag{2.7}$$

and changing the order of differentiation on the right-hand side:

$$\boldsymbol{\nabla} \times [\boldsymbol{\nabla} \times \mathbf{E}] = -\frac{\partial}{\partial t} [\boldsymbol{\nabla} \times \mathbf{B}] \tag{2.8}$$

Substituting in equation 2.4 and 2.5:

$$\boldsymbol{\nabla} \times [\boldsymbol{\nabla} \times \mathbf{E}] = -\frac{\partial}{\partial t} \left[\mu_0 \varepsilon_0 \mu \varepsilon \frac{\partial \mathbf{E}}{\partial t} \right] = -\mu_0 \varepsilon \mu \varepsilon \frac{\partial^2 \mathbf{E}}{\partial t} \tag{2.9}$$

where we assume both μ and ε are independent of time (i.e., μ and ε are constants).

$$\boldsymbol{\nabla} \times [\boldsymbol{\nabla} \times \mathbf{E}] = -\mu_0 \varepsilon \mu \varepsilon \frac{\partial^2 \mathbf{E}}{\partial t} \tag{2.10}$$

Using the identity $\boldsymbol{\nabla} \times [\boldsymbol{\nabla} \times \mathbf{E}] = \boldsymbol{\nabla}(\boldsymbol{\nabla} \cdot \mathbf{E}) - \boldsymbol{\nabla}^2 \mathbf{E}$, and $\boldsymbol{\nabla} \cdot \mathbf{E} = 0$ (as from equations 2.1 and 2.5 current density = 0), we are left with the wave equation for the electric field:

$$\boldsymbol{\nabla}^2 \mathbf{E} = \mu_0 \varepsilon_0 \mu \varepsilon \frac{\partial^2 \mathbf{E}}{\partial t^2}, \tag{2.11}$$

A similar derivation gives a similar wave equation for **H**:

$$\boldsymbol{\nabla}^2\mathbf{H} = \mu_0\varepsilon_0\mu\varepsilon\frac{\partial^2\mathbf{H}}{\partial t^2}. \tag{2.12}$$

The solutions to the wave equation are plane waves with angular frequency ω and wavevector k:

$$\mathbf{E} = E_0 e^{i(k.r-\omega t)}, \tag{2.13}$$

where k is

$$k = \frac{2\pi}{\lambda} \tag{2.14}$$

and describes the change of phase of the propagating wave, and r is the position vector. Light travels at a speed of $\frac{1}{\sqrt{\mu_0\varepsilon_0\mu\varepsilon}}$, with this speed typically written c/n, where

$$c = \frac{1}{\sqrt{\mu_0\varepsilon_0}} \tag{2.15}$$

is the speed of light in a vacuum, and

$$n = \sqrt{\mu\varepsilon} \tag{2.16}$$

is the refractive index of material, describing the factor by which the speed of light is reduced from that of a vacuum.

2.1.1 Optical Modes in a One-Dimensional Waveguide

Optical modes in a waveguide correspond to specific spatial distributions of the wave function that satisfy the boundary conditions of the waveguide structure. As light propagates along a device, a mode's electric field may be directed perpendicular to the direction of travel - this is called a transverse electric, or TE mode - or a mode may have its magnetic field directed perpendicular to the direction of travel - these are called transverse magnetic, or TM modes. Optical confinement in a waveguide usually occurs as a result of total internal reflection, with the wavevector of the mode k being imaginary and the wave exponentially decaying in the optically confining cladding dielectric n_1. The wavevector k is real in the waveguide dielectric n_2 and the wave propagates, with the condition that $n_1 < n_{eff} < n_2$, with n_{eff} being the effective refractive index of a guided mode. The effective refractive index n_{eff},

equation 2.17, is a constant analogous to the material refractive index, and is the ratio of the wavevector k of the mode to the freespace wavevector k_0, describing the speed of light guided by the waveguide relative to the speed in a vacuum. The n_{eff} is a typical characteristic used to describe modes, and can be calculated using simulation software, discussed in section 3.1, and is considered the eigenvalue of the waveguide mode.

$$n_{eff} = \frac{k}{k_0}. \tag{2.17}$$

In this section, we will provide a simple one-dimensional example derivation of the waveguide modes starting from Maxwell's equations. This one-dimensional example is a simplified but instructive case to show how waveguide modes are formed in a dielectric structure.

The time dependence of Maxwell's equations can be separated by using harmonic fields according to

$$\boldsymbol{\psi}(\mathbf{r}, t) = \boldsymbol{\psi}(\mathbf{r}) e^{-i\omega t} \tag{2.18}$$

where $\boldsymbol{\psi}$ can represent $\mathbf{D}$, $\mathbf{B}$, $\mathbf{E}$ or $\mathbf{H}$. Using this harmonic form of equations 2.3 and 2.4,

$$\boldsymbol{\nabla} \times \mathbf{E} = -\frac{\partial \mathbf{B}}{\partial t} = i\omega \mathbf{B} = i\omega \mu_0 \mu \mathbf{H} \tag{2.19}$$

$$\boldsymbol{\nabla} \times \mathbf{H} = \frac{\partial \mathbf{D}}{\partial t} = -i\omega \mathbf{D} = -i\omega \varepsilon_0 \varepsilon \mathbf{E} \tag{2.20}$$

We will now apply the TE wave equation to the case of a one-dimensional slab waveguide, with refractive index given by equation 2.21, where n_1 and n_2 are the index of the cladding and waveguide, respectively, and w is the width of the waveguide, with a diagram of this structure shown in figure 2.1.

$$n(y) = \begin{cases} n_1, |y| > \frac{w}{2} \\ n_2, |y| \leq \frac{w}{2} \end{cases} \tag{2.21}$$

For a structure which is varying in the y direction, and with light propagating in the z direction, the change in the x direction is zero, $\frac{\partial}{\partial x} = 0$. The electric and magnetic fields for a TE mode can be written as

$$\mathbf{E} = (E_x, 0, 0)$$

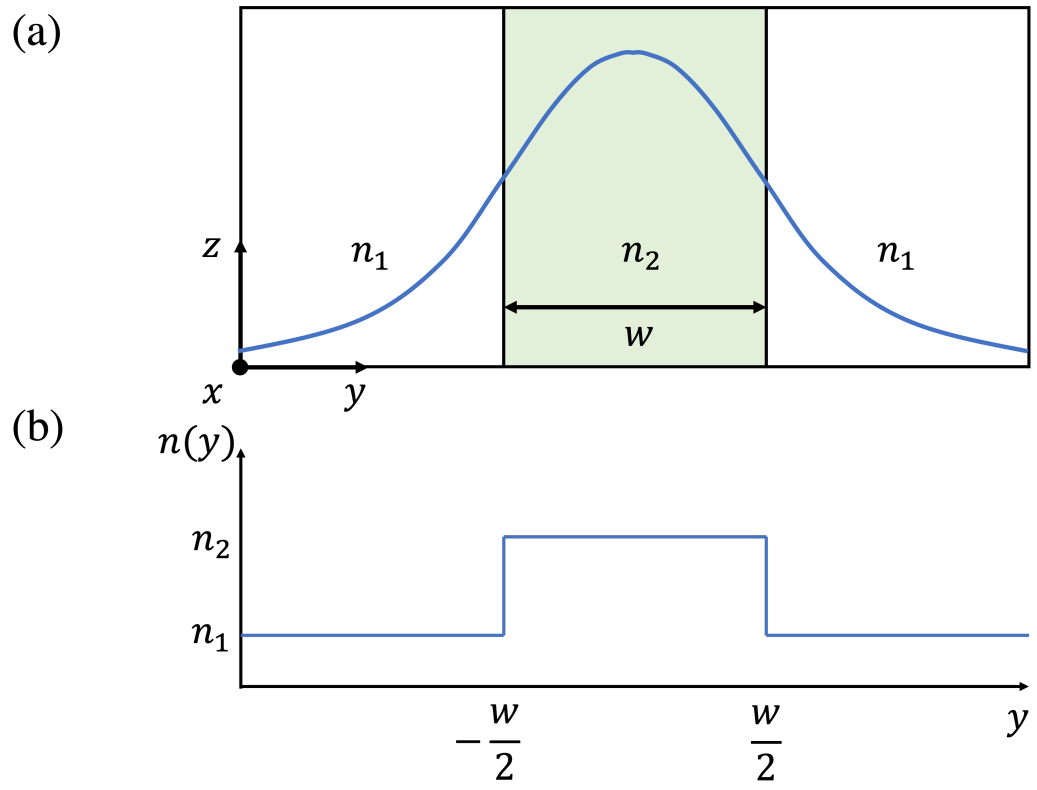

Figure 2.1: One-dimensional waveguide structure for example application of the wave equation. Light is propagating in the z direction. (a) Optically confining cladding and waveguide (width w) with index n_1 and n_2, respectively. Blue line shows the solution to $E_y(y)$. (b) Profile of the refractive index of the waveguide and cladding, as a function of y position.

and

$$\mathbf{H} = (0, H_y, H_z).$$

Equations 2.19 and 2.20 then become

$$\frac{\partial E_z}{\partial y} - \frac{\partial E_y}{\partial z} = \cancel{i\omega\mu_0\mu H_x} = 0 \tag{2.22}$$

$$\frac{\partial E_x}{\partial z} - \cancel{\frac{\partial E_z}{\partial x}} = i\omega\mu_0\mu H_y \tag{2.23}$$

$$\cancel{\frac{\partial E_y}{\partial x}} - \frac{\partial E_x}{\partial y} = i\omega\mu_0\mu H_z \tag{2.24}$$

$$\frac{\partial H_z}{\partial y} - \frac{\partial H_y}{\partial z} = -i\omega\varepsilon_0\varepsilon E_x \tag{2.25}$$

$$\frac{\partial H_x}{\partial z} - \cancel{\frac{\partial H_z}{\partial x}} = \cancel{-i\omega\varepsilon_0\varepsilon E_y} = 0 \tag{2.26}$$

$$\cancel{\frac{\partial H_y}{\partial x}} - \frac{\partial H_x}{\partial y} = \cancel{-i\omega\varepsilon_0\varepsilon E_z} = 0 \tag{2.27}$$

Solutions exist for both orthogonal polarisations, the TE and TM modes. For conciseness, we will focus on the TE mode (the TM mode can be found by applying the electric and magnetic fields $\mathbf{E} = (0, E_y, E_z)$ and $\mathbf{H} = (H_x, 0, 0)$ in the same way as above). Taking the second derivative with respect to z of equation 2.23 and y of equation 2.24, and substituting these into equation 2.25,

$$\frac{\partial^2 E_x}{\partial y^2} + \frac{\partial^2 E_x}{\partial z^2} + k^2 E_x = 0 \tag{2.28}$$

is the wave equation for the TE mode, where $k^2 = \omega^2\varepsilon_0\varepsilon\mu_0\mu$. This waveguide supports TE modes travelling in the z direction (light propagating in z) having the form:

$$E_z = E_{0,z}(y)e^{(ik_z z - i\omega t)} \tag{2.29}$$

where the propagation constant, k_z, must be the same in all three regions. Substituting equation 2.29

into the TE mode wave equation, equation 2.28 becomes

$$\frac{\partial^2 E_{0,x}(y)}{\partial y^2} + k_y^2 E_{0,x}(y) = 0 \tag{2.30}$$

where

$$k_y^2 = k^2 - k_z^2 \tag{2.31}$$

The solution of equation 2.31 in the waveguide (the incident wave and its reflection) is a sinusoidal wave, and in the substrate the solution takes the form of an exponential decay. Hence, the general solution is

$$E_{0,x} = \begin{cases} Ae^{-ik_{1,y}y} & y < \frac{w}{2} \\ B\sin(k_{2,y}y) + C\cos(k_{2,y}y) & -\frac{w}{2} \leq y \leq +\frac{w}{2} \\ De^{(+ik_{1,y})} & y > +\frac{w}{2} \end{cases} \tag{2.32}$$

As the solutions need to be confined to the waveguide and oscillate as sines and cosines, $k_{2,y}$ is real, whereas the solutions should exponentially decay in the substrate, so $k_{1,y}$ is imaginary. The three layers (two cladding layers and one waveguide layer) have the same k_z but different k and k_y,

$$k_1^2 = k_z^2 + k_{1,y}^2 = \left(\frac{n_1\omega}{c}\right)^2 \tag{2.33}$$

$$k_2^2 = k_z^2 + k_{2,y}^2 = \left(\frac{n_2\omega}{c}\right)^2 \tag{2.34}$$

k_z then written in terms of k and k_y is

$$k_z^2 = k_1^2 - k_{1,y}^2 = k_2^2 - k_{2,y}^2 = \left(\frac{n_{eff}\omega}{c}\right)^2 \tag{2.35}$$

where n_{eff} is the effective refractive index of the waveguide mode, where

$$n_1 < n_{eff} < n_2 \tag{2.36}$$

From equation 2.24, H_z is the gradient of E_x. Hence

$$H_{0,z} = -\frac{1}{i\omega\mu_0\mu} \begin{cases} -ik_{1,y}Ae^{-ik_{1,y}y} & y < \frac{w}{2} \\ k_{2,y}B\sin(k_{2,y}y) + k_{2,y}C\cos(k_{2,y}y) & -\frac{w}{2} \leq y \leq +\frac{w}{2} \\ ik_{1,y}De^{+ik_{1,y}y} & y > +\frac{w}{2} \end{cases} \tag{2.37}$$

2.1.2 Optical Modes in a Two-Dimensional Waveguide

We have now solved the electric and magnetic field wave equation(s) for the TE mode in a one-dimensional waveguide. This analysis has demonstrated how Maxwell's equations, the fundamental laws of light propagation, can be applied to dielectric materials to form waveguide modes. We will now apply these equations to a two-dimensional geometry, to provide a more realistic demonstration.

Figure 2.2 shows an example two-dimensional geometry with a ridge waveguide of width w, height h and index n_2 on a substrate of index n_1, with a cladding of index n_3, where $n_3, n_1 < n_2$ is required for optical confinement. Figure 2.2 also shows a TE mode solution calculated using Lumerical's MODE finite difference eigenmode (FDE) software [76]. Similarly to the previous 1D case, the propagation constant k is imaginary and light exponentially decays outside of the waveguide ($n = n_1, n_3$), and inside the waveguide ($n = n_2$) k is real and light oscillates sinusoidally.

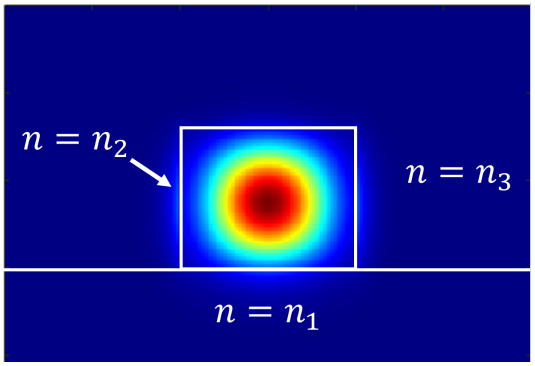

Figure 2.2: 2D ridge waveguide of index $n = n_2$ on a substrate of index $n = n_1$ with an air cladding of $n = n_3$, where $n_3, n_1 < n_2$. The TE solution for a GaN on sapphire waveguide calculated using Lumerical's MODE finite difference eigenmode (FDE) software [76] is also shown. Outside of the waveguide the propagation constant k is imaginary and light exponentially decays, and inside the waveguide k is real and light oscillates sinusoidally.

As well as the effective index, another useful property to characterise a mode is its confinement. The confinement of a mode can be defined as the amount of light within a waveguide compared to the total light. In 2D, this confinement factor is

$$\%\,\text{confinement} = 100 \times \frac{\int |E_{wg}|^2\, dxdy}{\int (|E_{clad}|^2 + |E_{wg}|^2)\, dxdy}, \tag{2.38}$$

where $|E_{wg}|^2$ is the $|E|^2$ in the waveguide, and $|E_{clad}|^2$ is the $|E|^2$ outside the waveguide; this cladding can be air, as in suspended waveguides, or air and a dielectric substrate, as in figure 2.2, or another cladding material, such as silicon dioxide. Another useful characteristic of light in a waveguide is the group velocity dispersion (GVD), given by equation 2.39. The GVD describes the extent to which the different frequency components of light in a device will travel at different speeds and spread out in time as the light propagates through the device.

$$GVD = \frac{1}{c} \cdot \frac{dn_g}{d\lambda} \tag{2.39}$$

where dn_g is the change in group index of the mode over a change in wavelength $d\lambda$. In a device, GVD can lead to temporal broadening and chirping of light signals. GVD can be calculated in the FDE solver, discussed in this next section, by simulating the optical modes over a range of wavelengths and calculating the respective group indices.

Chapter 3

Device Simulation and Fabrication Methods

3.1 Simulation Methods

Simulations are a vital tool used by researchers in integrated photonics, and are available in convenient off-the-shelf software packages. They allow scientists to test device designs and examine how devices would perform without having to physically fabricate them, allowing for the adjustment or correction of a device design before fabrication, saving significant time, money and resources. In this section, we will briefly outline two of the most common types of photonic simulations, finite difference eigenmode (FDE) and finite difference time domain (FDTD).

3.1.1 Finite-Difference Eigenmode Method

The finite-difference eigenmode (FDE) solver calculates the spatial profile and frequency dependence of modes by solving Maxwell's equations on a cross-sectional 2D mesh of the waveguide, seen in figure 3.1. The FDE solver calculates the mode field profiles and effective index, and software-integrated frequency sweeps make it easy to calculate properties such as group delay and dispersion. FDE discretises the simulation region into a 2D mesh of Yee cells [77], and the eigensolver software solves Maxwell's equations as a matrix eigenvalue problem in this mesh [78] to find the modes using the finite difference approximation. Figure 3.1c shows the Yee mesh used to calculate fields in FDE in 2D

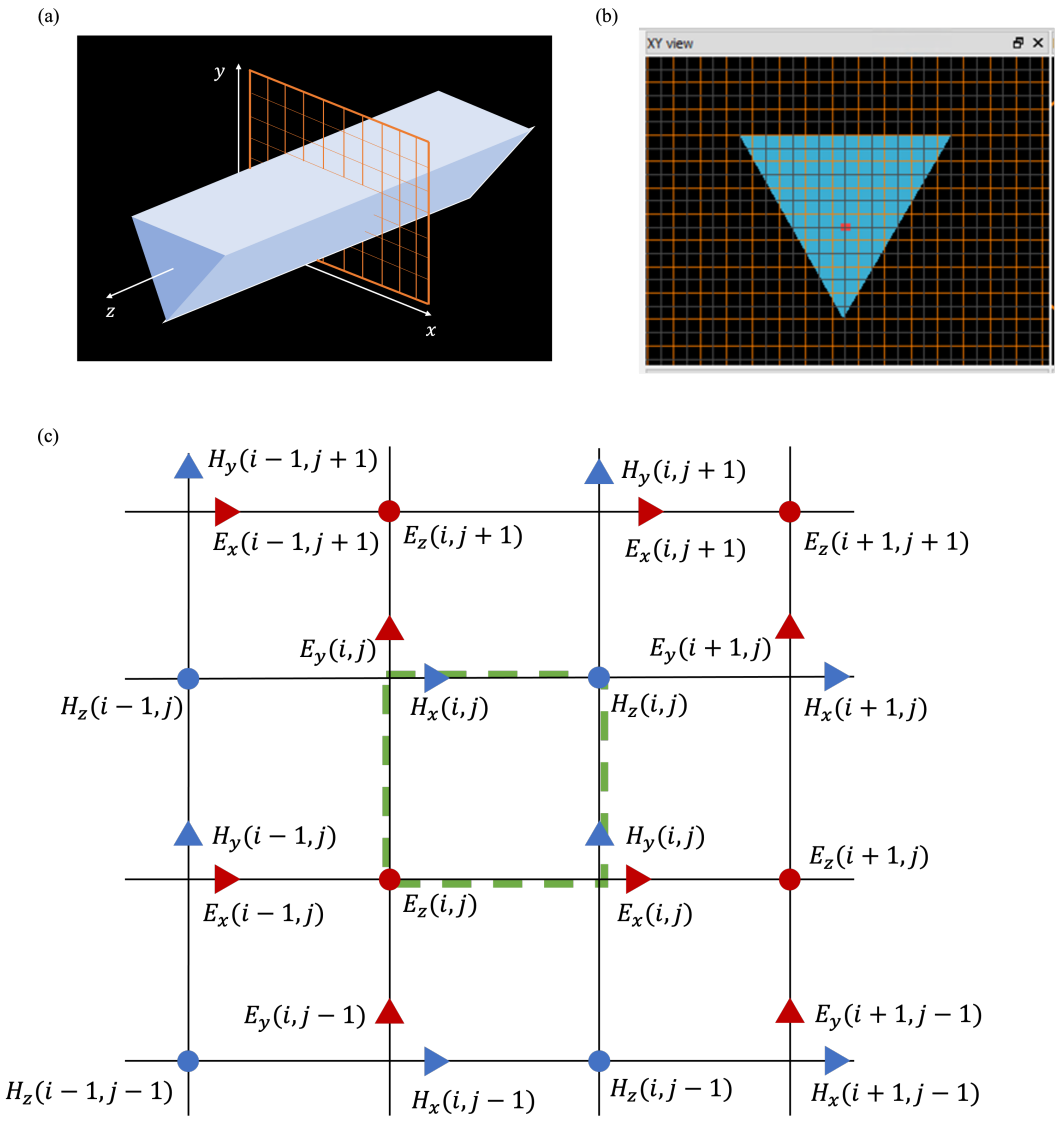

Figure 3.1: FDE solver with (a) a 2D mesh bisecting a 3D simulation object, a triangular nanobeam, and (b) a screenshot of the Lumerical FDE graphical user interface with mesh and dielectric. (c) 2D Yee mesh used to calculate fields in FDE with alternating E (red) and H (blue) fields, i and j labelling the spatial indices of the x and y positions on the mesh, respectively, with the unit cell outlined by green dashed line.

with the unit cell marked by the green box, with alternating field components at each mesh point and each field component lying on points of possible dielectric discontinuities, with the field components for each cell interpolated by the simulation software into the corner of the cell. In this thesis, we use the commercially available Lumerical FDE software package [76], which solves Maxwell's equations in the following way [78]: assume the fields have dependence $e^{i(kz-\omega t)}$. From Maxwell's curl equations $\boldsymbol{\nabla} \times \mathbf{E} = -\frac{\partial \mathbf{B}}{\partial t}$ and $\boldsymbol{\nabla} \times \mathbf{H} = \frac{\partial \mathbf{D}}{\partial t}$ (equations 2.3 and 2.4), after scaling E by the free space impedance $Z_0 = \sqrt{\mu_0/\varepsilon_0}$, we have

$$ik_0 H_x = \frac{\partial E_z}{\partial y} - ikE_y \tag{3.1}$$

$$ik_0 H_y = ikE_x - \frac{\partial E_z}{\partial x} \tag{3.2}$$

$$ik_0 H_z = \frac{\partial E_y}{\partial x} - \frac{\partial E_x}{\partial y} \tag{3.3}$$

$$-ik_0 \varepsilon_r E_x = \frac{\partial H_z}{\partial y} - ikH_y \tag{3.4}$$

$$-ik_0 \varepsilon_r E_y = ikH_x - \frac{\partial H_z}{\partial x} \tag{3.5}$$

$$-ik_0 \varepsilon_r E_z = \frac{\partial H_y}{\partial x} - \frac{\partial H_x}{\partial y} \tag{3.6}$$

Descretising these equations yields:

$$ik_0 H_x(j,l) = \frac{E_z(j,l+1) - E_z(j,l)}{\Delta y} - ikE_y(j,l), \tag{3.7}$$

$$ik_0 H_y(j,l) = ikE_x(j,l) - \frac{E_z(j+1,l) - E_z(j,l)}{\Delta x} \tag{3.8}$$

$$ik_0 H_z(j,l) = \frac{E_y(j,l+1) - E_y(j,l)}{\Delta x} - \frac{E_x(j,l+1) - E_x(j,l)}{\Delta y} \tag{3.9}$$

$$-ik_0\varepsilon_{rx}(j,l)E_x(j,l) = \frac{H_z(j,l) - H_z(j,l-1)}{\Delta y} - ikH_y(j,l) \tag{3.10}$$

$$-ik_0\varepsilon_{ry}(j,l)E_y(j,l) = ikH_x(j,l) - \frac{H_z(j,l) - H_z(j-1,l)}{\Delta x} \tag{3.11}$$

$$-ik_0\varepsilon_{rz}(j,l)E_z(j,l) = \frac{H_y(j,l) - H_y(j-1,l)}{\Delta x} - \frac{H_x(j,l) - H_x(j,l-1)}{\Delta y} \tag{3.12}$$

where

$$\varepsilon_{rx}(j,l) = \frac{\varepsilon_r(j,l) + \varepsilon_r(j,l-1)}{2} \tag{3.13}$$

$$\varepsilon_{ry}(j,l) = \frac{\varepsilon_r(j,l) + \varepsilon_r(j-1,l)}{2} \tag{3.14}$$

$$\varepsilon_{rz}(j,l) = \frac{\varepsilon_r(j,l) + \varepsilon_r(j-1,l-1) + \varepsilon_r(j,l-1) + \varepsilon_r(j-1,l)}{4} \tag{3.15}$$

Lumerical's FDE simulation software solves these differential equations to find the eigenvalues of the modes. FDE is generally quick to compute due to the lack of time dependence and does not require significant computing resources. Although FDE is capable of simulating in 3D, 2D calculations are sufficient to analyse the waveguide modes as they contain the mode profile (which is invariant in a straight waveguide), and the effective index, both of which are the two key results used in this thesis.

3.1.2 Finite-Difference Time-Domain Method

The finite-difference time-domain (FDTD) method is a widely-used general-purpose 3D electromagnetic solver commonly used for modeling nanophotonic devices in the time-domain. In this thesis, we use the commercially available Lumerical FDTD [76] software package. In 3D Yee cells, shown in figure 3.2, the electric fields are distributed on the edges of the cell, and the magnetic fields are distributed on the faces of the cell. The E and H fields are calculated in different time steps, creating a calculation which 'leapfrogs'; E and H are never calculated for the same point in time or space, offset by $1/2$ a time step and $1/2$ a space step; H fields are solved at time n, and E fields are solved at time $n + 1/2$. The simulation software automatically interpolates all field components to the corner of the Yee cell to help with visualisation and analysis of results. Like FDE, FDTD allows for the simulation of light in

arbitrary dielectric structures, allowing for flexible simulation and design of photonic devices. FDTD allows for the direct calculation of the time domain of light's evolution, using the permittivity of the device as well as a light source input to simulate the time dynamics of the electric and magnetic fields in the device.

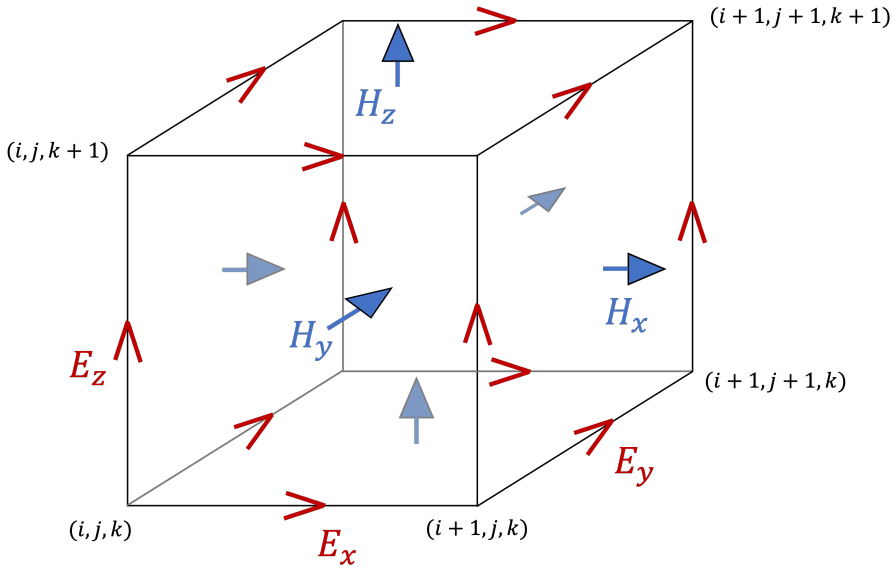

Figure 3.2: Yee cell used in finite difference time domain (FDTD) method of simulating time-evolving fields, with the electric fields distributed on the edges of the cell, and the magnetic fields distributed on the faces of the cell.

However, the high accuracy and versatility of the FDTD method does introduce some challenges. The maximum physical size of a device that can be accurately modelled is ultimately constrained by the available compute resources and is dependent on the simulation resolution as well as simulation time. The total simulation time is proportional to the number of spatial grid points N to be simulated and the simulation volume V, with $N \propto 1/dx^n$, and simulation time therefore $\propto V/dx^n$, where n is the number of spatial dimensions simulated assuming a uniform grid of step size dx. The total simulation time also naturally depends on the time the simulation runs for, characterised by the number of times steps T calculated, with $T \propto 1/dt$. Combining these two dependencies results in a total simulation time which is proportional to both the spatial resolution and the temporal resolution: simulation time $\propto 1/dt \cdot V/dx^n$. The Courant stability condition [77] states that for the time step dt of the simulation to be sufficiently small to resolve the speed of light in the medium, dt must be proportional to dx. This condition results in a total simulation time which is $\propto 1/dx \cdot V/dx^n = V/dx^{n+1}$. So, in 3D, the simulation time scales with V/dx^4, meaning a doubling in the resolution of the simulation results in a

16 times increase in simulation time. Thus, mesh accuracy and the design size can significantly impact the simulation time.

3.2 Fabrication Techniques

Fabrication of integrated photonic devices is a multi-step process involving several different fabrication techniques and equipment. This section will introduce fabrication techniques and tools available and commonly applied to fabricating semiconductor devices for integrated photonics. This section is intended to introduce the reader to the concepts of semiconductor fabrication that will be used in later chapters.

3.2.1 Lithography

Lithography, from the Ancient Greek "lithos" meaning "stone", and "graphein" meaning "to write", is the transcription of a design into a physical structure. Unlike the Ancient Greeks, we store lithographic designs as GDSII (Graphic Design System 2 [79]) files, the de-facto two-dimensional CAD format for integrated circuit design. Lithography can be 'indirect-write', as in photolithography, or 'direct-write', as in electron-/e-beam lithography. Photolithography offers essentially instantaneous exposure over full areas, but requires a separate physical mask and has lower resolution than direct-writing. E-beam lithography works masklessly, 'pixel by pixel'; it is high resolution but with lower throughput/processing speeds, and is therefore suited to research and low-volume prototyping. As such, we will focus on e-beam lithography in this thesis.

E-beam lithography works using a resist - often a solution-dissolved polymer, which is spin-coated onto the surface of a sample. The intended device design is written into the resist by exposing it with a focused beam of electrons. A positive-tone resist, when exposed, is made more soluble. When developed (for electron-beam lithography, a typical developer is a 3:1 ratio of isopropyl alcohol (IPA) and MIBK (methyl isobutyl ketone/4-methylpentan-2-one), this results in the exposed areas being dissolved and removed from the surface. Conversely, a negative-tone resist, when exposed, hardens as polymer chains are cross-linked by the exposing radiation. When a negative-tone resist is developed, the exposed region(s) remain, and the unexposed region(s) of resist are removed. Depending on the hardness of the resist compared to the substrate (known as the selectivity), a resist may itself act as an etch mask, or, a separate hard mask may need to be deposited on top, using the design of the exposed

resist.

Electron-beam lithography works via the electron-solid interactions in a resist. As electrons penetrate a resist, they undergo elastic and inelastic scattering. Elastic scattering is Rutherford scattering that can be forwards or backwards, either at small angles or large angles, respectively. Large angle back-scattering causes the 'proximity effect', where each exposure pixel receives extra dosage due to scattering from nearby pixels. The proximity effect can be counteracted by dose modulation, and the reduction of dosage can be calculated to compensate for this extra exposure. Inelastic scattering (where energy is transferred to the resist) produces secondary electrons and is responsible for exposure.

3.2.2 Inductively-Coupled Plasma Reactive-Ion Etching (ICP-RIE)

In integrated photonics we are making devices capable of guiding and manipulating light. For this, optical confinement is needed - a high index guiding core and a low index cladding. Confinement is achieved through etching, which removes portions of the semiconductor material. The lithographically written hard mask prevents substrate material underneath from being etched, transferring the device design to the substrate. Inductively coupled plasma reactive ion etching (ICP-RIE, often shortened to just ICP etching) is a common dry etching technique, which balances physical and chemical etching. Gas is input into the reactor chamber, and a high voltage strips electrons from the gas molecules, creating a 'cloud' of plasma. A second RF generator applies a DC-bias to the plasma, accelerating ions towards the sample and bombarding the surface, etching the substrate. The reactor chamber is kept under vacuum to remove reaction products from etching, and the temperature of the substrate can be controlled.

3.2.3 Scanning Electron Microscopy

As the devices we are fabricating are on the nanoscale, i.e., smaller than the wavelength of visible light, we often need to employ electron microscopy to view and image them. The most commonly used form of electron microscopy is scanning electron microscopy (SEM). SEM is a powerful tool which provides indispensable insights into device morphology and structural details. Scanning electron microscopes raster scan a focused electron-beam onto a sample's surface. The position of the beam is combined with detected intensity information to form an image. Figure 3.3 shows several SEM images which illustrate the results which can be achieved on a wide range of devices and structures by using SEM.

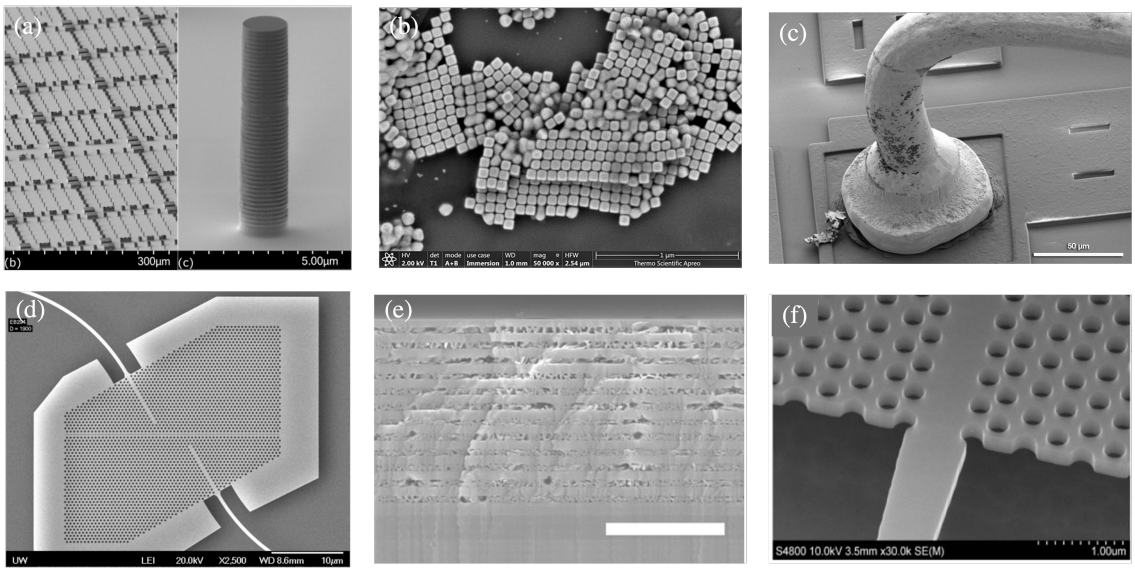

Figure 3.3: Examples of SEM images, highlighting the versatility of the tool and technique. (a) Arrays of and (b) single quantum dot micropillar cavity [80]. (b) Cluster of gold nanocubes [81]. (c) Wire bonded to a semiconductor [81]. (d) Waveguides and two-dimensional photonic crystal cavity [82]. (e) Side view of alternating layers of GaN and porosified GaN [83]. (f) Two-dimensional photonic crystal waveguide [84].

3.3 Device Processing

The devices in this thesis were fabricated using an e-beam lithography patterned nickel lift-off process, and then etched in an ICP-RIE tool. Nickel lift-off is the technique of using deposited nickel as a hard mask for etching, with nickel being used due to its high etch selectivity with GaN [85]. A positive-tone resist is lithographically patterned and developed, and nickel is deposited onto this device and resist, with the nickel adhering to the exposed regions (bare GaN). The device is then bathed in acetone, dissolving the resist and removing it from the sample surface, as well as the attached nickel, leaving only nickel attached to the GaN in the specified areas. A schematic of this lift-off process is shown in figure 3.4. Through the improvement of our lift-off process, including using thinner nickel and keeping the acetone warm, we were able to improve the device yield from approximately 20% to approximately 100%.

For our nickel lift-off process, we spin-coated a thin ($\sim$ 200 nm) layer of PMMA-A4 resist and exposed with a 115 μC cm^{-2} dosage. The sample was developed in a 3:1 IPA:MIBK solution for 30 seconds, quenching in IPA. After resist development, 30 nm of nickel was deposited onto the sample using physical vapour deposition (PVD). PVD was chosen as a deposition method due to its simplicity

of operation and sub-nm level of control of mask thickness. This simplicity and precision allowed for an overall highly controllable and repeatable process. This sample was then soaked in warm acetone ($\sim 50°C$) to remove the nickel in the unexposed regions, aka, perform nickel lift-off. Figure 3.4e shows an SEM image of nickel on a GaN surface deposited using this nickel lift-off process. Once the nickel hard mask was deposited, the sample was ICP etched with a Cl_2 and BCl_3 etch chemistry with a 2:1 ratio, at 0°C, for 7 minutes.

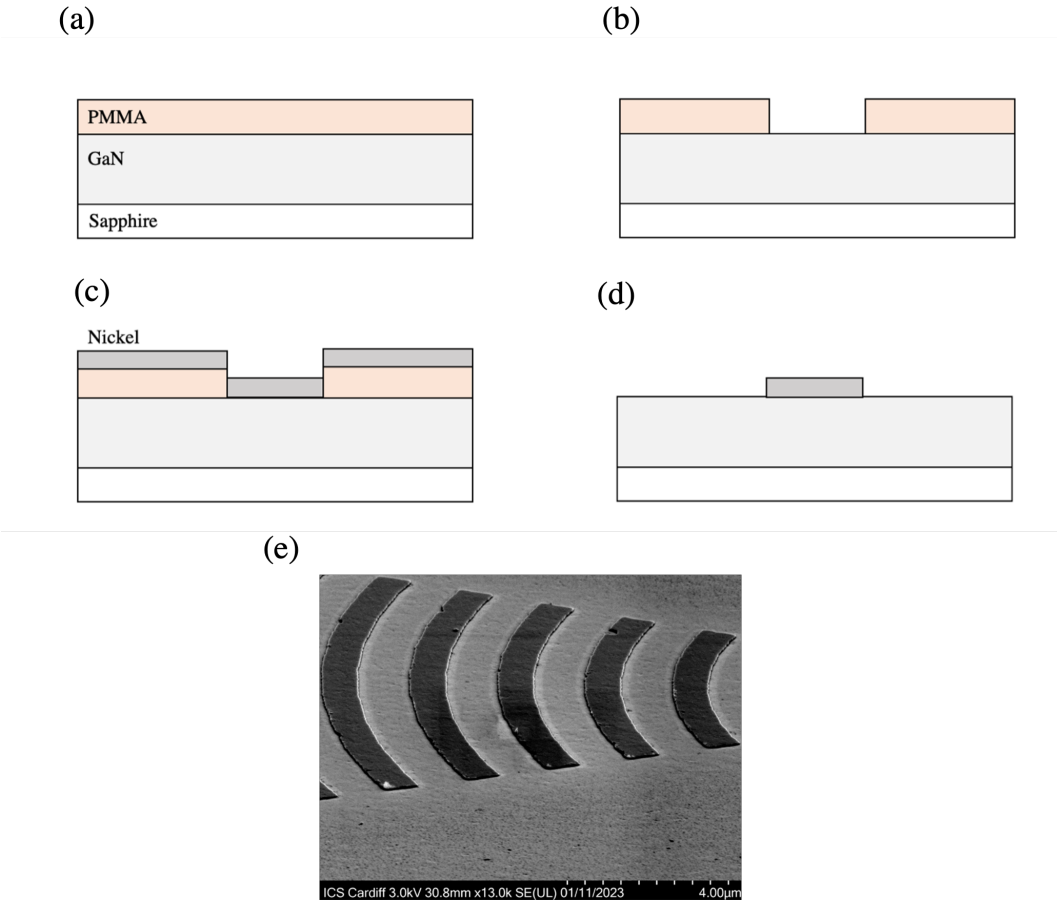

Figure 3.4: Nickel lift-off process. (a) PMMA (or other positive-tone resist) is deposited onto GaN surface (b) required design is lithographically transferred to PMMA (c) nickel is deposited (d) chip is bathed in acetone, dissolving resist and 'lifting-off' nickel on top, leaving only nickel in prescribed areas, which has adhered to the GaN surface. (e) SEM of $\sim 30\,\text{nm}$ nickel pattern deposited using lift-off with PMMA resist. This SEM shows the edge roughness of the nickel hard mask.

Chapter 4

Design and Fabrication of GaN on Sapphire Ridge Waveguides

4.1 Introduction

Perhaps the simplest and most fundamental component on a PIC is a waveguide, designed to confine and guide light along a specific path via total internal reflection. They are a keystone in all of integrated photonics, routing light and forming the geometric basis of many other PIC components. Waveguides can be designed to be either single mode or multimode, by engineering the (horizontal) width and (vertical) thickness of the waveguide in relation to the refractive index of the waveguide material. Multimode waveguides are larger than single mode waveguides and therefore easier to optically couple and align [86], however, they suffer from modal dispersion [87] and increased bend losses [88]. Rectangular cross-section ridge waveguides, shown in figure 4.1, are the most ubiquitous geometry of waveguides in integrated photonics. Sapphire could be considered to be the ideal substrate for GaN ridge waveguide integrated photonics, due to its commercial availability and the index contrast between GaN and sapphire ($n = 2.32$ and 1.75 at $\lambda = 1550\,\text{nm}$ for GaN [89] and sapphire [90], respectively,) being able to confine optical waveguide modes.

GaN on sapphire ridge waveguide simulations have been performed in the literature, however, the majority of these simulations have been of singular waveguide geometries [56], [66], [67], [69] (although Ref. [68] has simulated two different waveguide widths for their electro-optic modulator design). To the best of our knowledge, there is currently only one study analysing the mode properties of a wide

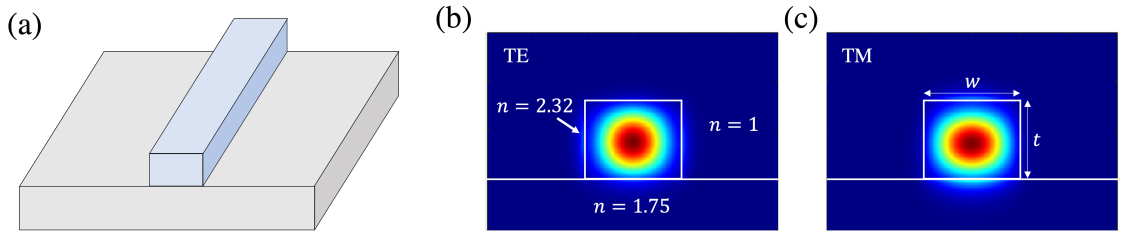

Figure 4.1: (a) Schematic of GaN ridge waveguide (blue, $n = 2.32$) on a sapphire substrate (in grey, $n = 1.75$). (b) Example of a ridge waveguide with field $|E|^2$ profiles of the fundamental TE and (c) TM modes plotted, calculated using FDE. These waveguides compose of a GaN ($n = 2.32$) on sapphire ($n = 1.75$) substrate with an air ($n = 1$) cladding, and have a thickness $t = 800\,\text{nm}$ and width $w = 1000\,\text{nm}$.

range of GaN on sapphire waveguide geometries [91], where a range of square waveguide areas were simulated and the mode area as a function of waveguide area, and a map of optical loss as a function of waveguide size and optical power, were calculated.

In this chapter, we will outline and detail the design of GaN on sapphire ridge waveguides via simulations, starting by creating 'maps' of the effective index of fundamental modes for a wide range of waveguide dimensions, finding the waveguide geometries with no confinement, and those which support higher order modes. We will then present and analyse the results of fabricating GaN on sapphire ridge waveguides in a cleanroom. The results in this chapter will act as a starting point for research and development of GaN on sapphire devices, particularly in the single mode regime, with the aim of fabricating circuits for cutback measurements. The practical results thereafter give more detailed results in fabricating using GaN for future researchers to refer to, which are not currently available in the literature, to the best of our knowledge.

4.2 Design and Simulation of GaN on Sapphire Ridge Waveguides

This section outlines and details the design and simulation of GaN on sapphire waveguides. We also describe the design and concept behind a circuit capable of experimentally measuring the optical loss as a function of propagation length.

Ridge waveguides, seen in figure 4.1, represent the perhaps simplest waveguide geometry in integrated photonics; they consist of a core of high index dielectric material of rectangular cross-section on a cladding of a low index substrate. For single-mode operation, the width of a waveguide must

not be too wide as to support higher order modes, but still wide enough to provide confinement; with single-mode operation being preferable as it decreases intermodal dispersion [87] and losses from multimode waveguide bends [88]. This width will also be dependent on the thickness of GaN material used. Figures 4.1b and c show the fundamental TE and TM modes of a representative waveguide of width 1000 nm and thickness 800 nm calculated using the FDE method.

Figure 4.2 shows the effective refractive index calculated using the FDE method as a function of waveguide (horizontal) width w and (vertical) thickness t for a GaN on sapphire waveguide, for the fundamental TE (figure 4.2a) and TM (figure 4.2b) modes. Such "maps" are a useful starting point to design waveguides, and are used in this study to determine the appropriate width and thickness of waveguides to fabricate. As well as the effective index, also shown are the waveguide geometries for which no modes are confined (region in white), and regions for which the waveguide supports higher order modes (the boundary of this is region marked by the dashed black line). As seen in figure 4.2, both TE and TM modes may have an effective index very close to the material index of GaN (2.32) if the waveguide is sufficiently large, $\sim 1800 \times 1800\,\mathrm{nm}^2$, with minimal light decaying outside the waveguide. However, these waveguides are highly multimode, with examples of higher order modes shown in figure 4.3. The single mode regions in figure 4.2a and b therefore indicate waveguide geometries which would be most appropriate to manufacture. Figure 4.2 shows there is a narrow region of waveguide widths which have a single mode operation for the TE and TM polarisations, with these being our boundaries in geometry. Choosing a waveguide thickness within this boundary will depend on the intended application. For example, if only waveguides are needed, then only a small window of widths available is needed, $\sim 50 - 100\,\mathrm{nm}$. On the other hand, if a device will have lots of variation in waveguide width, then a thickness which has a wider range of widths with confinement available is needed. However, even in the first example, we would still recommend selecting the thickness available with the largest available widths as a precaution, to maximise flexibility.

For the TE mode, the thickness with the largest available widths with modes is 500 nm, with widths between 600 nm and 1200 nm available. For the TM mode, the thickness with the largest available widths is 700 nm, with widths of 400 nm to 1100 nm available. We have selected a GaN thickness of 500 nm, due to this being the thinnest material our supplier [92] supplies, and allows for wider waveguides, which aids with fabrication. This thickness of GaN has a large range of widths available for optical confinement, marked on figures 4.2a and b by a dashed orange line.

Figure 4.4a shows the effective index for rectangular waveguides of thickness 500 nm, and width

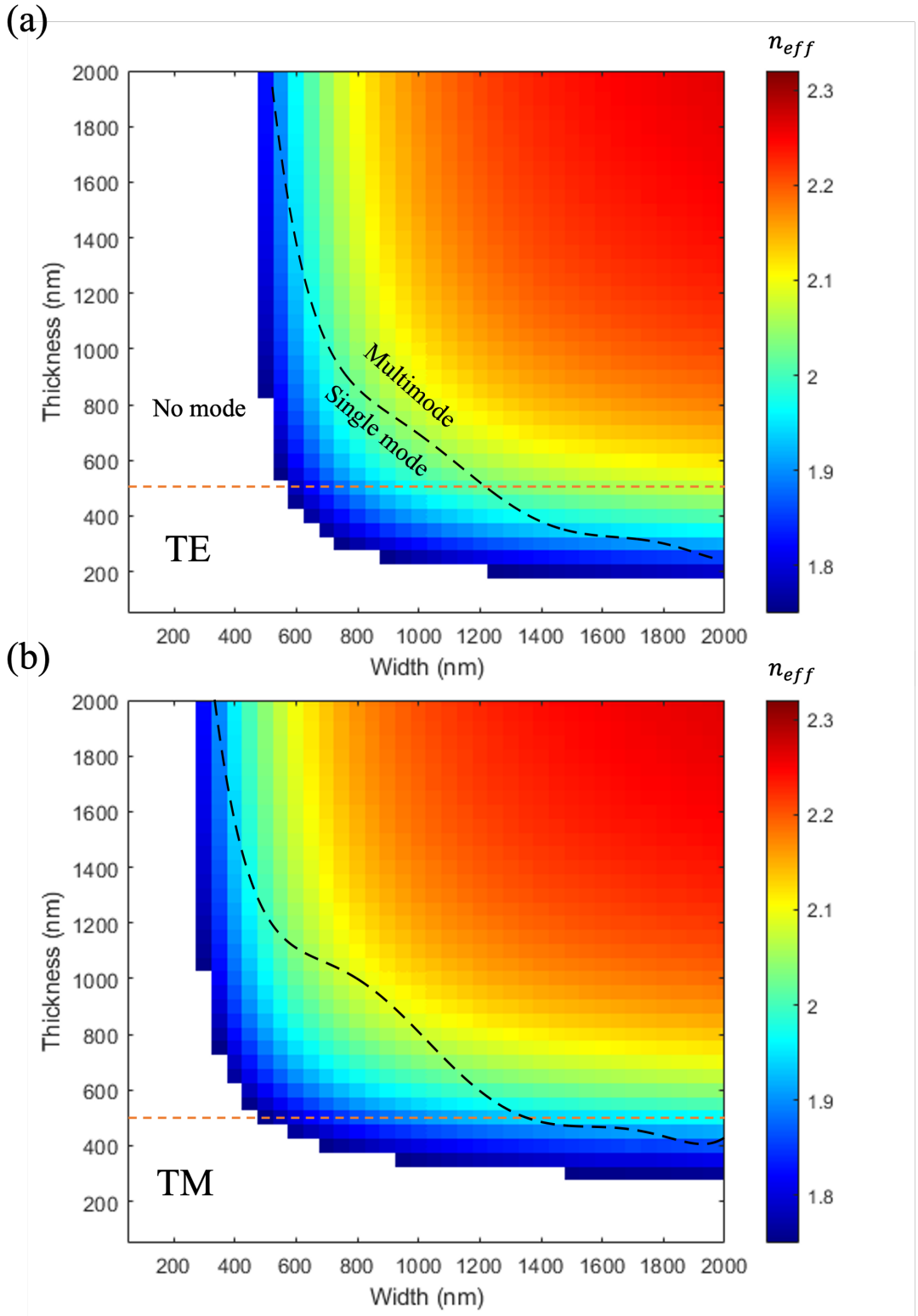

Figure 4.2: Maps of the effective index of the fundamental (a) TE and (b) TM modes in a GaN ($n = 2.32$) on sapphire ($n = 1.75$) ridge waveguide, as a function of waveguide width and thickness, calculated using FDE. Dashed black lines indicate higher order mode boundaries. Dashed orange line indicates a waveguide thickness of 500 nm.

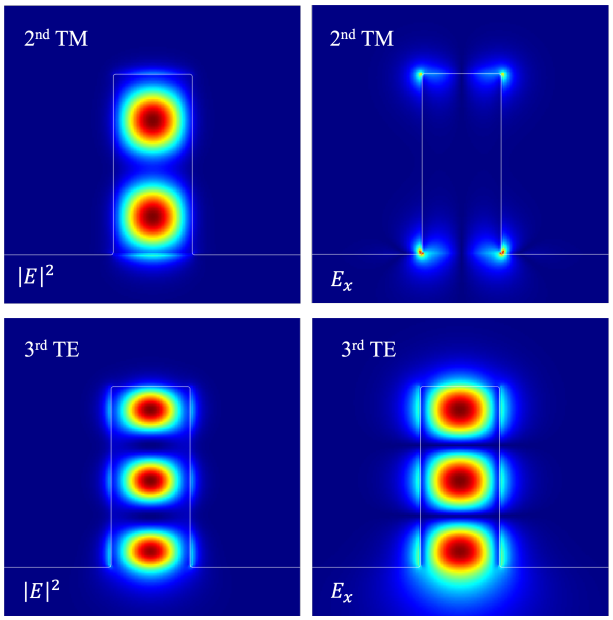

Figure 4.3: Example of multimode waveguides, with mode profiles calculated using FDE. The $|E|^2$ and E_x profiles are shown on the left and right-hand columns, respectively, for the 2nd order TM mode and 3rd order TE mode on the top and bottom rows, respectively, showing that $E_x \approx 0$ for the TM mode, and $E_x \neq 0$ for the TE mode.

varying between 550 and 1200 nm, which is the single mode regime for both the TE and TM modes. Figure 4.4b shows the mode profiles for the TE and TM modes for a range of representative rectangular waveguides, including the E_x and E_y field components for a 1250 nm wide waveguide, illustrating that $E_x \neq 0$ and $E_y \approx 0$ for the TE mode, and $E_x \approx 0$ and $E_y \neq 0$ for the TM mode. As seen and as expected, the optical confinement of both the TE and TM modes increases with an increased width. The TM mode appears to be less confined, with more of the mode present at the top and bottom waveguide interface. In a fabricated device, the results in figure 4.4a could be used to determine which mode light is in by comparing a measurement of the effective index of the mode and waveguide width to the simulated values. This method would have the limitation of the effective index of the modes being very similar in value at a width around 650 nm.

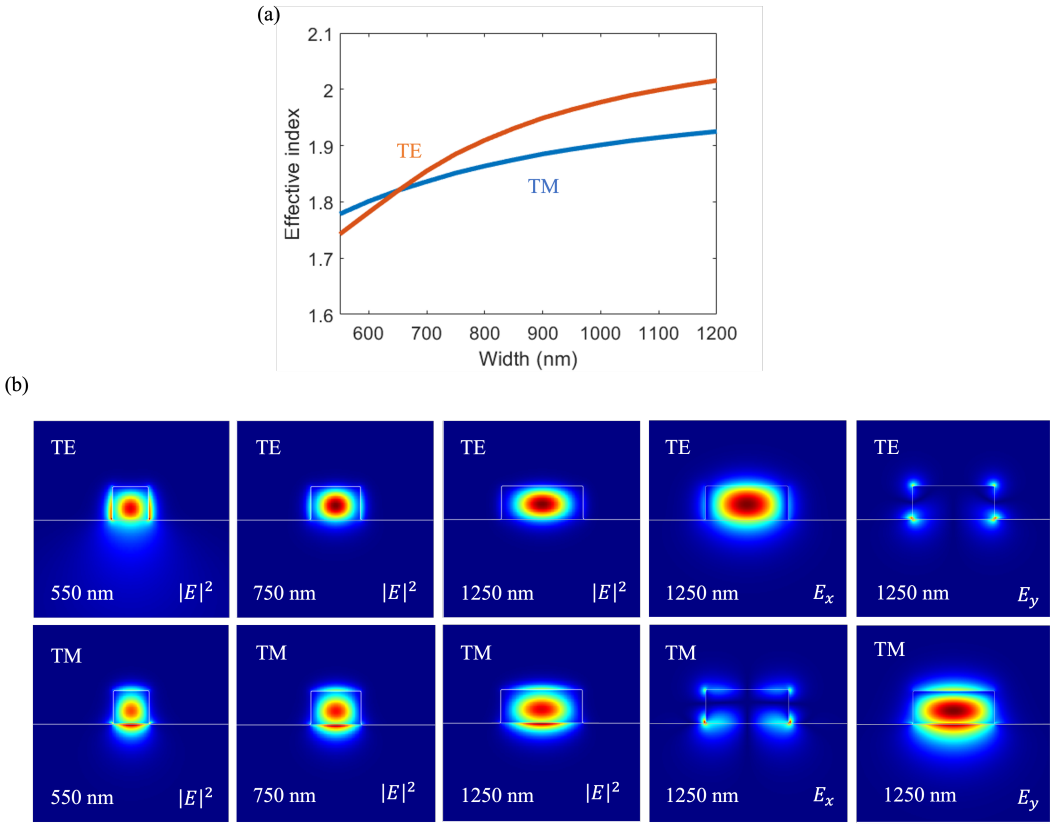

Figure 4.4: Simulation results for 500 nm thick GaN on sapphire waveguides, calculated using FDE. (a) Effective index versus waveguide width for a 500 nm thick GaN waveguide on sapphire substrate with waveguide width varying between 550 and 1200 nm, which is the single mode regime for both the TE and TM modes. (b) Mode profiles of the fundamental TE (top row) and TM (bottom row) modes for rectangular waveguides of varying widths and 500 nm thickness. $|E|^2$ profiles are plotted in the first three columns, and the E_x and E_y fields of a 1250 nm wide waveguide are plotted in the right two columns, showing that $E_x \neq 0$ and $E_y \approx 0$ for the TE mode, and $E_x \approx 0$ and $E_y \neq 0$ for the TM mode.

4.3 Manufacturing GaN on Sapphire Photonic Integrated Circuits

Manufacturing integrated photonic devices is a multi-step process involving several different fabrication techniques and equipment, requiring high levels of control, hygiene and precision throughout each step. If a single step is performed incorrectly, or is not refined enough for the task at hand, or if you are particularly unlucky that day, then it can have knock-on effects to the next processes, and even render the whole device useless; this is a daunting statement, but through careful considerations and lots of frustration, anything is possible. In this section, we will outline how to fabricate a simple photonic integrated circuit on a GaN on sapphire substrate using typical semiconductor manufacturing techniques. We will show SEM images of our results, and use these to describe the quality of the fabrication processes. We will also perform waveguide simulations to evaluate how sidewall angles imposed by our etch would affect a device.

4.3.1 Circuit Design

We have designed a relatively simple circuit, shown in figure 4.5. The purpose of this circuit is to validate the manufacturing techniques to be used to make GaN on sapphire photonic integrated circuits within the device geometries described in §4.2. This circuit consists of grating couplers and waveguides in a row with a separation of 250 μm, with the functionality based on the cut-back technique. The cut-back technique is a method of determining the power loss of an optical device as a function of propagation length [93].

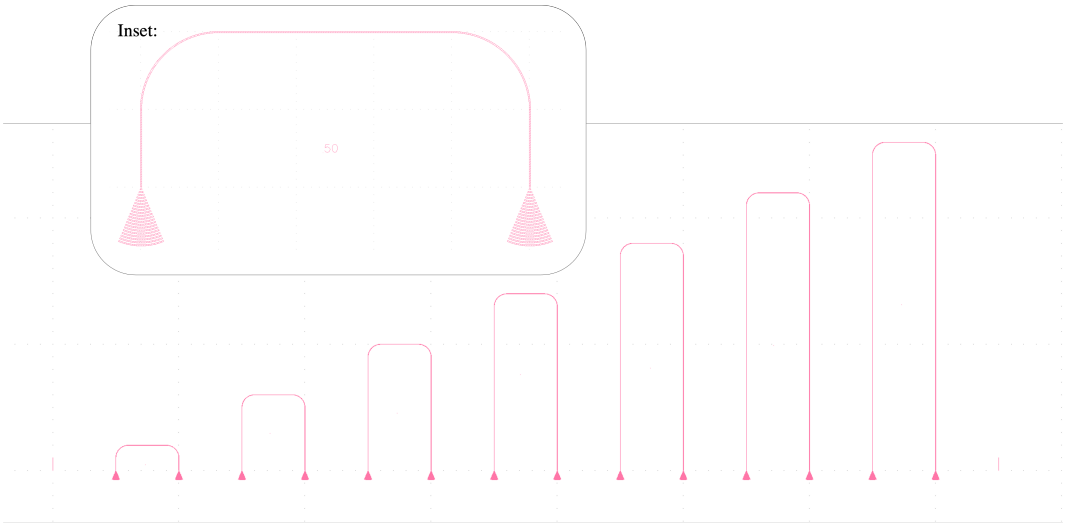

Figure 4.5: 'Cut-back' circuit for measuring the power loss of waveguides as a function of propagation length. The circuit consists of waveguide loops of increasing lengths, each with a pair of grating couplers for coupling light in/out the circuit. Each grating (and waveguide) is 250 μm apart. The waveguide loops in this figure have a bend radius of 50 μm, and each loop increases in total length by 400 μm. Inset: zoom-in of the smallest waveguide loop in the circuit, with grating couplers.

4.3.1.1 Grating Design

Grating couplers are optical devices used to efficiently couple light between an optical waveguide and free space or an optical fibre, widely employed in integrated photonics for the input/output coupling of light into and out of on-chip waveguides. The gratings at the (input/output) ends of the waveguide loop are a simple focal grating design with a pitch of around 1 μm and a width of 765 nm. Twenty grating periods were chosen to provide a large target to couple to an SMF28 optical fibre. The angle subtended by the sides of the gratings was 45°, again to ensure the grating is sufficiently large to couple an optical fibre.

4.3.2 Fabricated Circuits

Figure 4.6 shows the results of fabricating the previously detailed cutback circuit design. These devices were fabricated on a GaN on sapphire substrate, purchased from a commercial wafer supplier, KymaTech [92], with a specified GaN thickness of (500 ± 100) nm. To verify the GaN was fully etched into the sapphire substrate, we took SEM images and measurements at an angle of $\sim 60°$, seen in figure 4.7. Figure 4.7 shows measurements of the etch depth, which is (459 ± 6) nm for the GaN and ~ 700 nm in total. These results confirm that the full thickness of GaN has been etched, due to there

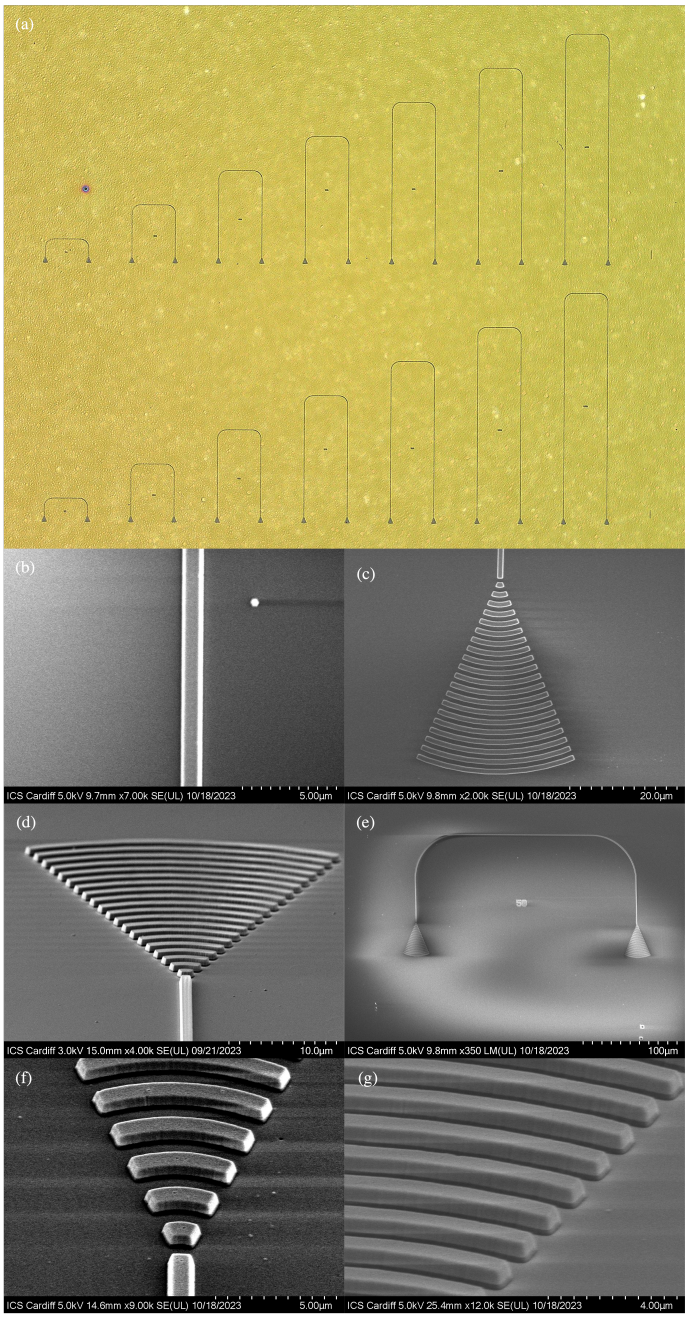

Figure 4.6: Fabricated cutback circuit. (a) optical micrograph of whole circuit. SEM images of GaN (b) waveguide (c) grating coupler and waveguide from top-down view (d) grating coupler and waveguide from angle (e) waveguide loop and grating couplers (f) close-up of a grating coupler, showing the surface morphology of the GaN, and (g) close-up of a grating coupler, showing the sapphire substrate (darker region) below the GaN, as the result of over etching. These devices were etched using ICP-RIE and a nickel hard mask, defined with nickel lift-off using PMMA exposed by e-beam lithography.

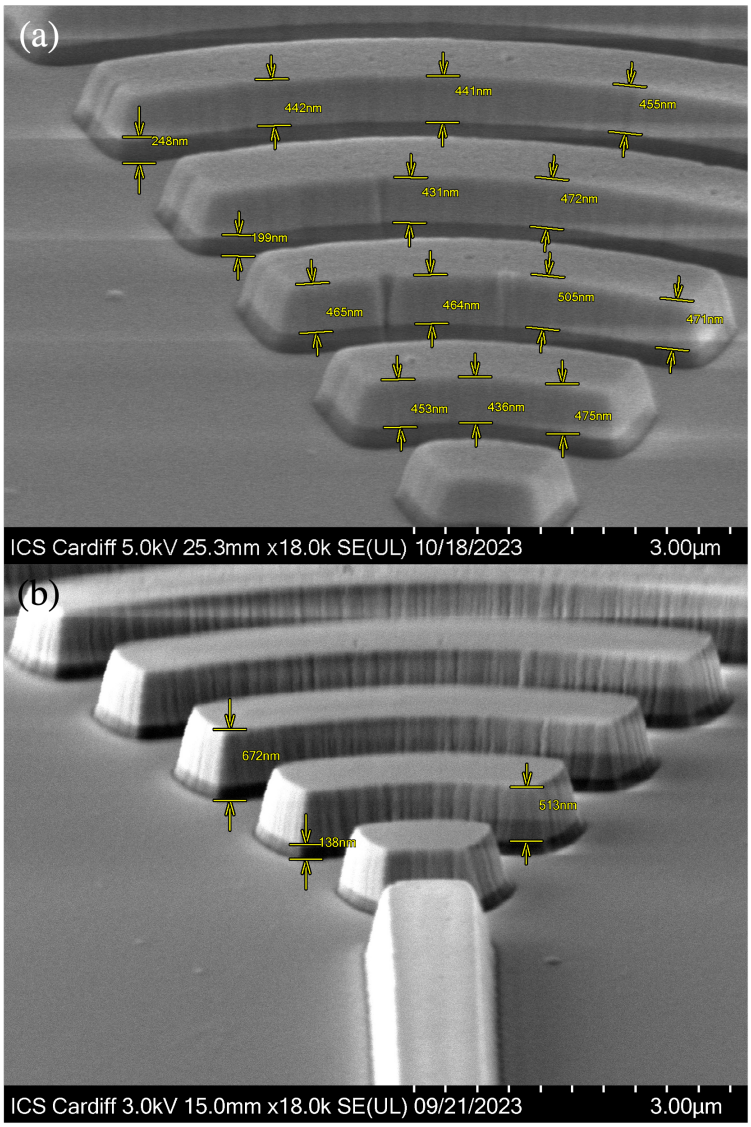

Figure 4.7: SEM images of etched grating couplers with measurements of etch depth. The measured GaN thickness in figure a is (459 ± 6) nm.

being two different layers of material, indicated by a top layer which is lighter in colour, thickness (459 ± 6) nm, and a second layer underneath, which is darker in colour, and has a visible depth of ~ 200 nm; the lighter material is GaN, and the darker material is sapphire. This hypothesis is supported by the thickness of the (fully etched) lighter material being ~ 500 nm, the specified thickness by the manufacturer. The etch time was 7 minutes, resulting in an etch rate of ~ 100 nm/min. Although the etch has continued into the sapphire, we are able to provide an upper bound of the selectivity of the etch using this nickel hard mask of ~ 23, a relatively high selectivity, as expected for a hard mask. Figure 4.6a shows a wide-view optical micrograph of the full fabricated circuit. As described above, this circuit contains looped waveguides of differing lengths coupled to grating couplers. The waveguide loops have different lengths so that the loss as a function of propagation length can be calculated using the cutback method [93].

When manufacturing waveguides, the dimensions should be "lithographically tuned" to achieve the desired width, as the lithography process (such as lithographic dosage and lift-off) may not have complete fidelity. The waveguides in figure 4.8 have a designed width of 765 nm, but the final manufactured versions are ~ 1100 nm. Although such waveguides are still single mode, the width should be corrected in the CAD file by approximately 350 nm.

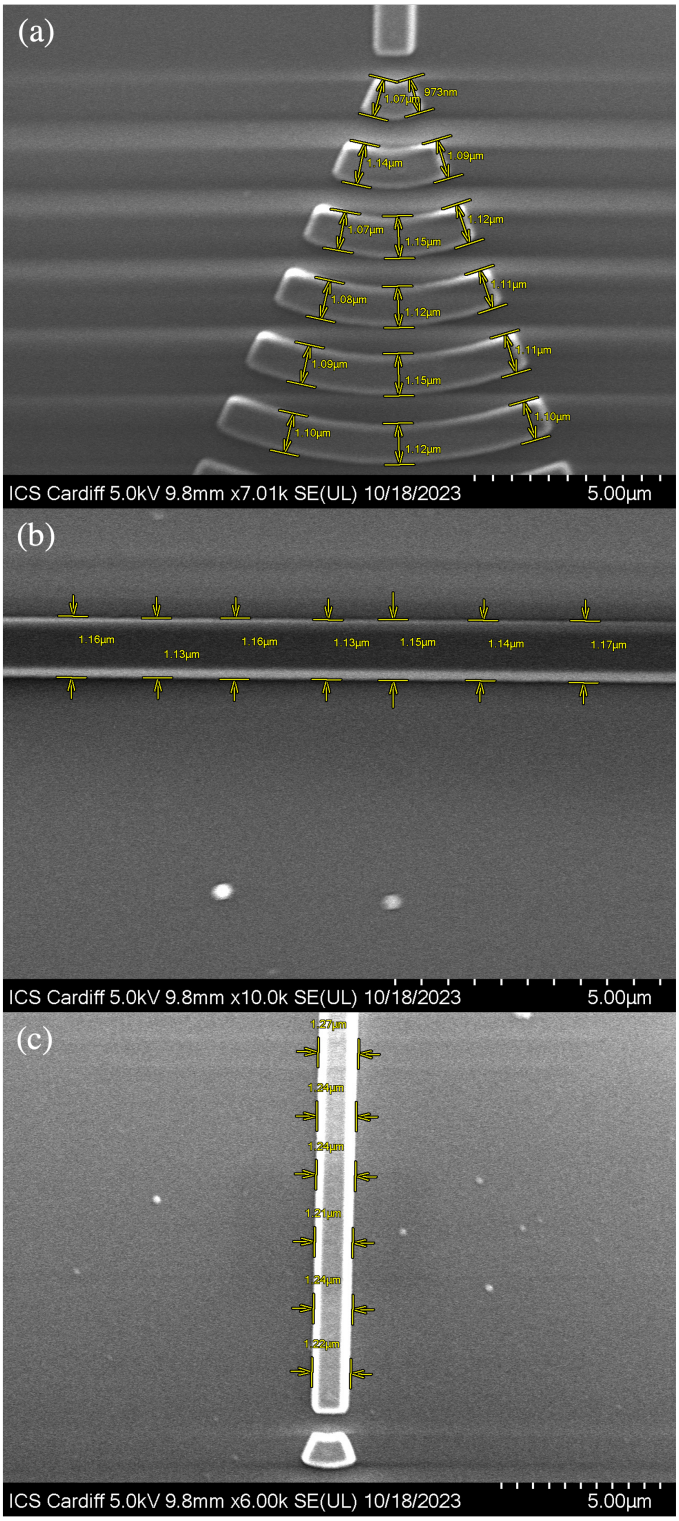

Figure 4.8: SEM images and measurements of waveguide widths.

4.3.2.1 Edge/Sidewall Roughness

As previously described, roughness in the sidewalls of a waveguide causes reflections and scattering of the optical mode, which decreases the efficiency of the device/circuit. Sidewall roughness can be transferred to the substrate either through the hard mask, which will have rough edges, or through the etch process itself. Different parameters of the etch process can be optimised for smoother sidewalls - a non-trivial process. It is harder to improve the roughness of the hard mask itself, except by changing the hard mask for a different material completely. Edge roughness in this case describes the deviation from a perfect straight line, or perfect curve, that may occur in the edges of the nickel hard mask. Although it is practically very difficult to have an atomically smooth nickel edge surface, we still must try to get as close as we feasibly can.

The SEM images in figure 3.4 illustrate the typical edge roughness of nickel from the lift-off process. When etched, this edge roughness then translates to rough/striated sidewalls. Figure 4.9 shows sidewall roughness/striations transferred to the sidewalls by the hard mask. Approximately $5 - 10$ striations μm^{-1} were measured in 4.9b and d. These images also demonstrates angled sidewalls, which we will now discuss.

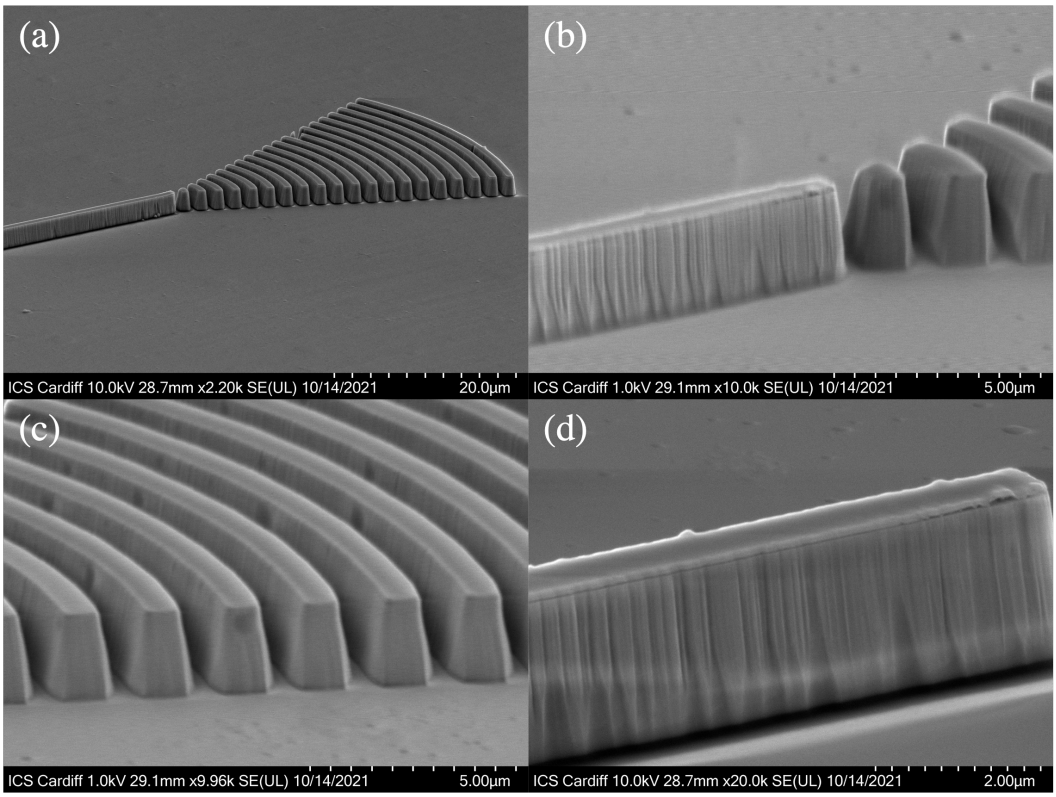

Figure 4.9: SEM images of etched 2 μm of GaN with a nickel hard mask. (a), (b) and (c) show the angled sidewalls. (b) and (d) clearly show the residual hard mask, as well as striations in the GaN sidewalls caused by the transfer of hard mask edge roughness from etching, which would lead to scattering loss.

4.3.2.2 Sidewall Angle Simulations

Figure 4.10 shows representative measurements of the sidewall angles of this etch. As seen, the waveguide sidewalls are not perfectly vertical, and are at an angle relative to the perpendicular of the substrate. The mean sidewall angle for these two images is $(16 \pm 3)^\circ$. As the angled sidewalls seen in figure 4.10 are a deviation from our intended design, it is possible that they will cause adverse effects in these devices. In this next subsection, we perform FDE simulations to investigate the effect sidewall angle has on an optical mode. Originally, our devices were simulated to have a perfectly rectangular cross-section. Because ICP etching is a combination of chemical (isotropic) and physical (anisotropic) etch processes, the etch recipe used may not achieve this. Ideally, a balance would be struck between etch parameters to optimise for a completely vertical etch. The results in this section should allow for the determination of whether angled sidewalls would be an issue in a fabricated device.

A range of quadrilateral waveguide cross-sections were simulated with a fixed upper width, $w = 765\,\text{nm}$, and the sidewall angle varied between them, with a schematic seen in figure 4.11b. The results of these simulations are seen in 4.11a and c. Angled sidewalls increase the size of the waveguide cross-section, and the mode 'fills out' the waveguide more. Figure 4.11a shows the increasing of effective refractive index of the mode with increasing sidewall angle. This result makes sense, as an increasing sidewall angle increases the cross-sectional area of the waveguide and there is more dielectric material for the mode to be supported in, raising the mode's effective index towards the material index of GaN (2.32), similar to the results in §4.2, and to be seen in §5.2. It is seen that a waveguide is single mode for the TE (TM) mode up to sidewall angles θ of $\sim 30^\circ$ ($\sim 40^\circ$). As the sidewall angle of the devices fabricated was measured to be $(16 \pm 3)^\circ$, we can predict that our fabricated devices would still be single mode in operation.

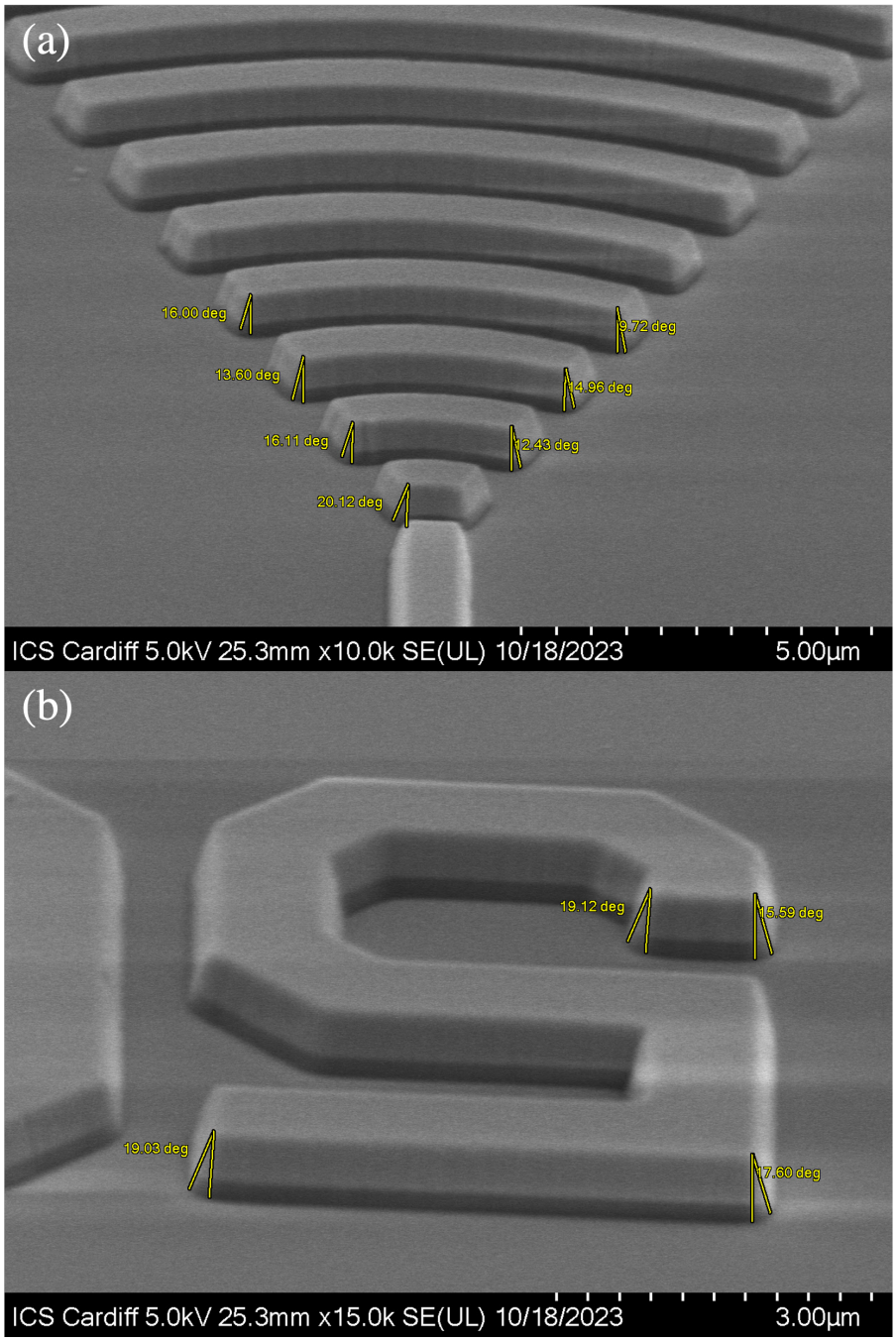

Figure 4.10: SEM images of etched devices, with sidewall angles measured. (a) is a grating coupler, and (b) is the number five. Note that these images were taken at a stage angle of $\sim 60°$, and these measurements are approximate. These angle measurements are to 2 decimal places because the native SEM operating software was used for these measurements, and they should be only considered to 2 significant figures. The mean sidewall angle for these images is $(16 \pm 3)°$.

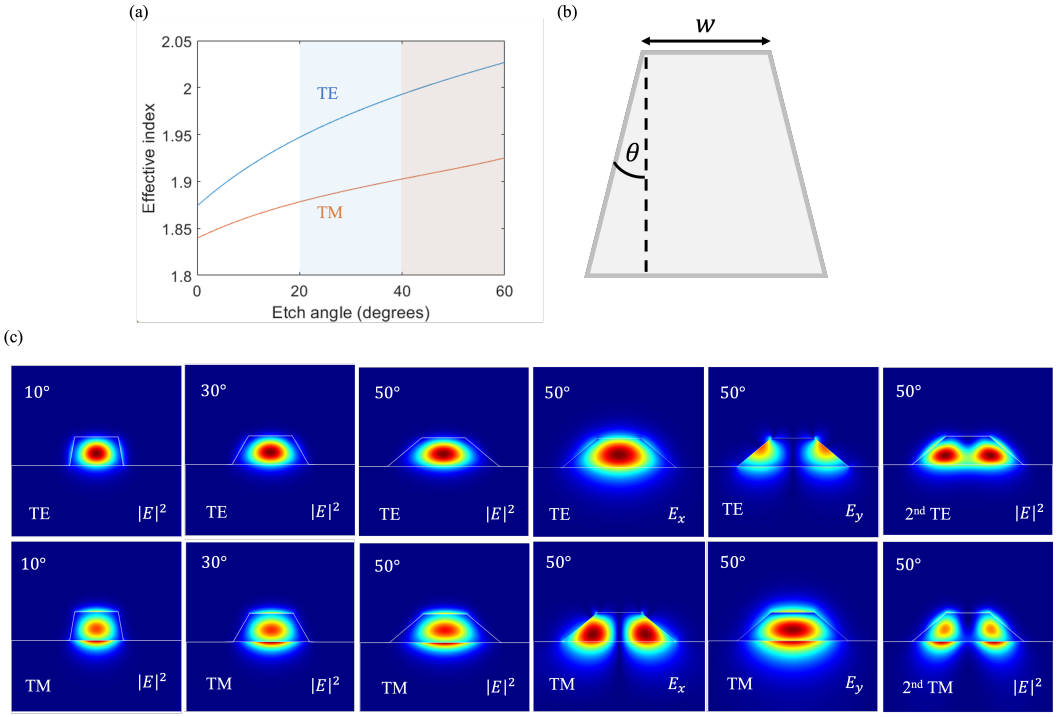

Figure 4.11: (a) Effective index versus waveguide etch angle, with the second order mode regions marked by blue and orange blocks for the TE and TM modes, respectively. (b) Schematic of waveguide sidewall etch angle, θ, and fixed upper waveguide width w, of 765 nm. (c) Mode profiles of representative results from sidewall angle simulations, including the E_x and E_y components for a waveguide with a sidewall angle of 50° showing $E_x \neq 0$ and $E_y \approx 0$ for the TE mode, and $E_x \approx 0$ and $E_y \neq 0$ for the TM mode. Far right: second order modes in waveguide with 50° etch angle. Results calculated using FDE.

4.4 Summary

By simulating the eigenmodes of rectangular GaN on sapphire waveguides over a wide range of widths and thicknesses, we have identified the waveguide geometries which only support fundamental modes, and the geometry boundaries for which higher order modes are supported. These results allow for a suitable device size to be chosen for fabrication in the single mode regime, and will be important for future studies on the simulation and fabrication of GaN waveguides. For the widest possible range of widths available for the fundamental TE and TM modes within this regime, a waveguide thickness of 500 nm was found suitable. For waveguides with a thickness of $\leq$ 200 nm, no optical modes are supported up to a width of 2000 nm. We have also simulated waveguides with a range of sidewall angles, and discussed the resulting increase in modal effective index. Following these simulations, GaN on sapphire waveguides were fabricated from 500 nm thick of GaN on a sapphire substrate using e-beam lithography, a nickel hard mask, and inductively-coupled plasma (ICP) reactive ion etching (RIE). Nickel was found to be an appropriate etch mask for GaN, with a measured selectivity of at least 23, resulting from an etch rate of $\sim$ 100 nm/min. We found that using a thinner layer of GaN allowed for a simpler nickel lift-off process and a thinner nickel hard mask (30 nm compared with 150 nm), which improved the device yield from $\approx$ 20% to $\approx$ 100%. We found the nickel lift-off process to be the largest contributor to device yield and fabrication success. Although the nickel lift-off process had a high yield, the design transferred to the hard mask had a width greater than the designed devices - 1100 nm compared to 765 nm - which caused etched devices to be wider than designed as a result.

Chapter 5

GaN Triangular Nanobeam Waveguides

5.1 Introduction

Most waveguides typically have a rectangular cross-section on a low index substrate like the ones described in the previous chapter. However, a low index substrate is needed for optical confinement, which can be an issue as not all semiconductors have (a range of) substrates that are both low index and lattice-matched, with lattice-matching reducing epitaxial growth strain and decreasing the number of defects in the crystal. As shown in references [45], [72]–[74], this issue can be solved by using the substrate as a sacrificial layer, chemically etching it away and leaving suspended rectangular nanobeams.

However, nanobeams with a triangular cross-section (henceforth also referred to as "triangular nanobeams"), shown in figure 5.1, pose an interesting solution to creating integrated photonic devices from semiconductor materials without low-index substrates. Triangular nanobeams, also suspending the nanobeam in air ($n = 1$), can be conveniently fabricated in a single physical etch by using a triangular prism Faraday cage in an ICP etching chamber [94], or by angled reactive ion beam etching [95], [96]. The ion dynamics of Faraday cage etching were simulated and studied by Latawiec et al. in 2016 [97]. They describe Faraday cage assisted ICP etching as working by "an equipotential developing at the cage boundaries, resulting in a field-free region inside the cage with electric fields pointing normal to its faces" - i.e., the electric field on the cage face directs the ions in the etch plasma

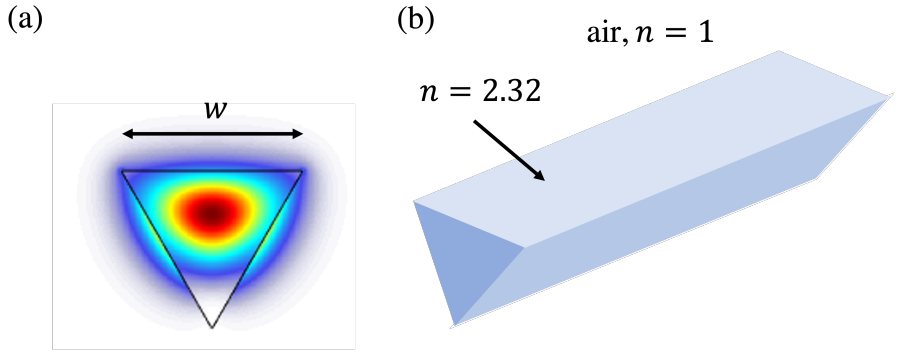

Figure 5.1: (a) TE mode of an equilateral triangular waveguide of width w, calculated using FDE. (b) Schematic of a triangular waveguide, showing the air cladding ($n = 1$), and GaN waveguide ($n = 2.32$).

to have a trajectory normal to the cage face, etching (and undercutting) the material at the desired angle. Once etching is complete, a nanobeam with a characteristic triangular cross-section remains. As mentioned, Faraday cage assisted angled etching is not the only possible method of fabricating triangular waveguides. Another method is reactive ion beam angled etching [95], [96], [98]. In this technique, the sample is vertically etched to the desired depth, the sample stage is tilted, and a second etch is performed at an angle, with the state rotated for etch uniformity [95]. Angled reactive ion beam etching has been demonstrated on the wafer scale with 8 samples in a 5-inch diameter on a 6-inch substrate holder, with a 5.4% and 2.9% variability in etch range and etch angle respectively across the wafer.

The first group to investigate triangular cross-section nanobeam waveguides studied them in diamond in a 2012 paper [99], in which they fabricated doubly-clamped cantilevers as a proof-of-concept for the angled etching fabrication technique. Some of the nanobeams fabricated are solid and some have a 1D array of periodic etch holes, intended to act as an optical cavity. Example SEMs of these nanobeam structures are shown in figure 5.2. As this was an early proof-of-concept for the fabrication technique, they did not characterise the optical properties of any of these structures. In the same paper they also experiment with a conical Faraday cage design, which was used to etch from all directions and to fabricate pedestals, nano-ring structures, and spiral nanobeams. They then followed up this work in 2014 [100], where they fabricated triangular cross-section racetrack resonators and PCNCs in diamond, and were able to optically characterise them using fibre taper coupling. SEM images of some of their devices are shown in figure 5.3.

Although triangular nanobeams are suspended above the substrate, they cannot literally be fully 'floating' above its surface - they must be attached to the substrate in some way. As seen in Figs.

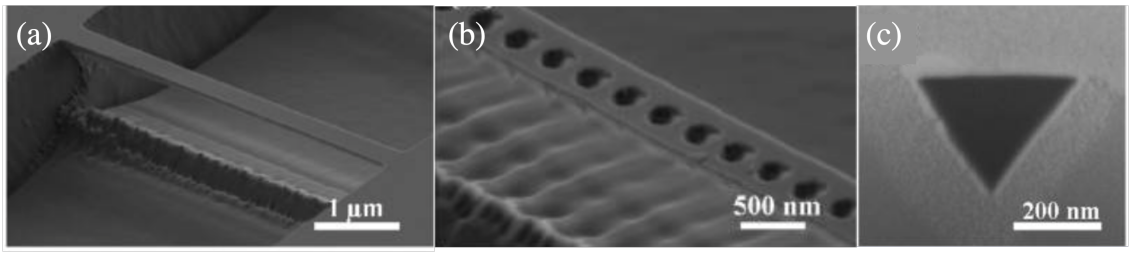

Figure 5.2: SEM images of a (a) suspended solid nanobeam, (b) suspended optical cavity and (c) FIB cross-sectioned $\sim 350\,\text{nm}$ wide solid diamond nanobeam taken from Ref. [99] to illustrate nanobeams fabricated using angled etching.

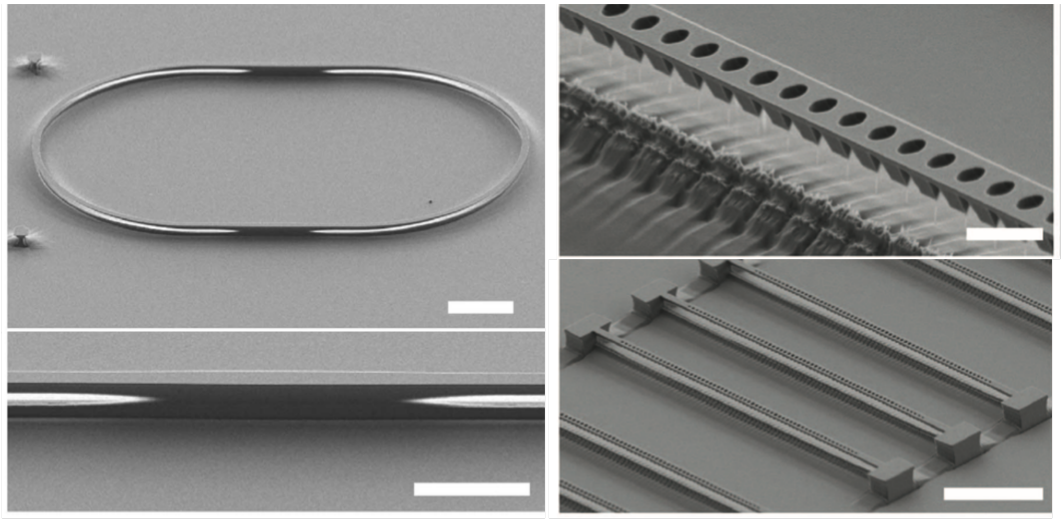

Figure 5.3: SEM images from Ref. [100] of optical devices fabricated in diamond using Faraday cage assisted angled etching. Left hand side: a $25\,\mu\text{m}$ bend radius racetrack resonator, with a close-up of the side view. Right hand side: photonic crystal nanobeam cavities with a close-up. All SEM images were taken with a 60° stage tilt.

5.2 and 5.3, convenient attachment and support can be in the form of large 'pads' either side of the nanobeam. However, this poses the question of how to join nanobeams together - which would be required for large-scale integrated circuits. Ref. [101] performed FDTD simulations to find out how a widened or tapered nanobeam supporting section, seen in figure 5.4, effects a triangular nanobeam mode, and how to optimise its design. They also experimented with supports on only one side of the nanobeam, and found that single-sided supports increased transmission efficiency, with a maximum value of 98.78%, compared to an already high maximum efficiency of 97.4% for a double-sided support. These values for efficiency are remarkably high, indicating that networks/circuits of suspended nanobeams would likely be possible and scalable. Ref. [101] notes that the optimal taper support shape or design is not necessarily consistent across different etch angles, and so taper designs need to be optimised for individual nanobeam designs and different materials. Although we have not studied this in GaN in this thesis, it is useful to know that losses due to supporting sections are low and can be optimised through simulations and parameter optimisation. A 2021 paper [102] also studied the waveguiding properties triangular nanobeams, but in SiC. Simulations were performed to investigate the effect nanobeam cross-section and wavelength has on a mode, and they found that as a nanobeam width is decreased relative to wavelength, optical confinement decreases. They also simulated changes in nanobeam etch angle.

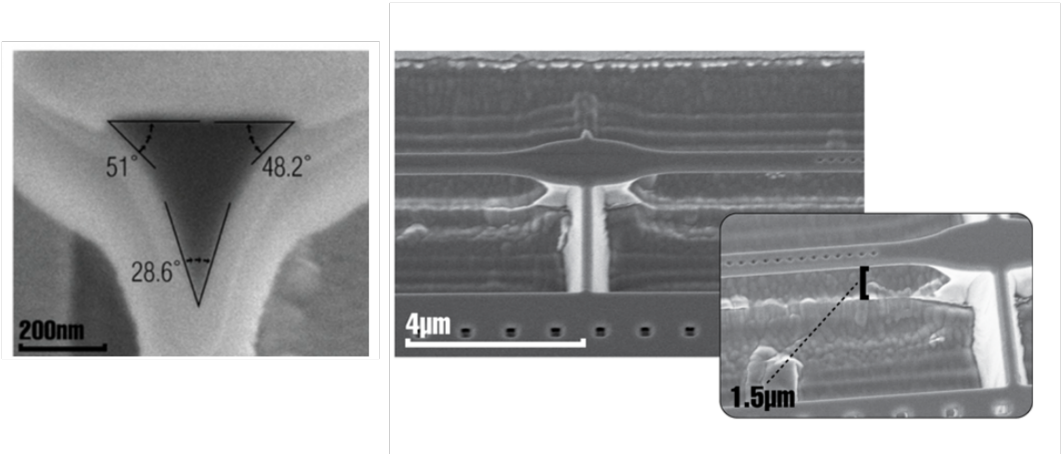

Figure 5.4: SEM images from Ref. [101]. Left: FIB made cross-section of a triangular nanobeam, with interior angles labelled (the lighter grey surrounding the nanobeam is redeposited platinum and diamond). Right: SEM of support structure and inset: measurement of nanobeam-substrate separation of $\sim 1.5\mu$m.

Homoepitaxial GaN, which is now available from commercial suppliers [92], would offer the highest possible crystal quality and thus theoretically PICs made of this material would have less intrinsic loss

and ideal for integrated photonics. However, as there is no low-index substrate, angled etching would be needed to create suspended triangular nanobeams to provide optical confinement. As seen in section 1.4, suspended rectangular cross-section GaN nanobeams have been demonstrated in the literature, using a selective chemical etch. However, to the best of our knowledge, the only previously reported GaN triangular nanobeam study is a 2020 paper [94], which fabricated singly- and doubly-clamped cantilevers in GaN using Faraday cage angled etching, seen in figure 5.5. Ref. [94] also included effective index simulation results for a range of nanobeam widths, which planted the seed for this chapter of my thesis, with these results first highlighting the possibility of GaN triangular nanobeams being used for integrated photonics.

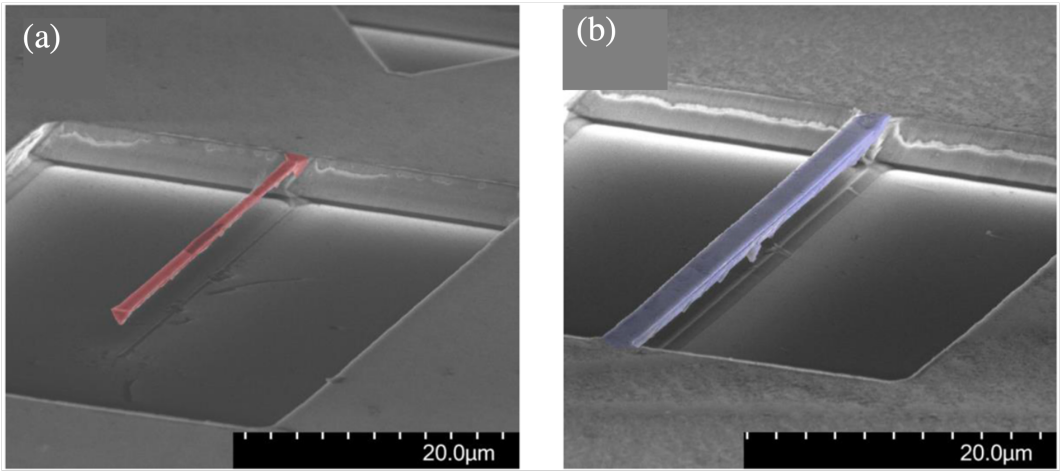

Figure 5.5: False-colour SEMs of GaN (a) singly- and (b) doubly-clamped suspended cantilevers. These images are from Ref. [94].

In this chapter, we study how changes in the cross-sectional geometry of triangular GaN nanobeams affect the optical modes supported. We will also describe the manufacturing tolerances for nanobeam width, etch angle, and asymmetry, as well as the minimum distance the substrate must be from the suspended nanobeam. Eigenmode calculations will be shown for triangular nanobeams of varying cross-sectional geometry, using the same commercial simulation software [76] and techniques as in section 4.2. Although our results are for gallium nitride at 1550 nm, these results can be qualitatively applied to other materials and wavelengths.

5.2 Effect of Nanobeam Width on the Optical Mode

To the best of our knowledge, there has been no investigation in the literature simulating different triangular nanobeam widths and the effect width has on waveguide modes. $|E|^2$ intensity profile results have been reported with a fixed width and four different wavelengths [102] which produced somewhat analogous results, however this is only qualitatively analogous, and to the best of our knowledge no quantitative study exists.

We begin our investigation by performing FDE simulations of triangular nanobeams the width of all three sides ranging from 400 to 1000 nm. To visualise the optical mode and confinement of the nanobeams, the absolute value of the electric field intensity, $|E|^2$ of the nanobeam cross-section is used. The purpose of the simulations in this section is to determine the nanobeam width that would be appropriate to fabricate based on the three conditions of (1): single mode operation, (2): high optical confinement, and (3): minimal overall dispersion. Figure 5.6a shows the $|E|^2$ profiles of the fundamental TE and TM modes for equilateral triangle nanobeams of width $w = 600$ nm, 760 nm and 1000 nm, as well as the E_x and E_y components of the TE and TM modes for a 1000 nm wide nanobeam, showing $E_x \neq 0$ and $E_y \approx 0$ for the TE mode, and $E_x \approx 0$ and $E_y \neq 0$ for the TM mode. Figure 5.6b shows the confinement of each mode as a function of WG width, with confinement given by 2.38 and defined here as the percentage of $|E|^2$ that is within the nanobeam compared to the total $|E|^2$. Figure 5.6b shows that optical confinement increases as nanobeam size increases, with the dielectric material being more able to support the mode. The TE mode is positioned slightly higher than the TM mode, expectedly, due to the TE mode being horizontally oriented, and requiring more dielectric material in the horizontal direction. This phenomenon is opposed to the TM mode, which is vertically oriented, and so does not need to be higher up to take advantage of the larger areas of dielectric material there. The TE mode is slightly ($\sim 2\%$) more confined to the nanobeam than the TM mode.

Figure 5.7a shows the effective index versus nanobeam width for these simulations of triangular nanobeam widths. Our results show the TE and TM modes as being degenerate in effective index, with effective indices of the modes being within 0.01% of each other for all nanobeam widths considered. As this behaviour is observed for a wide range of nanobeam widths and with a high degree of precision, we can likely rule out that this is a coincidence, and is instead due to symmetry. This result is notable - such degeneracy may be expected in a square cross-section with a fourfold symmetry, but here we also observe it in a triangular cross-section nanobeam waveguide with fewer axes of symmetry, despite the TE mode being slightly more confined to the nanobeam core than the TE mode. Optical modes

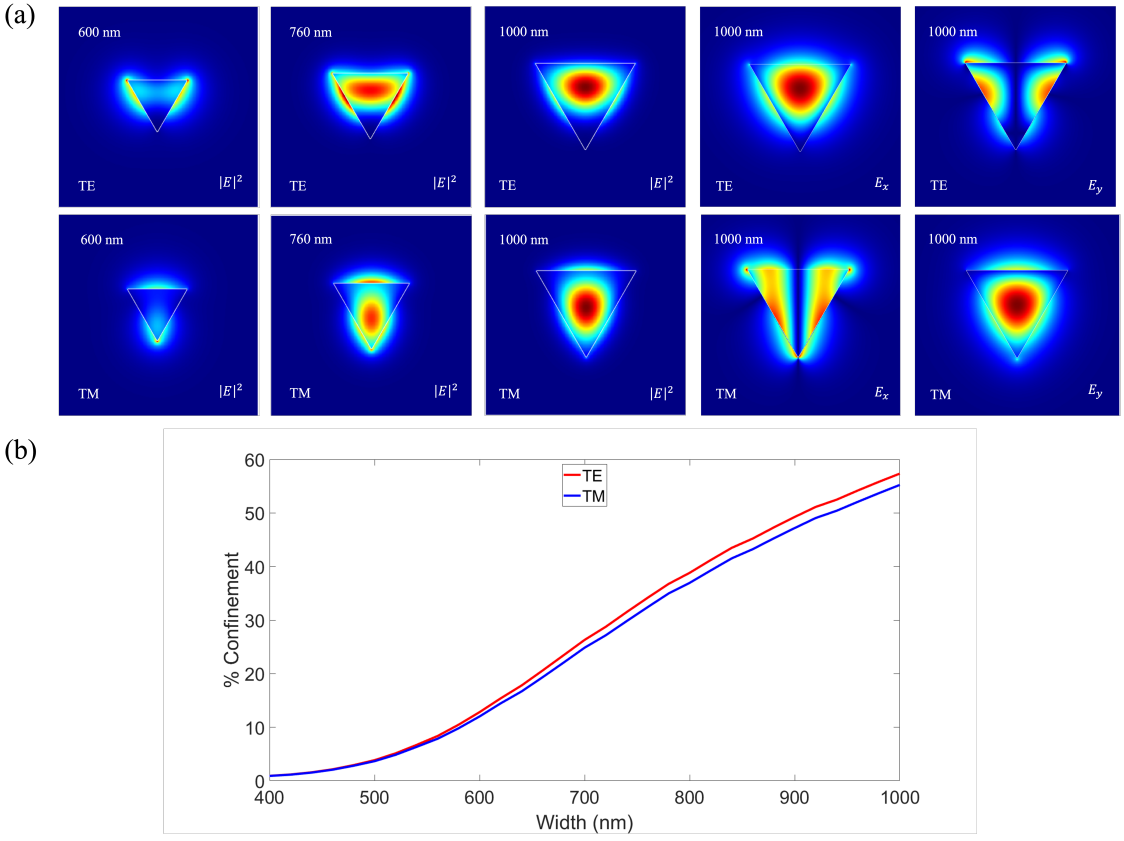

Figure 5.6: (a) Mode profiles of fundamental TE (top row) and TM (bottom row) modes of equilateral triangle nanobeams of widths 600, 760 and 1000 nm, showing optical confinement increasing with nanobeam size. The E_x and E_y fields are plotted for a 1000 nm wide nanobeam, showing $E_x \neq 0$ and $E_y \approx 0$ for the TE mode, and $E_x \approx 0$ and $E_y \neq 0$ for the TM mode. The white outline is the boundary of the nanobeam. (b) Confinement of TE (red) and TM (blue) modes with increasing nanobeam width. Results calculated using FDE.

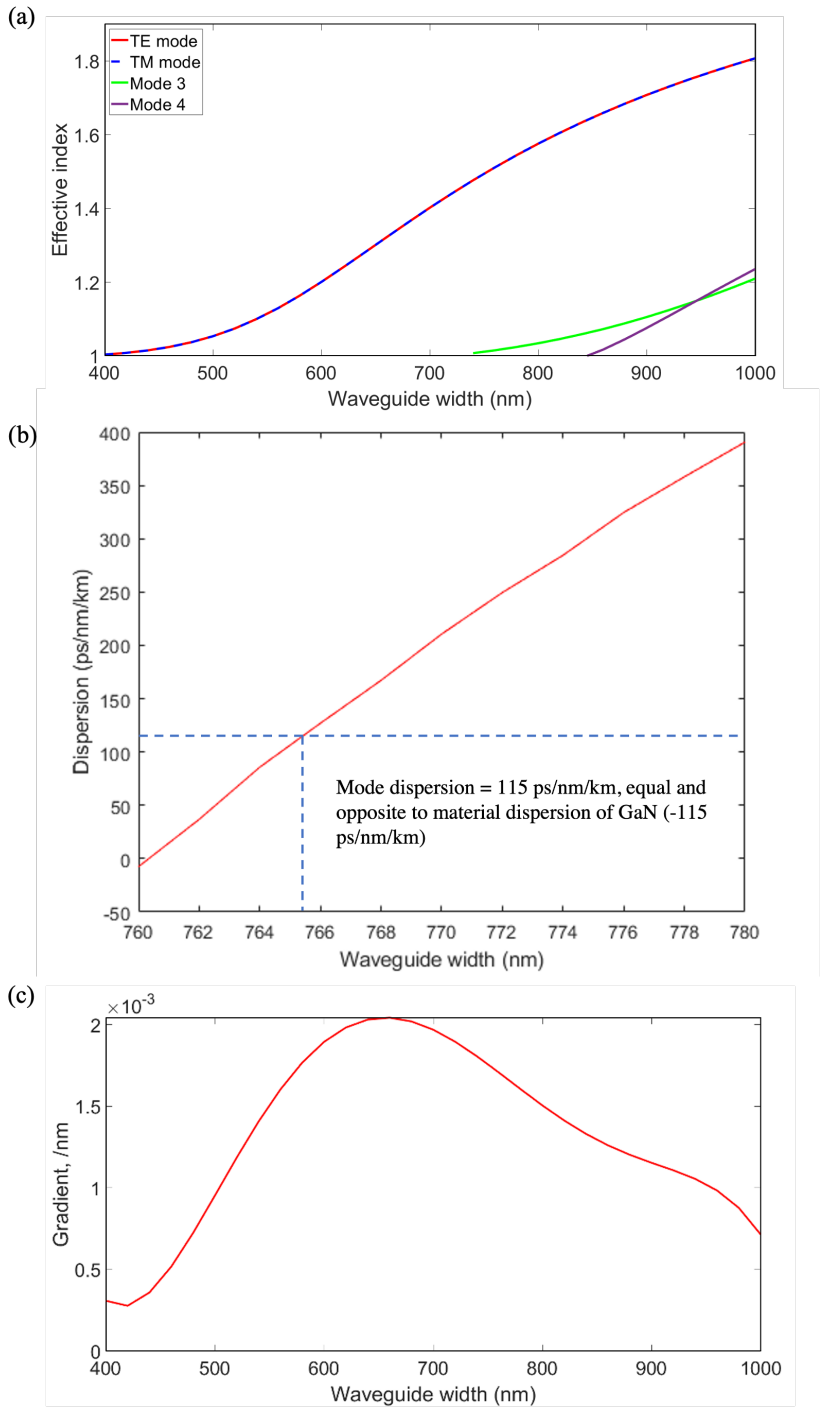

Figure 5.7: Simulation results for triangular nanobeams of varying widths. (a) Effective index against nanobeam width for first four modes. Modes 1 and 2 are the first TE and TM modes, respectively, which are degenerate in effective index. Modes 3 and 4 are hybrid modes. (b) Mode dispersion against nanobeam width for equilateral triangular WGs of widths between 720 and 840 nm, for the fundamental TM mode. Dashed blue line marks where the waveguide dispersion is equal and opposite to the material dispersion of GaN, which is −115 ps/nm/km. (c) Gradient of data in (a), as a function of nanobeam width.

are supported for nanobeams with width greater than 400 nm, although confinement is weak, shown in figure 5.6. For our size range, four modes are supported: the fundamental TE mode, fundamental TM mode, and two higher order modes, labelled mode 3 and mode 4 in figure 5.7. The two higher order modes are hybrid TE/TM modes with $\sim 50:50$ TE:TM ratios. $|E|^2$ profiles for these two hybrid modes are seen in figure 5.8. Mode 3 is supported for nanobeams with width greater than 720 nm, and mode 4 is supported for nanobeams with width greater than 860 nm. Figure 5.7 also illustrates the increase in optical confinement with width seen in figure 5.6, with the increasing effective index illustrating the mode index being closer and closer to the material index of GaN (2.32).

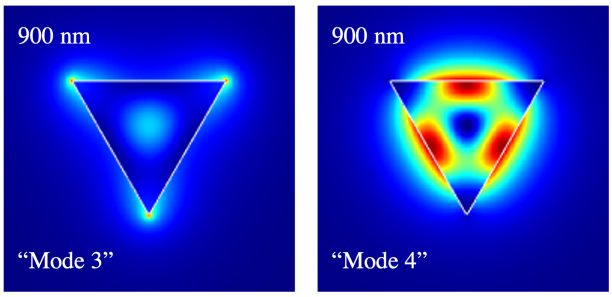

Figure 5.8: Higher order modes supported by a triangular nanobeam calculated using FDE, with an 800 nm wide nanobeam shown here. The TE:TM fractions are $\sim 50:50$ for these modes. The index of mode 3 is 1.1051 and has a TE fraction of 0.5, and the index of mode 4 is 1.0754 and a TE fraction of 0.5.

5.2.1 Near-Zero Dispersion Point

Group velocity dispersion (GVD) describes the extent to which the different frequency components of light in an optical device will travel at different speeds and spread out in time as the light propagates through the device. Having a near-zero GVD is beneficial for applications such as information processing, where the broadening of signals reduces the available/allowable data detection/transmission rate of a circuit. To the best of our knowledge, no discussion of the near-zero-dispersion point of triangular nanobeam waveguides has taken place in the literature before our work. The near-zero dispersion point of a waveguide is the point at which the intrinsic material group velocity dispersion is approximately equal and opposite to the modal group velocity dispersion; the total dispersion in the waveguide is approximately zero. The near-zero dispersion point therefore acts as an appropriate goal to aim for in a waveguide if it is possible, as a light source will not be a perfect delta function - it will have some bandwidth/spectral broadening. The material dispersion in GaN at 1550 nm is -115 ps/nm/km [89]. Therefore, a target nanobeam design would have a modal dispersion of $+115$ ps/nm/km. Figure

5.7b shows the nanobeam width (765 nm, marked by dashed lines) with this dispersion, at which point the material dispersion is counteracted, i.e., the near-zero waveguide dispersion point. A nanobeam waveguide of this geometry would have approximately zero overall dispersion, and would therefore be a good/appropriate nanobeam geometry to choose for fabrication. As the modal dispersion is very sensitive to waveguide size, shown in figure 5.7b with a change of only 1 nm resulting in a dispersion change of $\sim 20\,\mathrm{ps/nm/km}$, the overall dispersion in a fabricated waveguide will not likely be zero, but we can aim for it to be as close to zero as possible, which is what we have done here.

5.2.2 Manufacturing Tolerances

In this section, we will present results highlighting to what extent deviations in a triangular nanobeam width effect the mode's effective refractive index. Based on calculations of the gradient of effective index against nanobeam width, it is possible to evaluate how the variability in fabrication processes may affect the effective index of manufactured nanobeam waveguides. These results will also give an idea of how far away a device may be in terms of intended functionality, based on its deviation from the prescribed geometry; this change would have an effect on the effective index of the mode, and by proxy knock-on effects in a device, for example on the efficiency of grating couplers and quality factor of cavities. To the best of our knowledge, there is no literature on the deviations in triangular nanobeam waveguide cross-section and its effect on effective index, and how this relates to intended device design versus fabricated structure.

To determine the variation of effective index with respect to nanobeam width, the gradient of figure 5.7a was calculated. The data was considered to be the same for both the TE and TM modes, due to their degeneracy in effective index. The tolerance coefficient, given by the gradient, at $w = 765\mathrm{nm}$ is $(0.0017 \pm 0.0008)\,\mathrm{nm^{-1}}$. For our devices, a WG of width 765 nm has an effective index of 1.52, meaning that, for example, a 1% change in effective index (from 1.52 to 1.50 or 1.54) would occur from a change in nanobeam width of $(9 \pm 4)\,\mathrm{nm}$, and a 5% change in effective index would occur from a change in nanobeam width of $(45 \pm 20)\,\mathrm{nm}$. However, it is seen in figure 5.7a that the tolerance coefficient is not constant, which will clearly have an effect on these calculations if your intended device width is different to our example of 765 nm. The coefficient as a function of nanobeam width (figure 5.7c) will help determine the tolerances at any value of designed nanobeam. For example, the nanobeam widths with the least and most tolerance to change are 420 nm and 660 nm, respectively, with values of $0.28 \times 10^{-3}\,\mathrm{nm^{-1}}$ and $2.0 \times 10^{-3}\,\mathrm{nm^{-1}}$, respectively.

The structures in the literature [95], [97], [99], [100], [103] appear to have uniform widths, with little variance. Ref. [103] describes a mean etch angle of $(53.5 \pm 2)^\circ$ across over 500 devices, indicating good device uniformity through angled etching (using Faraday cage angled etching). However, it is not confirmed whether 53.5° was the targeted angle; as seen in §4, adjustment of the fabrication process is often needed to align intended device design with actual fabricated devices. In angled etching, this would be achieved by adjustments to the ICP etch bias, changes to the Faraday cage design, or calibration/tuning of the stage angle, depending on which method of angled etching is employed.

5.3 Etch Angle and its Effect on an Optical Mode

To the best of our knowledge, the only investigation into triangular nanobeam etch angle and its effect on waveguide modes is the previously mentioned Ref. [102]. However, only the $|E|^2$ intensity profiles of the modes were discussed without mention of effective index, and only three different etch angles were calculated. We will now calculate and discuss a wide range of angles, towards the boundaries of practical to manufacture devices.

As discussed in §5.1, the etch angle can be affected by several different factors, such as ICP conditions and Faraday cage design [97]. For an investigation of how etch angle effects the optical mode, triangular nanobeams were simulated with an upper angle θ simulating etch angle in the range of 40° to 80°. As these nanobeams are symmetric, both upper angles of the nanobeam are the same. The width of the nanobeams was kept a constant of $w = 765\,\text{nm}$. The height of the nanobeam is equal to $h = \frac{w}{2}\tan\theta$. Figure 5.9a shows the mode profiles for example nanobeams, and figure 5.9b shows the confinement for the TE and TM modes. At small θ values, little of the field is contained within the nanobeam, and most of the mode evanescently decays in the air cladding, particularly in the TM mode; confinement is poor in the TM mode until an etch angle $\theta < 60^\circ$, meaning that if the etch angle is fixed and limited to 60° by fabrication equipment available, then a wider device design is needed. If a wider device design is needed, then mode simulations should be undertaken taken based on the individual/particular etch requirements to determine the size of nanobeam needed to support the optical mode.

Figure 5.10 shows the effective index versus nanobeam angle for the fundamental TE and TM modes. The TE mode has an approximately linear relationship, and the effective index is greater than the TM mode for nanobeam angles below 60°, corresponding to better optical confinement, seen in figure 5.9. The modes then switch at 60°, with the TM mode having the higher index and

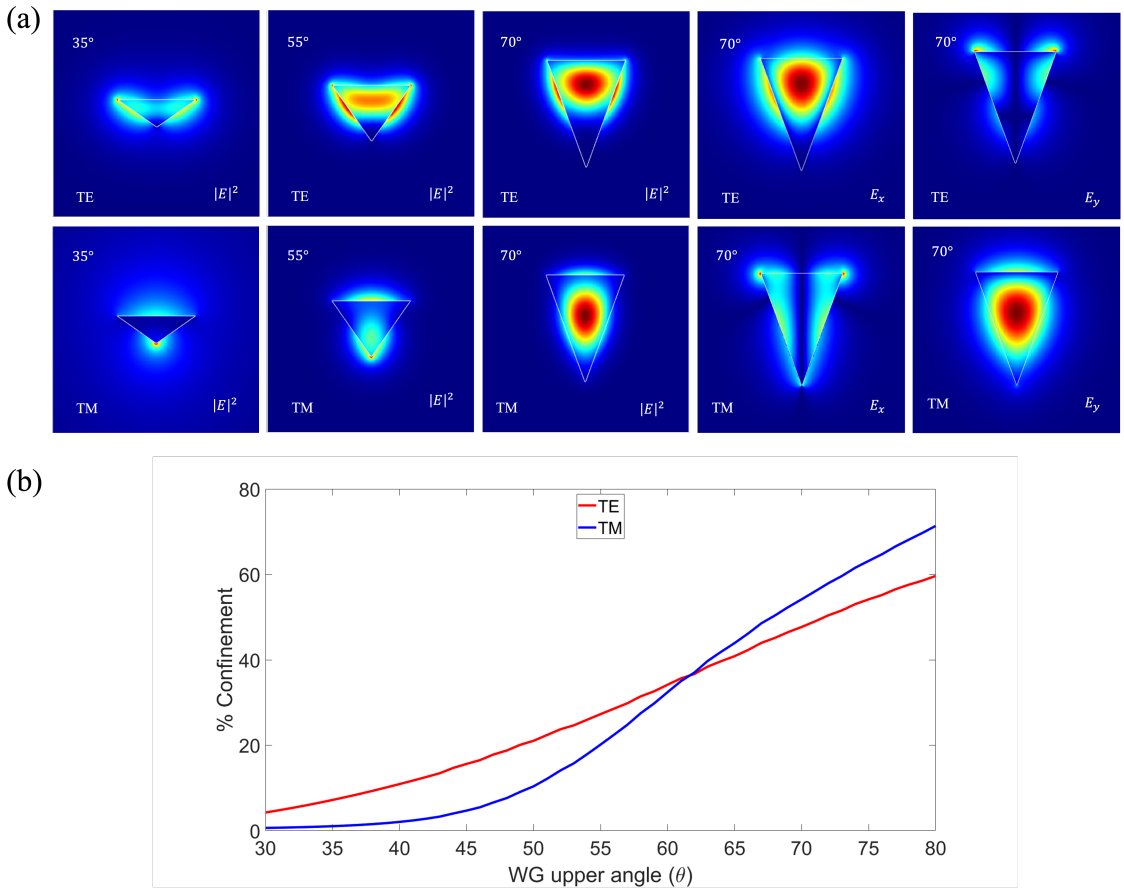

Figure 5.9: (a) Mode profiles of fundamental TE (top row) and TM (bottom row) modes calculated using FDE for nanobeams of angle, θ, of 35°, 55°, and 70°. The first three columns show the $|E|^2$ profiles. The final two columns show the E_x and E_y profiles of a nanobeam of $\theta = 70$, showing $E_x \neq 0$ and $E_y \approx 0$ for the TE mode, and $E_x \approx 0$ and $E_y \neq 0$ for the TM mode. (b) Nanobeam core confinement of the TE (red) and TM (blue) modes.

better confinement, approximately characterised by the lesser proportion of evanescent field outside the nanobeam. Generally, the effective index increases with an increasing nanobeam angle, with the dielectric increasing in cross-sectional area and being more able to support the light, similar to §5.2 also. In figure 5.10 we also again observe the TE and TM modes being degenerate for an equilateral cross-section ($\theta = 60°$). This degeneracy is lifted, and the waveguide becomes birefringent with diverging effective indices when the cross-section is no longer equilateral, suggesting that the degeneracy is linked to the symmetry in an equilateral cross-section nanobeam, which is broken when the etch angle is changed.

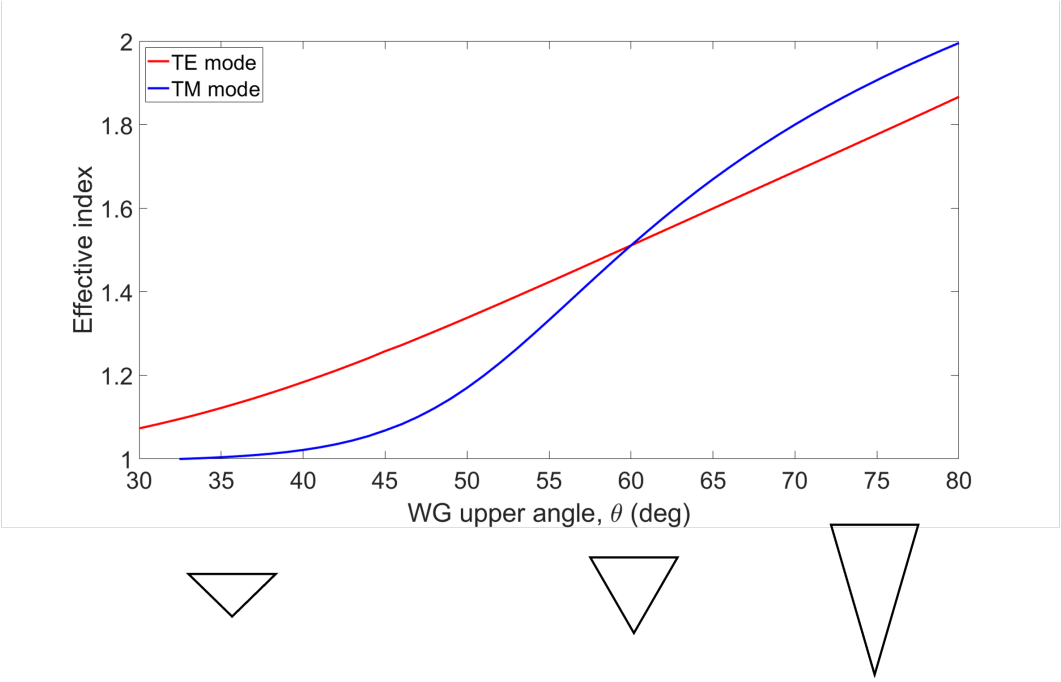

Figure 5.10: Effective index against nanobeam angle, θ. Triangles below the x-axis illustrate how θ effects nanobeam geometry. Effective index calculated using the FDE method.

5.3.1 Manufacturing Tolerances

These tolerances describe the relationship between a change in etch angle and the change in the effective index of an optical mode. The gradient in figure 5.10 at 60° is (0.0176 ± 0.00017) per degree for the TE mode and (0.0349 ± 0.0041) per degree for the TM mode. As an example, a 1° change would result in a change in effective index of 1% for the TE mode and 1% for the TM mode.

Ref. [103] describes a mean etch angle of $(53.5 \pm 2)°$ across over 500 devices, indicating good device uniformity through angled etching (using Faraday cage angled etching). However, it is not confirmed whether 53.5° was the targeted angle; as seen in §4, adjustment of the fabrication process is often needed to align intended device design with actual fabricated devices. In angled etching, this would be achieved by adjustments to the ICP etch bias, changes to the Faraday cage design, or calibration/tuning of the stage angle, depending on which method of angled etching is employed. Ref. [100] observed a blue-shift in their cavity resonance of roughly 5% of their targeted values that they attribute to an uncertainty in etch angle of up to 2° of the nominal value, but despite this deviation they still measured high Q factors of $\sim 183,000$. Ref. [97] state their angled etch results were accurate to within 1°.

5.4 Effect of Asymmetric Etching on a Mode

After angled etching, it may be possible for an asymmetric etch to occur; this could be unintended, for example due to imperfections in the etch cage [97], or it could be achieved deliberately. To the best of our knowledge, there currently does not exist any literature on the effects of asymmetry on triangular nanobeam waveguides. As such, we will now present the first study of this kind.

The effects of asymmetry on the mode profiles of the fundamental TE and TM mode are seen in figure 5.11a, and the effects on confinement are shown in figure 5.11b. The nanobeam cross-sections are defined based on the relative position of the bottom vertex, illustrated in the panels below the axis in figure 5.12. Triangular nanobeams were simulated with a triangular cross-section and width of 765 nm, for a range of bottom vertex positions ranging from $-w/2$ (all the way to the left, see panels beneath axis for illustration) to $+w/2$ (all the way to the right), each representing a different asymmetric etch. The mode profiles at a displacement of 0 are the same as those of an equilateral nanobeam, as in §5.2. The E_x and E_y profiles in the final two columns of figure 5.11a indicate that the TE and TM modes become less polarised and more hybrid when they are asymmetric, supported by TE fractions of ~ 0.6 and ~ 0.4 for the TE and TM modes, respectively.

Figure 5.12 shows the effect of introducing asymmetry on the effective index of the mode. The TE and TM modes begin degenerate in effective index when there is no asymmetry (i.e. the waveguide is equilateral), consistent with figures 5.7a and 5.10. When this equilateral symmetry is broken and asymmetry is introduced, the waveguide becomes birefringent and the modes diverge, no longer being degenerate. This observation further points to the TE and TM modes being degenerate in an equilateral cross-section nanobeam, as a result of a symmetry which is broken when the cross-section is changed. As the nanobeam becomes more asymmetric, the effective index of the TE mode increases, from ~ 1.5 to ~ 1.6, whereas the TM mode decreases in effective index, from ~ 1.5 to ~ 1.4. Both the TE and TM modes have a similar, slightly non-linear relationship, but the TM mode changes to a greater extent overall, ~ 0.16 compared to ~ 0.08. This behaviour is further visible in the $|E|^2$ profiles in figure 5.11, with the mode profile of the TM mode appearing to be less confined with increased asymmetry, whereas the mode profile of the TE mode appears to get better confined. The relationship between bottom vertex displacement and optical mode is symmetric in the positive and negative direction, as would be expected due to the geometry of the waveguides.

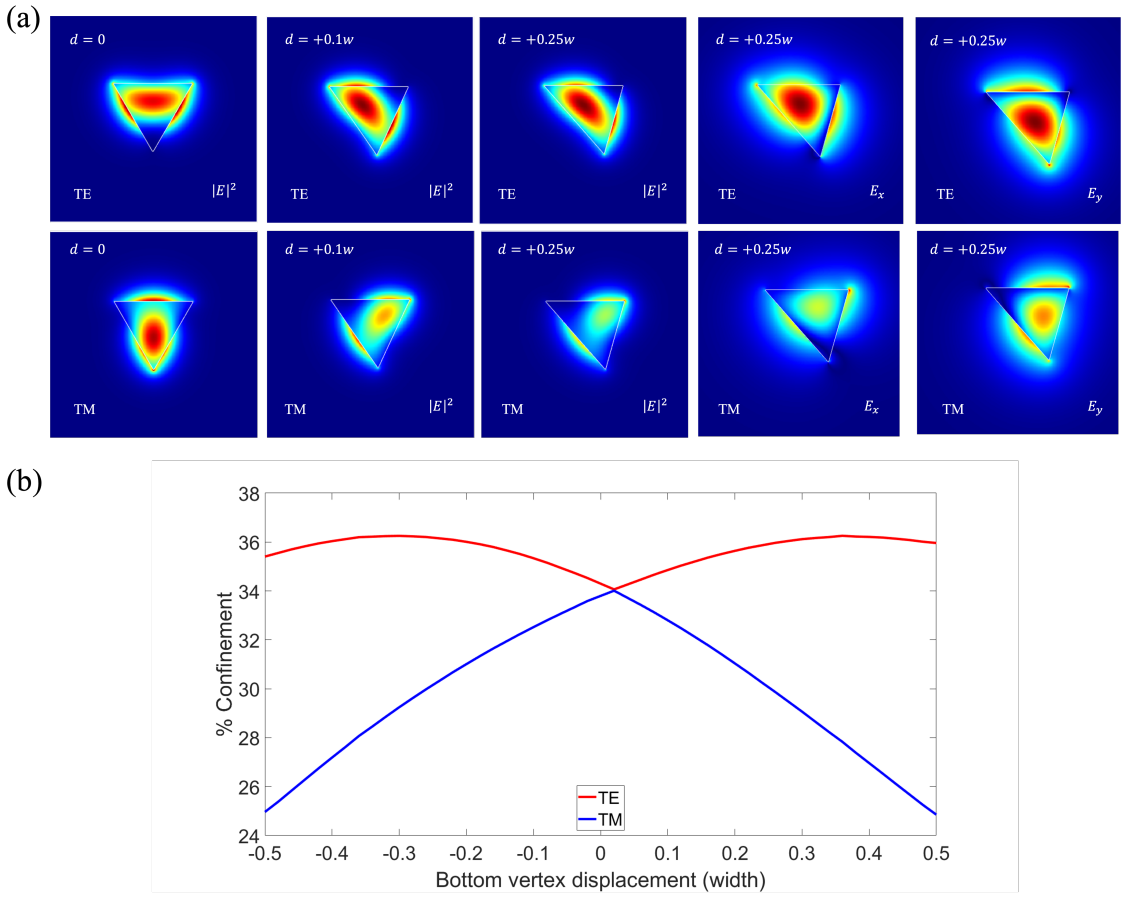

Figure 5.11: (a) Mode profiles of fundamental TE (top row) and TM (bottom row) for representative bottom vertex displacements, d, of $0.1w$, and $0.25w$, with $d = 0$ also plotted for reference. Displacements of $\pm$ any value are reflections of each other with the vertical as the axis of reflection. $|E|^2$ profiles are shown in the first three columns. E_x and E_y profiles are shown in the final two columns, and indicate the TE and TM modes becoming less polarised and more hybrid, supported by TE fractions of ~ 0.6 and ~ 0.4 for the TE and TM modes, respectively. (b) Nanobeam core confinement for the TE (red) and TM (blue) modes. This relationship is symmetric, as would be expected for this symmetrical change in cross-sectional geometry. Results calculated using FDE.

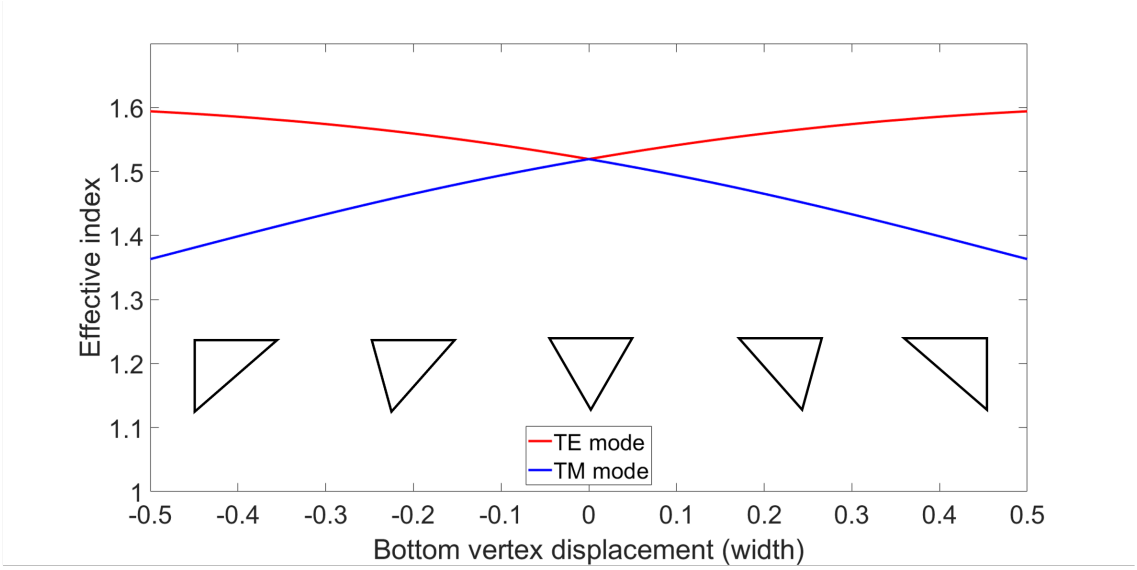

Figure 5.12: Effective index as a function of bottom vertex displacement from centre, calculated using FDE, with TE and TM modes labelled. This relationship is symmetric, as would be expected for this symmetrical change in cross-sectional geometry. The schematic above the legend illustrates how bottom vertex displacement effects the nanobeam cross-section.

5.4.1 Manufacturing Tolerances

These tolerances describe the amount of asymmetry that may occur in a nanobeam before a particular change in the effective index is observed. In order to calculate the gradient, the data in figure 5.12 was fitted for only positive displacement of the bottom vertex, but due to the symmetry, this result can also be applied to a negative displacement. The gradient at a displacement of $0.02w$ is $(0.2287 \pm 3.7 \times 10^{-5})\, w^{-1}$ for the TE mode, and $(-0.2390 \pm 6.9 \times 10^{-5})\, w^{-1}$ for the TM mode (the reason we consider the gradient at a displacement of 0.02 and not, for example 0, is because we consider a displacement of 0 to be a point of inflection, with a gradient of 0, as a result of the symmetrical relationship of effective index with nanobeam geometry). These results give a measure for how much the index of a mode may be changed due to asymmetry from etching. As an example, a 1% change in effective index occurs for a bottom vertex displacement of $(0.11 \pm 1.8 \times 10^{-5})\, w$ for the TE mode and $(0.12 \pm 3.5 \times 10^{-5})\, w$ for the TM mode. These index changes of 1% represent a bottom vertex displacement of 84 nm and 92 nm for the TE and TM modes, respectively, which is relatively large. As such, triangular nanobeam waveguides are likely to be resistant to negative effects on optical modes due to asymmetry.

5.5 Effects of Nanobeam-Substrate Proximity

If an angled etch has been under-etched, then a triangular 'foot' or 'stump' remains present in the substrate underneath the suspended nanobeam, with examples seen in figure 5.2. As this foot is also a dielectric material, it is possible for light to evanescently couple to it, which would be a parasitic loss and make a device less efficient. As the separation between nanobeam and foot is dependant on the etch time, the effect the proximity of the foot has on the optical device is needed to be studied, so that appropriate etch times/depths are known prior to fabrication, which is the motivation for these simulations. To investigate the effect the substrate (foot) beneath a suspended nanobeam has on an optical mode, a triangular nanobeam and substrate were simulated with varying separation, d, between the top of the nanobeam and the top of the substrate, with a schematic seen in figure 5.13a. As the shape of the substrate is also the result of angled etching, it will have a profile/geometry determined by the etch angle. Figure 5.13b shows a schematic of how the angled profile is formed for a single step angled etch, alongside the equation for finding the substrate angle, ϕ, also displayed in equation 5.1 (from [94]). Figure 5.13c, also from Ref. [94], shows a SEM after a partial angled etch, nicely illustrating the profile of the 'foot'. Using equation 5.1, the substrate foot formed by fabricating an equilateral triangle nanobeam (i.e. nanobeam interior angle $= 90° - \theta = 60°, \theta$ = etch angle $= 30°$), has an angle ϕ equal to 11°. For a triangular nanobeam 765 nm wide, this equals a substrate 'foot' height of 662.5 nm (the same as the nanobeam height) and a width of 6817 nm.

$$\tan\phi = \frac{1}{3\tan\theta} \tag{5.1}$$

Figure 5.14 shows the results of simulating nanobeams with differing separations from the substrate. The triangular foot was positioned 'on top' of a rectangular section of sapphire - extending beyond the simulation region. There are no modes supported in the nanobeam for a separation below 50 nm. It is observed in figure 5.14a that there is little change (0.00075/0.05%) in the TM mode after this critical separation, with the effective index converging to a value of 1.5183 after a separation of approximately 300 nm. The TE mode has a greater change in index, with the proximity of the substrate increasing the index by 0.01 ($< 0.5\%$), before converging to a value of 1.5184 at a separation of approximately 600 nm. These results indicate that triangular nanobeams do not have to be over-etched significantly to provide efficient confinement, with a minimum separation of 50 nm between nanobeam and substrate needed for the fundamental modes to be supported in the nanobeam, with the effective indices of the

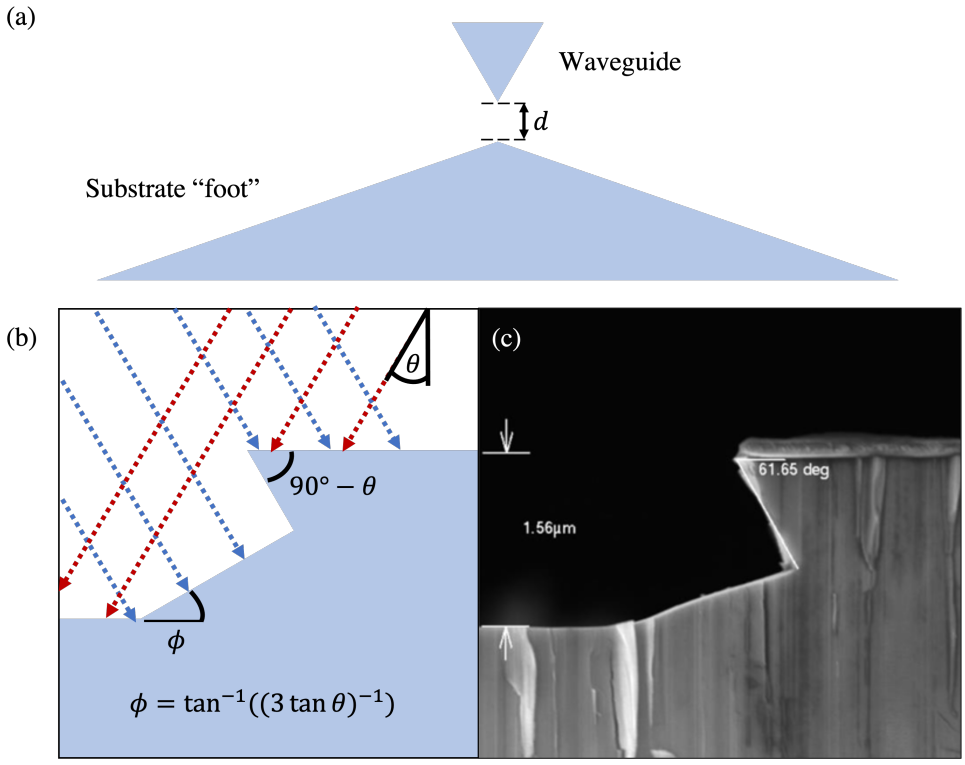

Figure 5.13: Top: schematic of a triangular nanobeam and substrate residual "foot" as a result of under-etching, with d, "tip-to-tip" separation between nanobeam and substrate, marked. Bottom-left: SEM image from Ref. [94] of a cleaved cross-section of a partially-angled-etched GaN nanobeam, included for a reference for this chapter to a physical device. Bottom-right: schematic of how ions incident at an angle θ cause an interior nanobeam angle of $90° - \theta$ and a substrate "foot" angle of $\phi(= \tan^{-1}((3\tan\theta)^{-1})$ (eq. 5.1).

TE and TM modes changing by less than 1% compared to an isolated nanobeam. Figure 5.14b shows $|E|^2$ profiles for a nanobeam and substrate with a separation of 50 nm, showing the similarity with an isolated nanobeam waveguide.

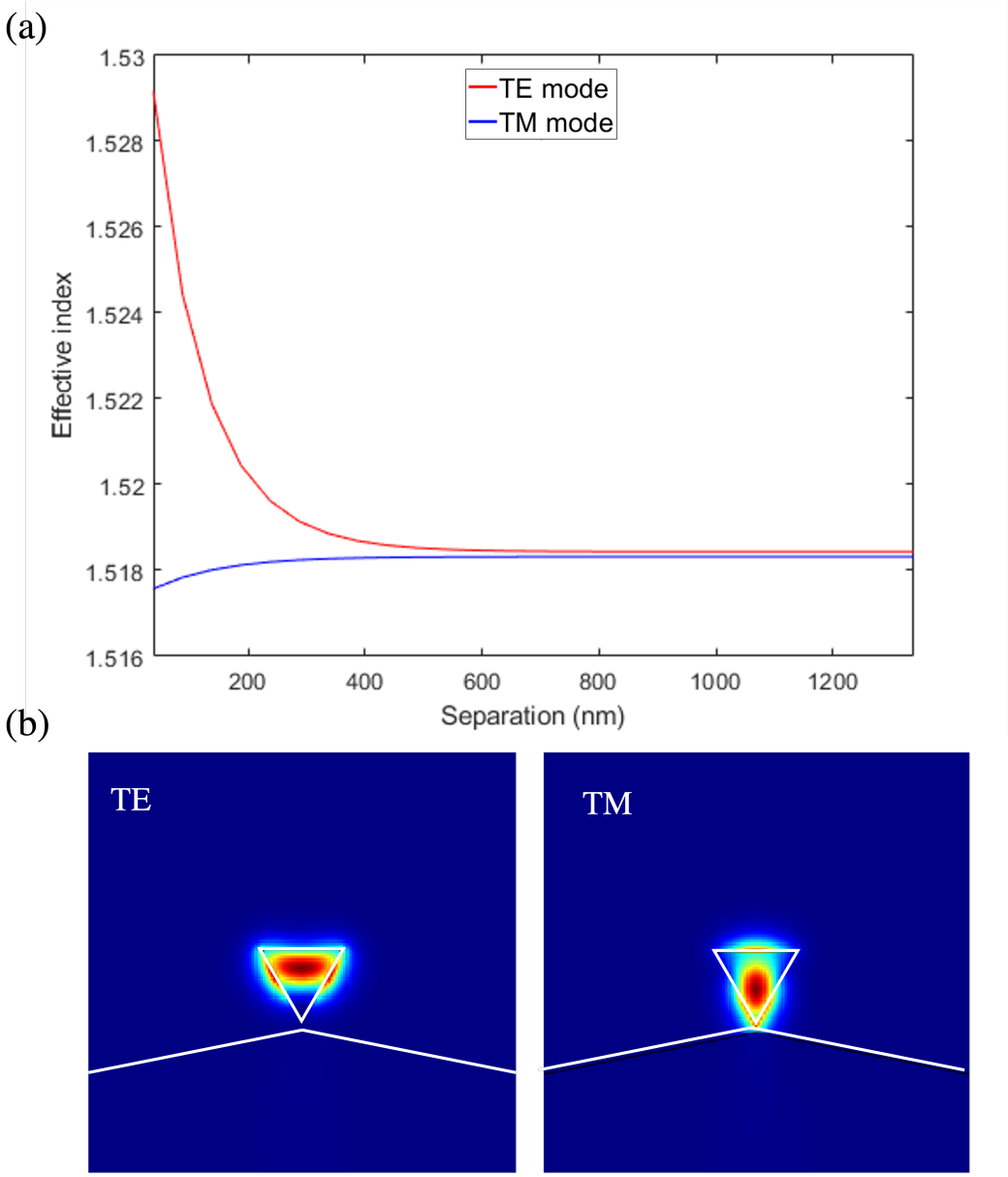

Figure 5.14: (a) Effect of nanobeam-substrate separation on mode effective index, calculated using FDE. (b) $|E|^2$ profiles of the fundamental TE (left) and TM (right) modes for a nanobeam-substrate separation of 50 nm.

5.6 Summary

We have presented the first in-depth study into the effects that variations in triangular nanobeam cross-sections have on waveguide modes. The effective indices of the fundamental TE and TM modes are seen to be degenerate for a triangular nanobeam waveguide with an equilateral cross-section, with a waveguide becoming birefringent when the nanobeam cross-section is altered away from equilateral. The effect etch angle has on a mode has been studied, with a steeper etch angle causing a larger nanobeam cross-section, and higher optical confinement. Conversely, a shallow etch angle causes a smaller cross-section and less confinement. These results allow insights into how well a fabricated device may perform in practice. We found that a minimum nanobeam width of 400 nm is required for optical modes to be supported in an equilateral triangular nanobeam at a wavelength of 1550 nm. A nanobeam with a 765 nm wide equilateral cross-section was found to be an appropriate target for fabrication, as it has an overall group velocity dispersion of approximately zero due to the material dispersion of GaN being approximately cancelled out by the modal dispersion. The perturbation effects of the substrate underneath the nanobeam were simulated, with the optical mode having little parasitic loss into the substrate.

Chapter 6

GaN Triangular Photonic Crystal Nanobeam Cavities

6.1 Introduction

Photonic crystal nanobeam cavities (PCNCs) are a small-footprint method of enhancing matter-light interactions on an integrated photonic platform [104]. PCNCs are a form of Fabry-Perot resonator/cavity, with light being reflected back and forth by a pair of distributed mirrors either side of a central 'cavity' region. The mirrors in a PCNC are regular changes in dielectric material geometry, leading to reflections. These mirrors can be a 1D array of holes etched into the nanobeam, as shown previously in figures 1.5, 5.2 & 5.3, or modulated changes in width, which are not as common. When the geometry of these mirrors is designed in an appropriate way, with features on the order of quarter the wavelength of light, a photonic bandgap occurs, resulting in a stop-band of higher reflectivity, with modes with frequency within the bandgap being forbidden, and remaining in the cavity.

Triangular cross-section PCNCs, which are PCNCs made using suspended triangular nanobeams like the waveguides described in the previous chapter, were first demonstrated in diamond in 2012 [99] and shown previously in figure 5.2. In 2021, Ref. [102] studied triangular PCNCs in a different material, SiC, in which they simulated coupling to colour centres for light emission in quantum information processing (QIP) networks. They followed this work up in 2022 [105], where they simulated a large network of these colour centre-coupled PCNCs for the generation and manipulation of photonic qubits. Room temperature quantum emitters have recently been observed in GaN [106], which

could be enhanced in an integrated circuit by a PCNC, with networks of PCNCs coupled to emitters similarly to Refs. [102], [105] forming the basis of QIP networks. As shown in sections 1.4 and 5.1, rectangular cross-section suspended GaN PCNCs have been demonstrated in the literature, [45], [73], and GaN triangular nanobeams have been fabricated [94]. However, there is currently no literature on triangular cross-section GaN PCNCs.

In this chapter, we outline the principles behind designing a triangular cross-section width-modulated GaN PCNC, calculate the mirror strength of PCNC DBR mirrors in relation to their geometry, describe and assess two methods of calculating Q factor, demonstrate the saturation of Q factor with cavity length, and outline a method of simulating loss in a PCNC. We then attempt to improve on the cavity design by apodising the cavity mode by gradually the mirror strength profile, in order to increase the cavity Q factor.

6.2 Triangular Distributed Bragg Reflector PCNCs

Distributed Bragg reflectors (DBRs) are the basis of perhaps the simplest PCNC design; consisting of alternating quarter-wavelength thick layers with higher and lower refractive indices, DBRs cause the constructive interference of light and create a 'stop-band' with high reflectivity at the targeted wavelength. A Fabry-Perot cavity can be formed by placing two DBRs, which act as the mirrors, adjacent to a half-wavelength spacer layer, which maintains the phase of the light and acts as a localisation region for the cavity mode. A schematic of a triangular cross-section DBR PCNC is shown in figure 6.1, with side and top-down views shown in figures 6.1a and b showing the widths w_1 and w_2, lengths a_1 and a_2, and effective indices n_1 and n_2 of the wide and narrow nanobeam segments, respectively, as well as the length L of the central half-wavelength spacer. A 3D model is shown in figure 6.1c. For constructive interference, the effective indices n_1 and n_2 and lengths a_1 and a_2 of each segment must satisfy the Bragg condition, 6.1

$$n_1 a_1 = n_2 a_2 = \lambda/4, \tag{6.1}$$

where n_1 and n_2 are a function of the nanobeam widths w_1 and w_2 respectively, which can be calculated by FDE simulations as we have previously demonstrated in §5. Due the mode of a 765 nm wide nanobeam having approximately zero overall dispersion (calculated in §5.2.1), we have selected a w_1 value of 765 nm resulting in an index n_1 of 1.52. We then select a second width w_2 of 600 nm as it has

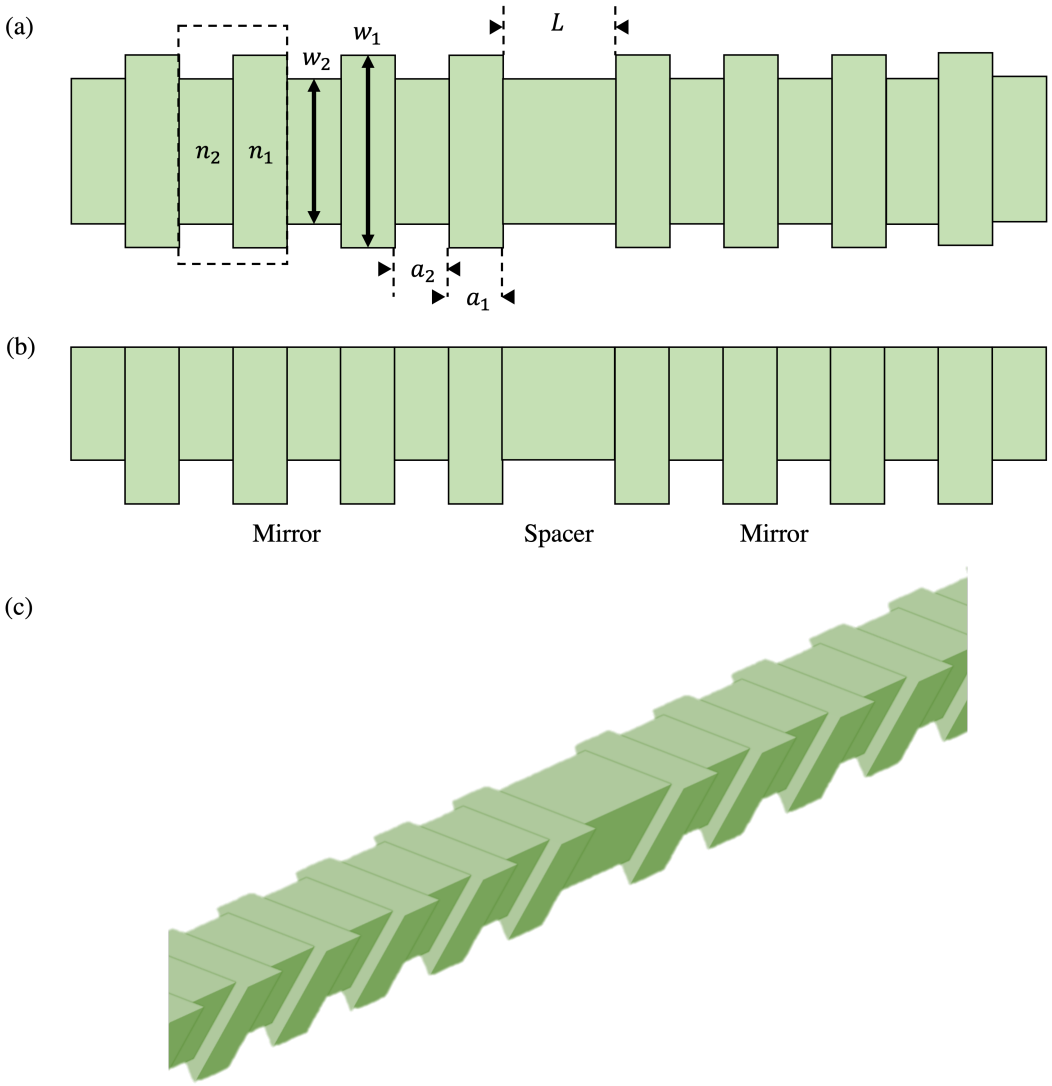

Figure 6.1: (a) Top-down schematic of a width-modulated Bragg cavity. The dashed box indicates a single period unit of the mirror, n_1 and n_2 are the effective indices of the two different nanobeam widths, w_1 and w_2 are the two different nanobeam widths, and a_1 and a_2 are the lengths of each segment. (b) side view of the same structure with mirror and spacer regions labelled. (c) 3D model of a width-modulated Bragg cavity with central spacer.

both high optical confinement (shown in figure 5.7a) and a high index contrast with n_1, with an index n_2 of 1.20. Using equation 6.1, we get lengths of $a_1 = 255\,\text{nm}$ and $a_2 = 323\,\text{nm}$. The central cavity is a half-wave spacer layer of length L where $na = \lambda/2$, where either $n = n_1$ and $a = a_1$, or $n = n_2$ and $a = a_2$. In our design, we choose $n = n_2 = 1.20$, and $a = a_2 = 323\,\text{nm}$. We have now outlined the basic design of a triangular cross-section DBR cavity, and will now move on to evaluating our design.

6.2.1 Filling Fraction of Triangular PCNC DBRs

The filling fraction (FF) of a DBR mirror can be defined as the fractional area of the narrower nanobeam section, a_2, compared to the total period of the mirrors $a_1 + a_2$:

$$\text{FF} = \frac{a_2}{a_1 + a_2}. \tag{6.2}$$

Changing the FF changes the optical pathlength of each section, which in turn changes the phase and leads to reflections in the nanobeam. Earlier, we calculated the lengths a_1 and a_2 of the wide and narrow sections of DBR mirrors that satisfy the Bragg condition, as 255 nm and 323 nm respectively. A DBR of this design therefore has a FF of 0.559. As we change the FF and move away from the Bragg condition, the mirror strength in the DBR should decrease

6.2.2 Mirror Strength of Triangular PCNC DBRs

One of the crucial properties of a DBR mirror is its mirror strength, γ, a measure of how strongly light is reflected by the DBR. Having a DBR with the highest γ is needed for higher quality cavities, and occurs at the Bragg condition. When light is incident on a DBR mirror at a wavelength in the stop-band, propagation is forbidden and some light is reflected, and some light exponentially decays into the mirror. The envelope of this decay in the mirror can be defined as

$$E(x) = E_0 e^{-\gamma x}, \tag{6.3}$$

where $E(x)$ is the field of the light in the mirror along the propagation axis x, and E_0 is the field of the light incident on the mirror, i.e., the field of the source. The higher the value of γ, the stronger the decay in the mirror, with the decay of $E(x)$ being able to be measured in a simulation. We will now use the FDTD method to simulate a range of DBRs with differing mirror filling fractions (FF) and calculate γ for each, which will allow us to (1), verify whether a cavity design with this FF will

result in the highest mirror strength and therefore Q factor, and (2), allow us to attempt to apodise the cavity to increase Q further.

Figures 6.2a and b show a schematic of the simulation setup from the top and side, respectively. The FDTD simulation consisted of a source injecting the fundamental mode from a uniform-width ($w = 765\,\text{nm}$) nanobeam section towards a DBR mirror. The purple line in figure 6.2c shows the placement of the source, the green box shows the mirror region, the yellow box shows the uniform region, and the blue box indicates E as a result of reflections from the mirror. The light source has a wavelength $\lambda = 1543\,\text{nm}$, chosen as a result of broadband simulations of these devices. Light propagates towards the DBR, and exponentially decays within the mirror, according to equation 6.3, with an example of this decay shown in figure 6.2c. To calculate the mirror strength γ, the natural log of the E signal along the centre of the DBR (where E is at its maximum) is then taken, shown in figure 6.2d, with this slope equalling $-\gamma$. We then normalise γ to the total period of each mirror segment, $a_1 + a_2 = 578\,\text{nm}$.

Triangular nanobeams of varying FFs were simulated in Lumerical FDTD [76] and the mirror strengths calculated for each FF. The results of these simulations are shown in figure 6.3, with errors estimated from the error in the linear fit. We observe that there is a point of maximum γ, with γ decreasing approximately quadratically away from this maximum and reducing to zero, at which point light no longer decays in the width-modulated nanobeam and is able to propagate through the nanobeam. This result is in good agreement with the literature [107]. The maximum γ is at the Bragg condition, and decreases as the FF moves away from the Bragg condition. As seen in figure 6.3, mirror strength is highest ($\gamma = 0.151 \pm 0.017$) for a mirror with an FF of 0.567. This is slightly different to the calculated Bragg condition of FF = 0.559, $\gamma = 0.149 \pm 0.016$, however this is still within the error tolerance. We will now use a grating with this FF to construct a cavity.

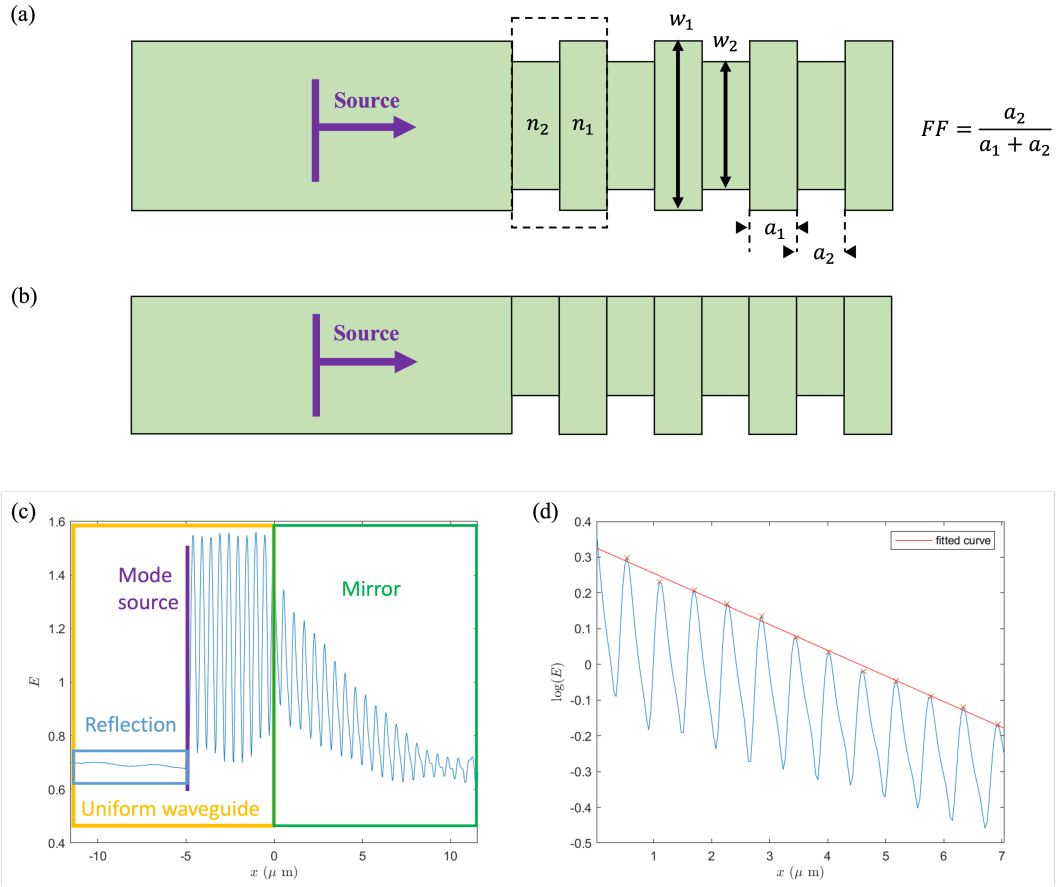

Figure 6.2: (a) Top view and (b) side view of simulation setup to calculate mirror strength of width-modulated nanobeams, with formula for filling fraction (FF) shown. (c) $|E|^2$ profile along the x (propagation) axes along the width-centre of the nanobeam, with different elements labelled. The purple line shows the placement of the source (which injects the fundamental mode into the device), the green box shows the mirror region, the yellow box shows the uniform region, and the blue box indicates the $|E|^2$ as a result of reflections from the mirror. (d) Natural logarithm of the exponential decay of $|E|^2$ in the mirror region (green box in figure c), with the gradient being used to calculate the mirror strength of a particular mirror size. This gradient is then normalised to the period of the mirrors, 578 nm.

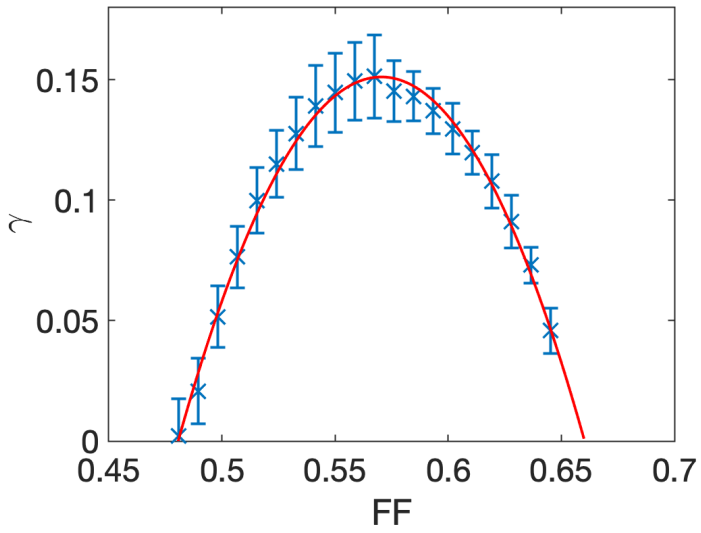

Figure 6.3: Mirror strength γ with error bars, normalised to the mirror periodicity, 578 nm, as a function of the filling fraction FF of the narrow nanobeam section. Calculated from FDTD simulations.

6.2.3 Q Factor of a PCNC Cavity

Following the calculation of the mirror design with the highest mirror strength in §6.2.1, we have designed triangular cross-section PCNCs with these parameters and will investigate their Q factors. The main figure of merit of an optical cavity is the quality factor, also known as the Q factor, or Q. The Q factor encapsulates the overall 'quality' of a cavity, describing the lifetime of a photon within the cavity. The Q factor is a fundamental metric used to evaluate the performance of resonators and is crucial in applications such as lasers, filters, and sensors. For example, in optical filters, a high-Q resonator leads to sharper and more selective spectral responses, and in sensors, a high-Q cavity increases the sensitivity and resolution of the sensing mechanism.

We will now outline how to use FDTD simulations to calculate the Q factor of a DBR cavity using two different methods, and show how Q factor of a DBR saturates with increasing cavity length. We will compare and contrast these two methods in the context of performing FDTD simulations. We will then present a method of calculating simulated loss in a DBR, and examine its effect on Q factor.

6.2.3.1 Calculating Q Factor

The Q of a cavity can be calculated in several ways. In the first we will consider, Q can be expressed as a dimensionless decay rate, defined as the ratio of energy stored in the cavity and the energy loss

per cycle,

$$Q = 2\pi \frac{E_{stored}}{E_{loss}}, \tag{6.4}$$

where E_{stored} is the optical energy stored in the cavity, and E_{loss} is the energy lost from the cavity per cycle. Secondly, the Q can be expressed as a fractional bandwidth of the cavity resonance,

$$Q = \frac{\lambda_0}{\Delta\lambda} = \frac{\omega_0}{\Delta\omega} \tag{6.5}$$

with λ_0 and ω_0 being the resonant wavelength or frequency, and $\Delta\lambda$ and $\Delta\omega$ being the full width at half maximum (FWHM) of the resonance peak. Both the ringdown and spectral methods of calculating Q will be used in this section, and we will see that they are both useful in different Q factor regimes. Calculating the Q factor from a spectrum using equation 6.5 is straightforward, with the FWHM and resonance wavelength or frequency able to be calculated easily; calculating Q from energy lost over time (as in equation 6.4) is less so, but we will now outline how.

The time domain signal of a cavity resonance, also called the 'ringdown' of a cavity, shown in figure 6.4a, is the decay in energy over time. The ringdown is given by

$$E(t) = U(t)e^{i\omega t}e^{-\alpha t}, \tag{6.6}$$

where $U(t)$ is the step function to 'ring up' or excite the cavity, indicated by the yellow boxes in figure 6.4, and α is the decay constant and the gradient of the logarithm of the decay envelope in the ringdown (with the logarithm of a decay shown in figure 6.4b) where $\alpha = 1/\tau$, with τ being the photon lifetime of the cavity. The decay envelope of the ringdown can be given by

$$E_{env}(t) = E_0 e^{-t/\tau} = E_0 e^{-\alpha t}, \tag{6.7}$$

where $E_{env}(t)$ is the field decaying in the cavity indicated by the purple boxes in figure 6.4, and E_0 is the field once the cavity has been excited or 'rung up', i.e., the source field.

$$|E(\omega)|^2 = \frac{|E_0|^2}{(\alpha^2 + (\omega - \omega_0)^2)} \tag{6.8}$$

$|E(\omega)|^2$ is at its maximum value of $1/\alpha^2$ when $\omega = \omega_0$, and at half this maximum when $\omega = \omega_0 \pm \alpha$. Therefore, the FWHM $\Delta\omega = 2\alpha$. Substituting this into the fractional bandwidth expression of Q,

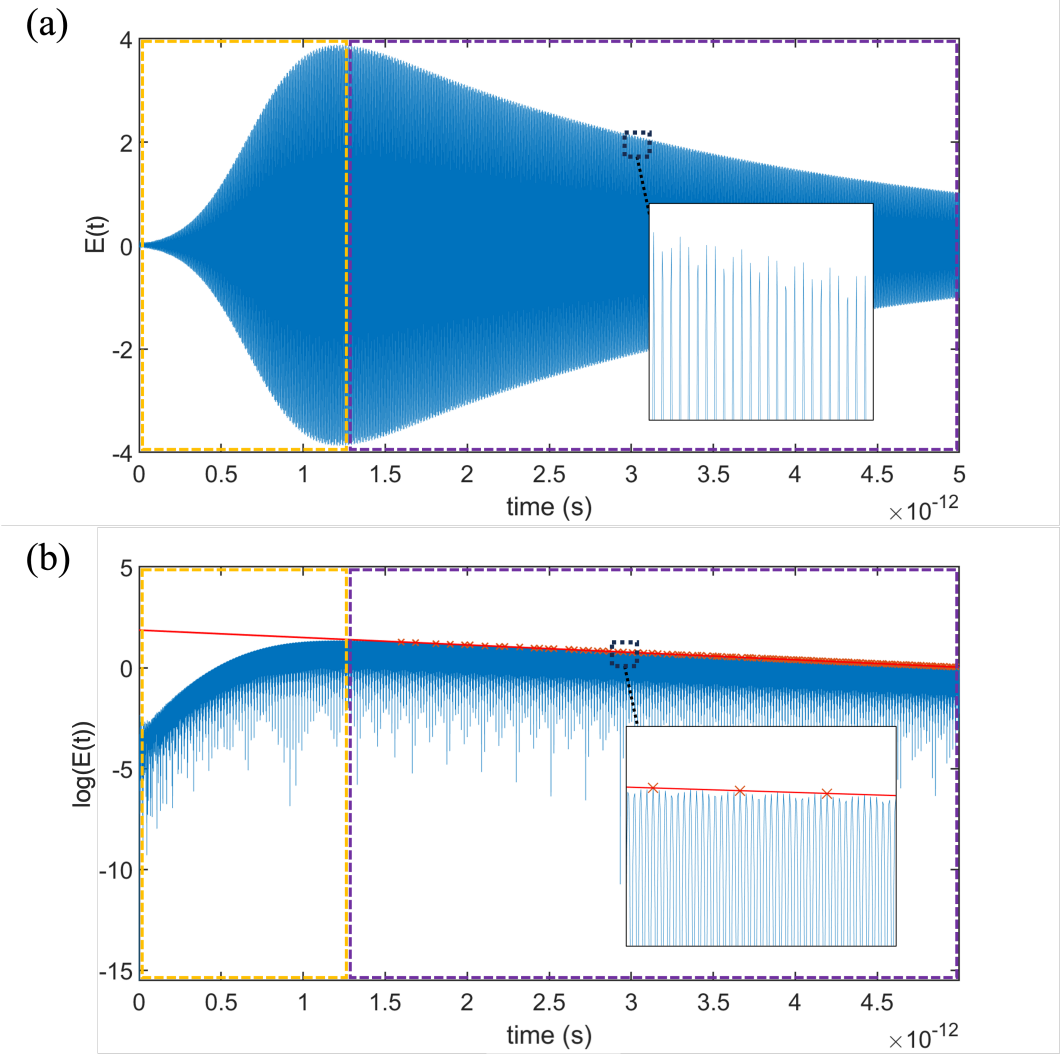

Figure 6.4: (a) FDTD-simulated ringdown $E(t)$, and (b) logarithm of plot (a), with yellow and purple boxes on both plots marking the cavity 'ring up'/excitation, and the ringdown/exponential decay, respectively. In (b), the gradient of the decay is plotted in red, and the data points used to calculate the gradient marked with red crosses. Both (a) and (b) have insets with zoomed-in views of the data, and are of a DBR cavity with $N = 50$ mirror periods either side of central quarter-wave spacer.

equation 6.5,

$$Q = \frac{\omega_0}{2\alpha}$$

and rearranging for α, we get

$$\alpha = \frac{\omega_0}{2Q}.$$

Substituting this into the equation for the time-varying field envelope (equation 6.7) we get

$$E_{env}(t) = E_0 e^{-\omega_0 t/2Q}.$$

Taking the natural logarithm and using the fact that $\ln(E_{env}(t)) = -\alpha t$:

$$\ln(E_{env}(t)) = -\frac{\omega_0 t}{2Q} = -\alpha t \tag{6.9}$$

and rearranging for Q, we once again get

$$Q = \frac{\omega_0}{2\alpha}$$

which can also be written as

$$Q = \frac{\omega_0 \tau}{2}[108]. \tag{6.10}$$

We are now able to calculate the Q factor using both the spectrum and the ringdown of a cavity.

To aid our discussions of cavity Qs, we define two different regimes of Q: a "high Q" regime, and a "low Q" regime. Here, we define a high Q cavity as one that we are not able to fully simulate the ringdown of with the simulation conditions that we have used, e.g., the simulation time of 5000 fs; we then define a low Q cavity therefore as one we are able to fully simulate the ringdown of. In our case, this boundary between low Q and high Q corresponds to a $Q \sim 400$. Depending on the length of the cavity, this results in a compute time between three and eleven hours. We acknowledge that this definition of high Q and low Q is not universal as the simulation time is chosen based on a compromise between accuracy of results and compute time, and other machines used to simulate devices will be different. However, these definitions will offer assistance when describing the results we will present.

6.2.3.2 Q vs Cavity Length

We will now use FDTD to simulate a range of triangular DBR cavities with varying lengths and calculate their Q factor. For our simulation setup, ten dipole sources were pseudo-randomly positioned

in the centre of the cavity to inject light into the cavity, with a wavelength $\lambda = 1543\,\text{nm}$. The sources had a pulselength of 500 fs and offset of 800 fs, with the properties of the sources a compromise between simulation time and spectral bandwidth of the sources. Although originally designed for a wavelength of 1550 nm, broadband simulations of the cavities revealed resonance at a wavelength of 1543 nm. This resonance is sufficiently close to 1550 nm for the purposes of this project of demonstrating triangular PCNCs in GaN. The cavities had varying numbers of mirror periods, with N being the number of mirror periods either side of the centre of the cavity (i.e. N = half of the total mirror periods of the PCNC). Results were measured from ten psuedo-randomly positioned monitors in the centre of the cavity, which record the electromagnetic fields as a function of position, time, and frequency/wavelength.

The Q factors for DBR cavities increasing in size from $N = 20$ to $N = 150$, in intervals of 10, are shown in figure 6.5. Q factors are shown calculated from both the cavity spectrum (figure 6.5a) and ringdown (figure 6.5b), including error bars for both. Q factors from the cavity spectra are calculated from the fractional bandwidth (equation 6.5), with the error in these Qs, δQ estimated with

$$\delta Q = Q\frac{\delta\Delta\lambda}{\Delta\lambda}, \tag{6.11}$$

where Q is the spectrally-calculated Q factor, $\Delta\lambda$ is the FWHM of the peak, and $\delta\Delta\lambda$ is the error in the FWHM, equal to 0.579 nm (half the spectral resolution). Qs are calculated from the ringdowns using the gradient of the logarithm of the ringdowns (equation 6.10), with the error in these Qs estimated using the standard error in the data used to calculate the gradient of the envelope of $\ln(E(t))$.

The spectral Q factors in figure 6.5a increase slowly and approximately linearly with N, with an approximate gradient of $40\,N^{-1}$ up until a maximum of $Q = 1630 \pm 1000$ at $N = 60$, after which Q saturates at around 1200; however, the large errors make it difficult to determine an exact relationship or precise values. On the other hand, the Q factors calculated using the ringdowns of the cavities show a clear saturation, saturating at $Q \approx 4100$ from $N = 90$ onwards. It is noted that after saturation, the Q factor appears to oscillate between a value of ~ 3900 and 4600. The Q factors calculated using the spectra and ringdowns are similar for low Qs, but quickly diverge.

We will now discuss the reason for the saturation of Q factor: the Q we have been discussing and calculating thus far is the net Q - the sum of the total Qs - there are different sources of loss within a cavity, each with their own Q factors and individual $1/Q$ decay rates, defined by subdividing the energy loss per cycle in equation 6.4 into two separate loss mechanisms, $E_{loss} = E_{lossw} + E_{lossr}$, where E_{loss} is the total loss out of the cavity, E_{lossw} is the loss from light decaying into the uniform

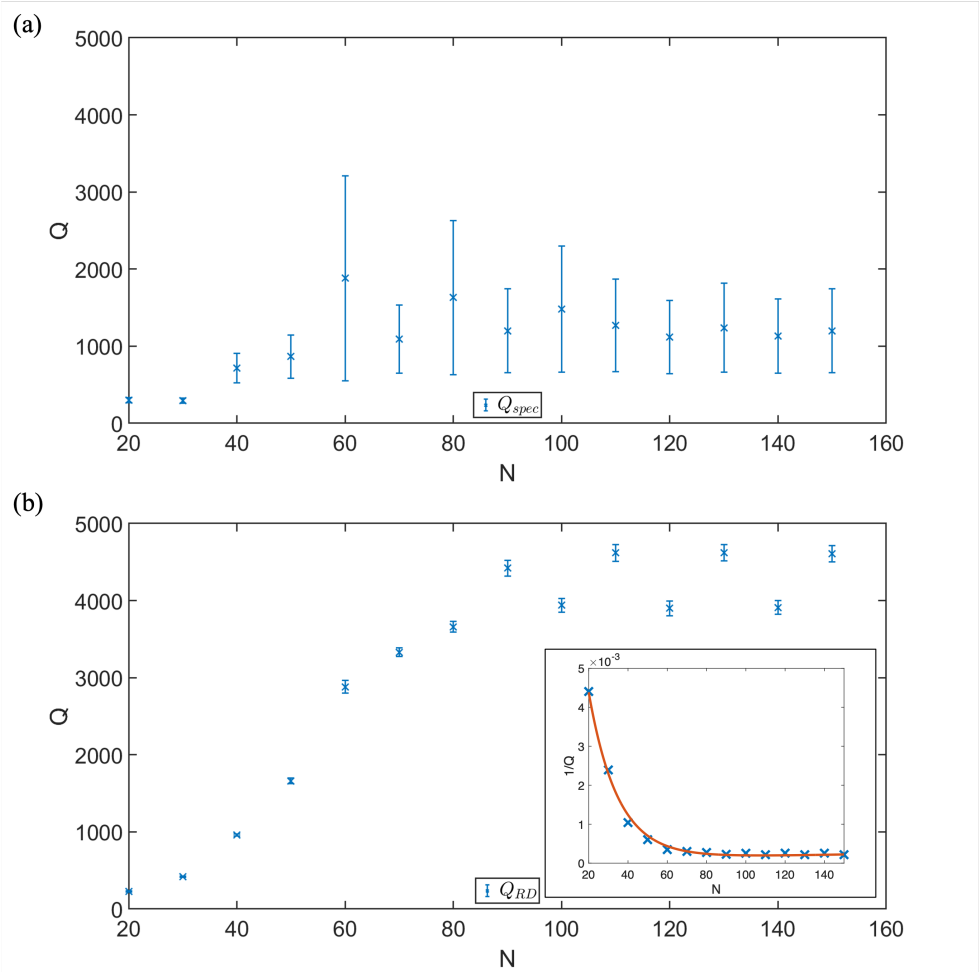

Figure 6.5: Q factor versus number of mirror segments N on either side of the cavity centre, with error bars. (a) Q calculated using spectrum. (b) Q calculated using ringdown. Inset in (b) shows $1/Q$ vs N. Cavities simulated using the FDTD method.

nanobeam either side of the cavity, and E_{loss_r} is the loss from light radiating out from the cavity into the air, i.e., radiative loss [108].

The total Q of our cavities is therefore

$$\frac{1}{Q} = \frac{1}{Q_w} + \frac{1}{Q_r}, \tag{6.12}$$

where $1/Q$ is the total decay rate, $1/Q_w$ is the decay rate of light into the uniform nanobeam waveguide (either side of the DBRs), and $1/Q_r$ is the decay rate from light radiating into the surrounding air, or the radiative loss. Q_r is roughly independent of N, and Q_w increases exponentially with N [108]. This means that as $N \to \infty$, $1/Q_w \to 0$, and $Q \to Q_r$, resulting in $1/Q$ decreasing exponentially, which is observed in the inset of figure 6.5b, and Q saturating at $\sim Q_r$, ~ 4000.

In terms of physical devices, these results mean that there is an upper limit to the cavity size one can fabricate before diminishing returns in Q are reached. As the losses from fabrication imperfections, e.g. surface roughness and variation in mirror dimensions, are proportional to the cavity length, fabricating a longer device could actually decrease Q beyond this saturation point. In order to minimise device footprint while maximising Q, we therefore recommend performing similar calculations to those in this section, to determine the saturation point for your PCNC design before fabricating a device to be used in a PIC.

6.2.3.3 Comparing the Spectral and Ringdown Q Calculation Methods

We will now examine the spectra and ringdowns to determine the sources of these large errors, and compare and contrast the ringdown and spectral methods of calculating Q. Figure 6.6 shows representative ringdowns and spectra of the cavities simulated. Figure 6.6a, b & c show ringdowns, and figure 6.6d, e & f show spectra of cavities for $N = 20, 50$ and 140, respectively. As just seen in figure 6.5, the Qs calculated from the spectra have significantly (~ 5 times) larger errors than the Qs calculated from the ringdowns. The reason for the large errors is because the error in spectrally calculated Q, δQ, has a second order dependence with the value of Q; both Q and δQ, equations 6.5 and 6.11, are inversely proportional to the FWHM $\Delta\lambda$: $\delta Q = Q\frac{\lambda_0}{\Delta\lambda} = \frac{\lambda_0}{\Delta\lambda} \cdot \frac{\delta\Delta\lambda}{\Delta\lambda} = \frac{\lambda_0\delta\Delta\lambda}{\Delta\lambda^2}, \propto \frac{1}{\Delta\lambda^2}$. In practical terms: as Q increases, the FWHM gets narrower and the error in FWHM therefore increases, increasing the error in Q; this is then compounded by the propagated error being proportional to the value of Q.

As seen in figure 6.6d, e, f, the width of the spectral peak decreases with an increasing Q, as expected. However, at a certain point the linewidth reaches a similar magnitude to the spectral

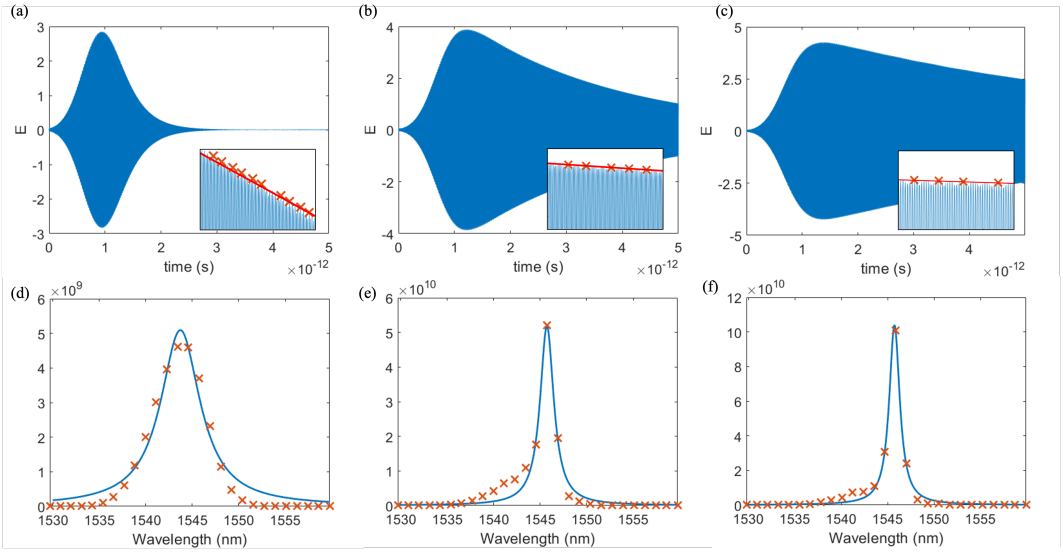

Figure 6.6: Ringdowns (a, b, c) and spectra (d, e, f) of DBR cavities with 20, 50 and 140 mirror segments, respectively, on either side of the cavity centre, calculated using the FDTD method. Spectra have Lorentzian functions fitted (blue), used for calculating Q.

resolution, and the linewidth is too narrow and no longer able to be resolved. As the spectral resolution is of a similar magnitude to the linewidth, this leads to large errors in calculated Q, seen in figure 6.5a. As the simulation is no longer able to resolve the spectra, this means that the Q calculated here using the spectra are not the actual Qs of the devices, and are resolution-limited. As such, the results in figure 6.5a are not a valid representation of the Q factors of these cavities. As opposed to the results in figure 6.5b from the ringdowns, which are.

For low Qs, the results from the spectra and ringdowns are relatively similar. However, as stated at higher Qs the spectral method breaks down, and cannot resolve Qs much higher than this. This is in contrast to the ringdown method, which is able to reliably resolve arbitrarily high Qs. The error in Q at low Qs is relatively similar for both the spectra and ringdown results, and the errors increase in magnitude relatively similarly with increasing Q, but the errors in the spectral Qs are still $5 - 15$ times larger than those from the ringdowns. The maximum error in Q from the spectra is ± 1880 for $N = 60$, and the maximum error in Q from the ringdowns is ± 109 for $N = 110$.

In order to more accurately calculate Q factor from a spectrum, a much smaller spectral resolution is required. The large error in Q calculated spectrally is a result of the poor spectral resolution of the simulation, with spectral resolution inversely proportional to simulation time. This resolution is not able to be greatly increased, as this would lead to prohibitively long simulations, with the cavity

simulations discussed here taking approximately six hours for the time we have simulated (5000 fs). In order to increase the spectral resolution to bring the error in Q to a comparable level to that from the ringdown, the simulation time would need to be approximately five times as long. For a full set of cavity simulations such as here, that could result in many further weeks of simulation time. As a further example and demonstration of the limitations of the Q calculated from a simulated spectrum, in order to calculate the Q/resolve the FWHM of a cavity with $Q \sim 10^6$ with the same accuracy as our results here (which have not-insignificant errors), the simulation would need a spectral resolution of $\sim 1.543 \times 10^{-3}$ nm, which would require the simulation time to be ~ 750 times as long, $\sim$ half a year. As such, the ringdown method of measuring Q is a much more efficient method of measuring Q factor, especially as Q increases and an even greater degree of spectral resolution is required due to the decreasing FWHM.

As a result of our analysis, when simulating an optical cavity we strongly recommend using the ringdown to calculate its Q factor, and would not recommend using the spectrum due to the high simulation and compute time required to accurately calculate a high Q. We believe the ringdown method is a more practical technique for calculating the Q factor of a simulated cavity, with a much shorter simulation time needed for precise results.

6.2.3.4 Simulating the Effect of Loss on Q

Fabricated integrated photonic devices are not perfect, they have random disorder - imperfections and irregularities in their physical structure caused by manufacturing processes, causing optical loss and hampering device performance. On the nanoscale, these imperfections are unpredictable, and are virtually impossible to simulate in FDTD directly as they would require $\sim$nm resolution in 3D, resulting in impractically long simulation times. For example, a resolution of 2 nm would be an increase in resolution of ~ 20 times, which, as simulation time scales with dx^4, results in a simulation time 10^4 times as long. With the average simulation time of our cavities being $\sim$ four hours, this would increase the simulation time to ~ 4.5 years. Or, as another example, to decrease the resolution further to 1 nm, a simulation time of ~ 73 years would result. However, we present a model for simulating loss in a PCNC by introducing a material loss via the imaginary refractive index of the material.

To illustrate, start with a plane wave travelling along the $x-$direction,

$$E = E_0 e^{i(k.x - \omega t)},$$

which describes the propagation of light in a medium, where wavenumber $k = \frac{\omega n}{c}$, and refractive index $n = n_r + in_i$, where n_r and n_i are the real and imaginary components of the refractive index, describing propagation speed (relative to in a vacuum) and attenuation, respectively. This attenuation can be used as an added decay mechanism in an otherwise perfect cavity structure (perfect in terms of no losses from imperfections in fabrication) to model how loss affects a cavity. Although we only study one source of loss, material absorption, there are many others, such as surface roughness of the top of the nanobeam and the sides, deviations in width and thickness between each mirror segment, and deviations in etch angle.

To investigate loss in a cavity, we use FDTD to simulate triangular DBR PCNCs with $N = 90$ mirror periods, with increasing imaginary index n_i. This cavity size was chosen as having a balance between simulation time and a high Q factor of 4420. Figure 6.7a shows the Q factor of the cavity and its dependency on n_i. Q is calculated from the cavity ringdown, and the figures 6.7 also show error values for Q factor, estimated using the same standard error as before. Q is seen to decrease exponentially with increasing n_i, with the fit in figure 6.7a being an exponential. Figure 6.7a appears to show $Q \to 0$ as $n_i \to \infty$, which is verified by plotting Q against $1/n_i$ in figure 6.7b. The inset of figure 6.7a shows the decay rate $1/Q$ as a function of n_i, with $1/Q$ linearly increasing with n_i. The gradient in the inset of figure 6.7a indicates the rate at which energy decays in the cavity as a function of imaginary index n_i, with a value of 0.62, and the intercept represents the loss in a cavity with no material absorption, $1/Q_{design}$, which is equal to 2.26×10^{-4}. Figure 6.8 also shows example spectra and ringdowns for cavities with increasing n_i, further demonstrating the decrease in photon lifetime and Q with n_i.

To analyse these results further and help contextualise them, we again express the total cavity Q factor as the sum of component decay mechanisms and Qs. In this case, we express Q as

$$\frac{1}{Q} = \frac{1}{Q_{design}} + \frac{1}{Q_{loss}} \tag{6.13}$$

where $1/Q_{design}$ is intrinsic decay rate of the cavity (which we have been calculating thus far, and is 4420 for a cavity of this N value), and $1/Q_{loss}$ is the decay rate due to the imaginary refractive index n_i. Increasing n_i increases the associated decay $1/Q_{loss}$, with $1/Q_{design}$ remaining constant.

To contextualise our results, we discuss them in relation to Ref. [109], which estimated the contributions of different physical device imperfections (which they call $Q_{imperfect}$) on the overall Q factor of a fabricated silicon 2D photonic crystal cavity, compared to a simulated cavity of the same de-

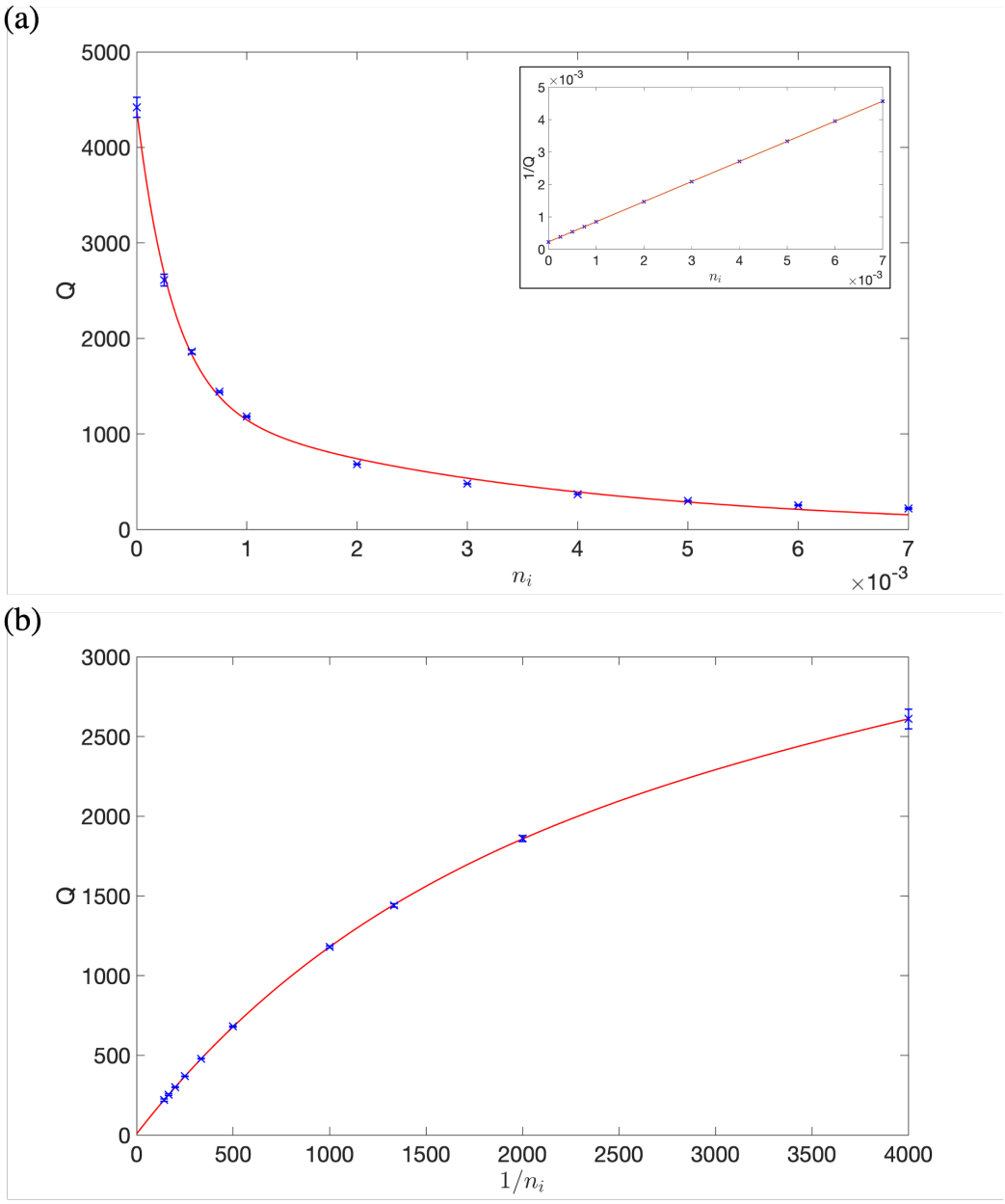

Figure 6.7: (a) Q factor against imaginary refractive index n_i for triangular DBR cavity, with error bars. DBR cavities have 90 mirror segments on both sides. Inset shows $1/Q$ against n_i. (b) Q against $1/n_i$, confirming that Q does go to zero for large values of n_i. Note that $Q = 4420$ at $n_i = 0$ is not plotted due to the division by 0

.

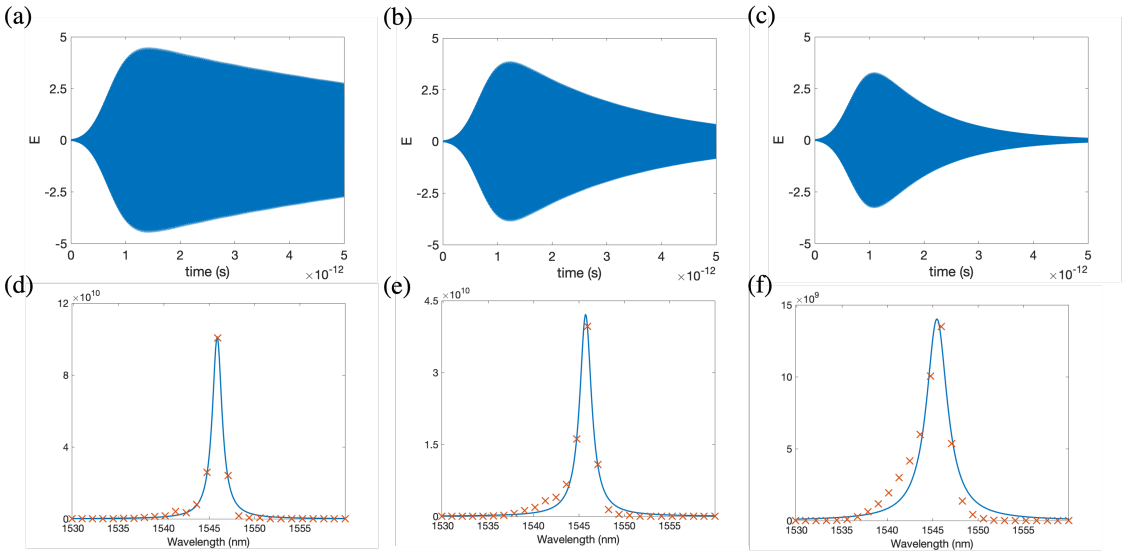

Figure 6.8: (a, b, c) Ringdowns and (d, e, f) spectra of PCNC DBRs with varying imaginary refractive indices of 0, 7.5×10^{-4} and 2×10^{-3}, respectively, demonstrating the decrease in Q factor with increasing material absorption.

sign. Their estimations were in good agreement with their experimentally measured Q, Q_{exp}. To the best of our knowledge, no such investigation exists for a PCNC. Ref. [109] simulated ultra-high $Q > 15,000,000$ cavities and fabricated them, with a maximum experimental Q in the fabricated devices of $1,000,000$, showing that $Q_{exp} \approx Q_{imperfect}$ (which they estimated to be $\approx 900,000$), and showing a significant decrease in Q compared to the designed and simulated device. This behaviour could be partially explained by our results, which show an exponentially decaying Q with a linearly increasing loss. Ref. [109] also calculated that the decrease in Q resulting from material absorption is two orders of magnitude smaller than from the largest contributors: the surface roughness of the inner walls, variation in radii of air holes, and tilt of inner walls of air holes. This suggests that material absorption will not be the largest contributor to a decreased Q in a fabricated triangular PCNC, and further work is needed to quantitatively relate these results in n_i to losses in a fabricated device, which we will discuss in our section on future work in the conclusion of this thesis.

In summary, changing the imaginary index n_i of the cavity is a simple method of changing the degree to which light is lost in a PCNC by introducing a new decay mechanism, $1/Q_{loss}$, and offers a convenient description of simulating loss from a cavity which may occur from a variety of sources such as imperfections in the cavity shape from fabrication, or from material imperfections, which would be otherwise difficult to simulate.

6.3 Apodised PCNCs

The triangular cross-section DBR PCNCs we have described thus far have had reasonably high Q factors of up to ~ 4000. Whilst Qs of this size are still useful [104], these Qs are not in the high Q regime of 10^4 and above which have been demonstrated elsewhere in the literature [102], [104], [107], [110]. If we are to attempt to obtain Qs in this ultra-high regime with width-modulated triangular GaN PCNCs, the design must be adjusted.

Apodisation of the cavity mode is a technique of increasing Q by designing a mirror strength (γ) profile which increases linearly from the centre of the cavity. Such a γ profile results in a gradual change in the envelope of the cavity mode profile, leading to smaller components of the spatial Fourier transform spectrum in the leaky region [111]. A Gaussian mode profile along the PCNC has been shown to decrease loss [111], with Ref. [112] demonstrating that the energy within the light cone (i.e. radiative loss $1/Q_r$) was approximately two orders of magnitude smaller in a PCNC with a Gaussian attenuation profile compared to an exponential. However, the mode profile need not be Gaussian, it may be a Lorentzian for example [113], but the profile does need to be varied gently. Ref. [112] and [107] by the same author outline a deterministic approach to designing a high-Q apodised cavity, which we follow. They describe an approximately linearly increasing γ resulting in a Gaussian mode profile, with this gradually increasing γ profile being the most important aspect to increasing Q. They also note that having a spacer layer with length $L = 0$ minimises mode volume and cavity loss, however as we are using apodisation to improve the PCNCs cavity designs we already have (described), which have a half-wavelength spacer layer, we omit this step, and focus on a gradually increasing γ profile.

To design a linearly increasing γ profile, we use the mirror strengths as a function of filling fraction FF, calculated in figure 6.3. The FF profile used could be from the left side of the peak in figure 6.3, i.e., an increasing FF, or from the right side of the peak with a decreasing FF, or a combination of both, so long as the mirror strength increases linearly. For our apodised cavity design, we select the left side of the peak and an increasing FF profile. The overall periodicity ($a_1 + a_2$) of these cavities has remained the same as the previous DBR PCNCs, at a value of 578 nm. Figure 6.9a shows the mirror strength profile and figure 6.9b shows the filling fraction profile along the length of this cavity. A PCNC of this design should have minimal scattering losses between each mirror segment, leading to a high Q.

However, we find that there appears to be no resonance within the cavity, with the cavity spectra and $E(t)$ being approximately equal to those of the source pulse. A wide range of apodised cavities

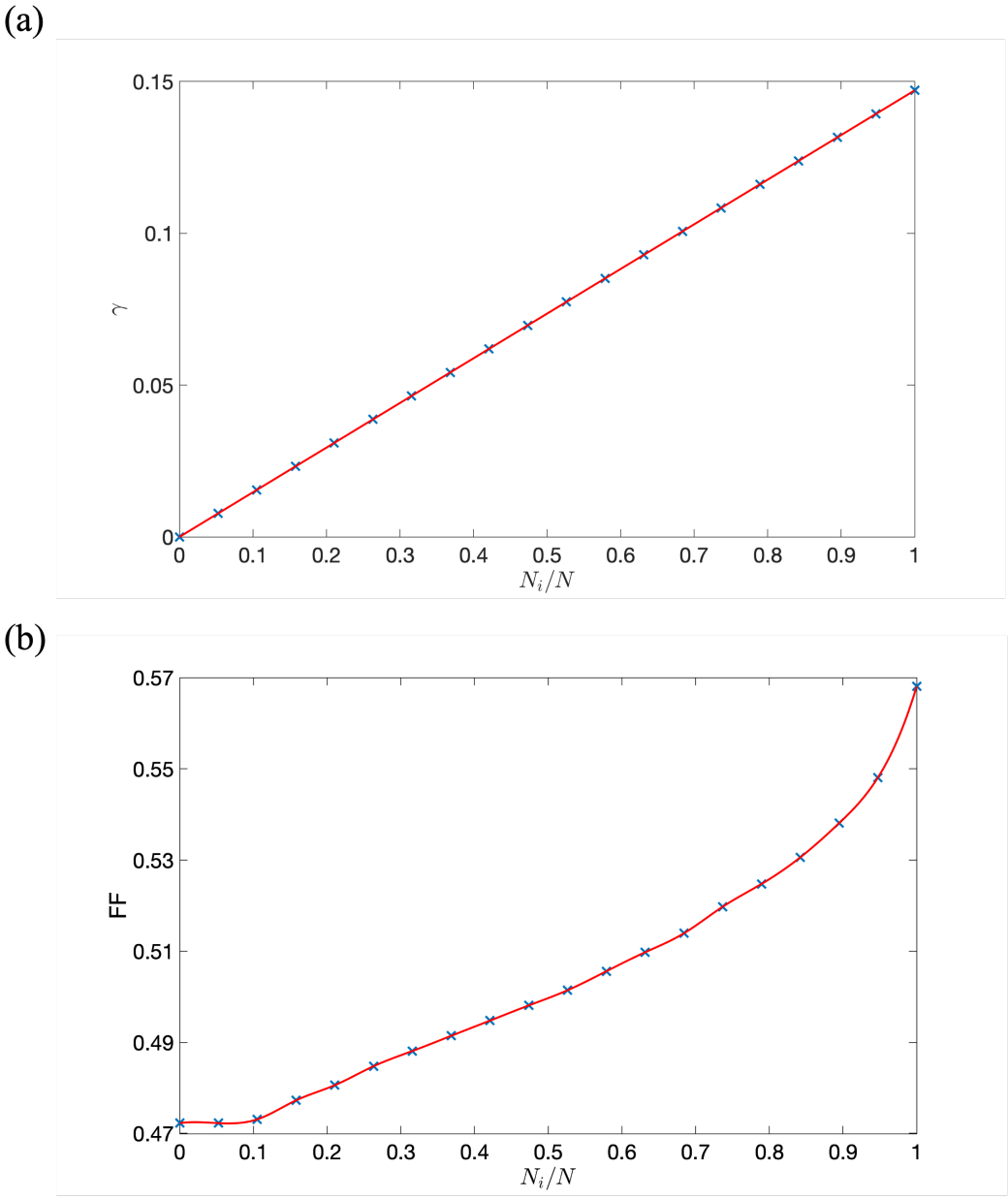

Figure 6.9: (a) Mirror strength γ and (b) filling fraction (FF) profiles as a function of mirror segment position, calculated as a ratio of mirror segment index N_i to total number of mirror segments N.

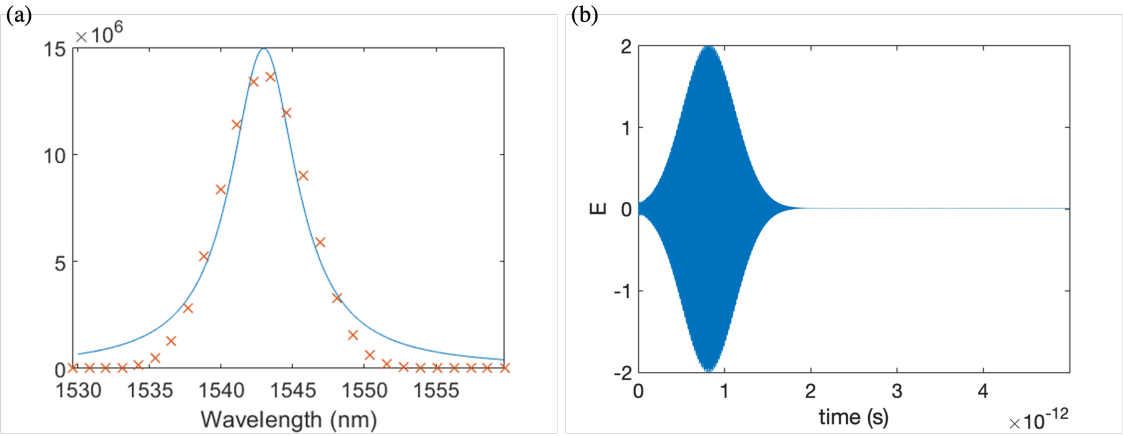

Figure 6.10: Example (a) spectrum and (b) $E(t)$ of an apodised ($N = 20$ mirror periods) cavity, which does not appear to be resonating.

were simulated, with the number of periods N in the cavities ranging from $N = 20$ to $N = 150$, in steps of 10. The spectra and $E(t)$ were found to be independent of N for all values considered, with an example shown in figure 6.10. Given that other work in the literature [102], [107], [112] has shown different results to ours presented here and have demonstrated high Qs using a linearly increasing mirror strength profile, we believe that the design we have used here must be incomplete or incorrect, and is subject to further work. There is a clear discrepancy between our results and others, which despite our best efforts of following the outlined design procedure, we were unable to replicate. As we have followed the design procedure of calculating the mirror strength of DBR mirrors of different FFs, and creating a linear mirror strength profile from these results, it is not clear where we have gone wrong. We recognise that Ref. [112] and [107] have used a different form of mirror, electing to use circular etch holes instead of modulations in nanobeam width, as we have. However, this difference should be a matter of personal choice, and shouldn't impact the ability to resonate with an apodised version of these mirror types; in fact, width-modulated nanobeams are clearly able to resonate at this wavelength, as we have already demonstrated DBR cavities with a fixed γ profile which do resonate.

6.3.1 Central Spacer Length

The other way our design is different to the described design procedure in Ref. [112] and [107] is that we have a central half-wavelength cavity spacer layer, which they do not. While they do state that the length of this spacer layer does effect Q, it should not effect the resonance of the cavity to this degree. However, with an aim to determine whether this may be the case, we study the effect the length L

of a central cavity spacer has on this cavity design. We introduced another section of nanobeam of thickness 765 nm in the centre of the nanobeam, and varied its length between 0 and 600 nm, in steps of 5 nm. We found varying L in this way had no effect on the lifetime of the cavity, and no resonance was observed, with the spectra and $E(t)$ of the cavities again resembling the sources (shown in figure 6.10), and being independent of L.

We therefore draw the conclusion that the central cavity region is not the source of the lack of resonance of our cavity design, and is therefore likely due to the γ profile we have chosen. However, as we have used a linearly (i.e., gradually) increasing γ as prescribed, more work is needed to determine the source of lack of resonance. We outline potential avenues of investigation in our suggestions for future work section, §7.2.

6.4 Very-High Q Cavity

We now evaluate the photon lifetime, the spectral and ringdown techniques for calculating Q factor, as well as evaluating the effect of loss on Q, for a very-high Q ($\sim 100,000$) cavity. As our attempt at apodisation to increase Q was unsuccessful, these results were produced using a PCNC designed by a collaborator [114].

Figure 6.11 shows the (a) spectrum and (b) ringdown of such a very-high Q cavity, simulated for the same length of time as the previous cavities using the FDTD method. The Q calculated using the spectrum is 781 ± 233, and using the ringdown is 106000 ± 6830. This result further demonstrates the limitations of calculating Q using spectra for the FDTD method, and the usability of the ringdown method; although the photon lifetime of this cavity is clearly very high, the spectral resolution is not able to resolve the assumedly very narrow resonance peak (a cavity with a Q factor of 10^5 and resonating at 1561 nm as here, would have a FWHM of 0.01561 nm, whereas the FWHM of the spectrum in figure 6.11 a is 1.4 nm).

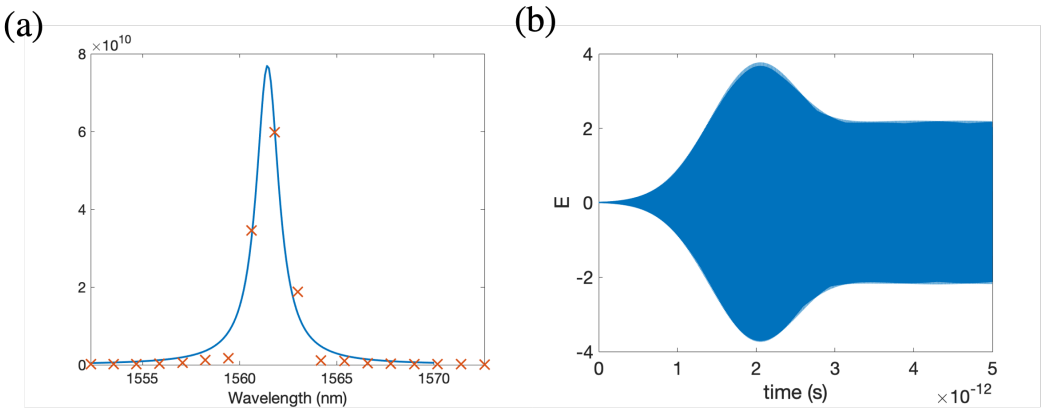

Figure 6.11: (a) Spectrum and (b) ringdown of an apodised PCNC DBR cavity designed by [114], with a fixed period and the apodisation profile defined based on the nanobeam width in each mirror segment, with mirror strength linearly increasing from the centre of the cavity, and with no central half-wavelength spacer layer.

6.4.1 Differences in Design

This PCNC design differs from ours in that mirror strength is varied, and apodisation relationship defined, based on the width of the nanobeam, and not the relative period of each mirror segment (FF); our design directly changes the phase of the light, whereas this design indirectly changes the phase using the effective index. This PCNC consists of 30 apodised mirror sections either side, and 50 'padding' sections of high γ DBR mirrors to minimise loss into the adjacent feeding waveguide, $1/Q_w$, and increase overall Q. This PCNC design is similar in that it consists of alternating width-modulated layers of GaN, also with a wider nanobeam width of 765 nm, and a narrow nanobeam width of 600 nm. This cavity was also designed for a wavelength of 1550 nm. This PCNC also differs in the fact that the central cavity spacer is 765 nm wide, as opposed to 600 nm in ours. The overall periodicity a of the mirrors is also different, at 510 nm, as opposed to our 578 nm. Their overall periodicity of $a = 510$ nm was calculated with the relationship

$$na = \frac{\lambda}{2},$$

and using the index of the wide nanobeam $n = 1.52$, whereas we calculated the optical path lengths using both optical path lengths in the mirror segments.

6.4.2 Simulating the Effect of Loss in a Very-High Q Cavity

We now apply the same technique of evaluating the effect of loss on cavity Q factor as in §6.2.3.4, using the simulated complex index, but this time in a very-high Q cavity ($Q \sim 100,000$). Figure 6.12a shows the Q factor of the cavity as a function of imaginary index n_i, and figure 6.12b shows the Q factor as a function of $1/n_i$. As n_i increases, Q decreases approximately exponentially, similarly to the lower Q cavities. The inset in figure 6.12a shows the overall loss rate $1/Q$, which increases linearly with n_i. The intercept of this relationship is $1/Q_{design}, \sim 10^{-5}$, and the gradient, the rate at which the loss increases as a function of n_i, is equal to 0.98. Figure 6.12b shows the Q factor as a function of $1/n_i$, verifying that Q also $\to 0$ as $n_i \to \infty$ for this cavity, as before in figure 6.7 in the cavity with a lower Q. Figure 6.13 also shows example ringdowns and spectra for varying n_i values, further demonstrating the decrease in photon lifetime and Q with n_i.

We have now applied our analysis of the effect of loss on a PCNC to a cavity with a high Q, verifying that the Q of a high Q cavity does decrease exponentially with an increasing imaginary index n_i, and tends to 0 as $n_i \to \infty$. As before in §6.2.3.4, as material absorption will likely not be the largest contributor to a decreased Q in a fabricated triangular PCNC [109], further work is needed to quantitatively relate these results in n_i to losses in a fabricated device, which we will discuss in our section on future work in the conclusion of this thesis.

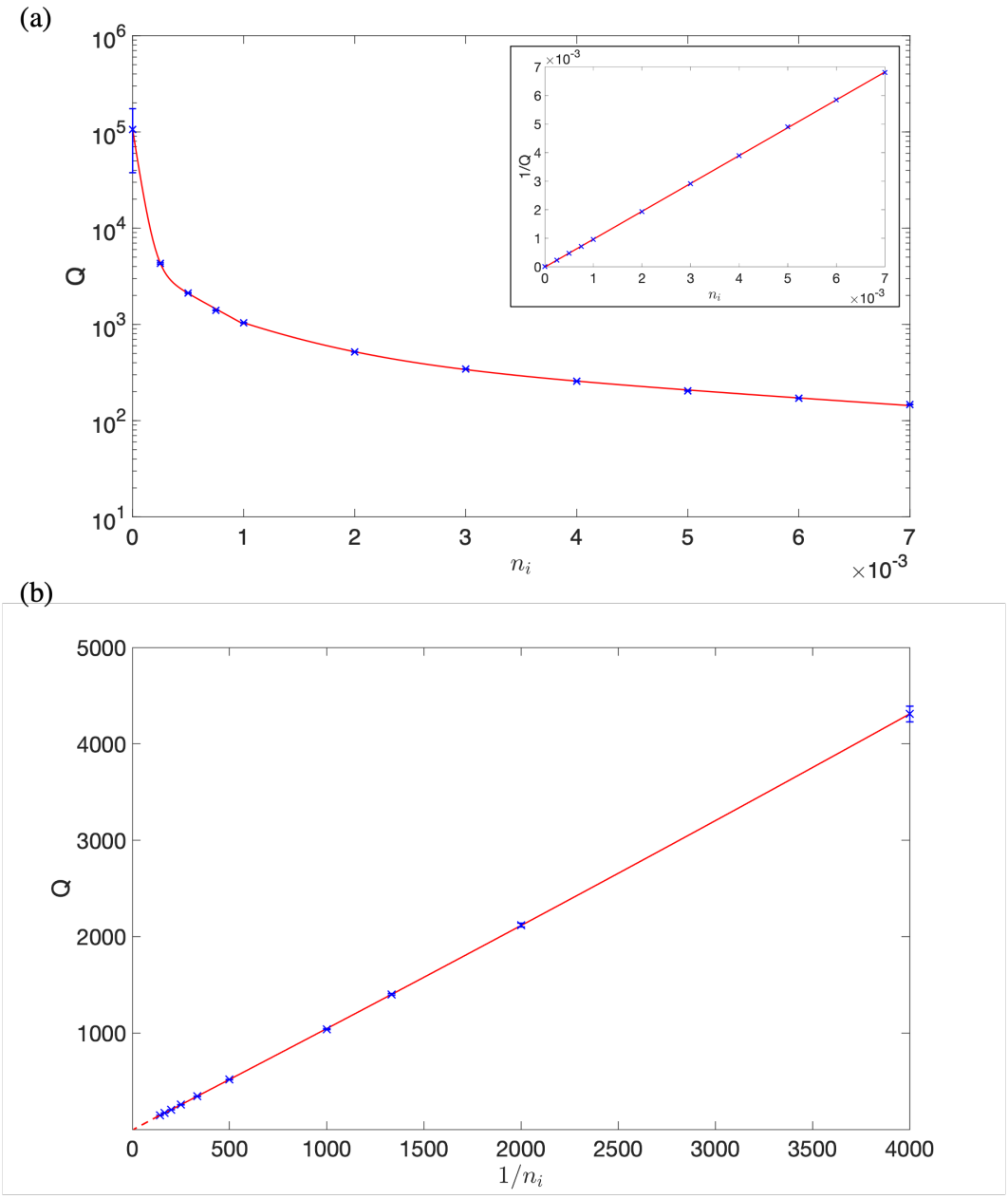

Figure 6.12: (a) Q factor as a function of imaginary refractive index n_i. (b) Q factor as a function of $1/n_i$. Red dashed line extrapolates to $Q = 0$.

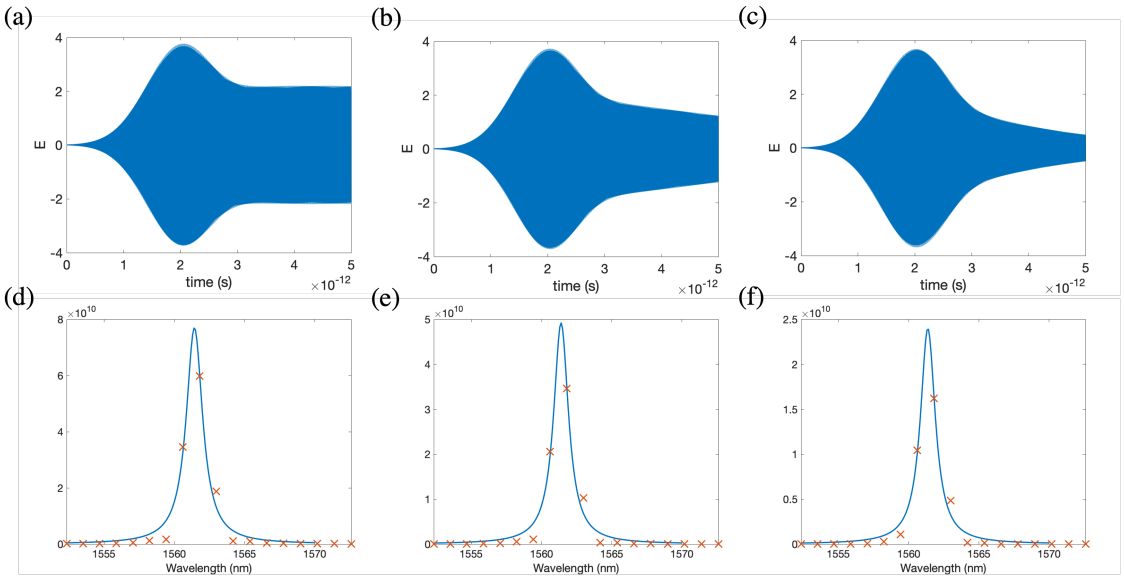

Figure 6.13: (a, b, c) Ringdowns and (d, e, f) spectra of apodised PCNC DBRs with varying imaginary refractive indices of 0, 7.5^{-4} and 2×10^{-3}, respectively, demonstrating the decrease in Q factor with increasing material absorption.

6.5 Summary

We have used FDTD simulations to show how triangular cross-section nanobeams can be used for width-modulated optical cavities using a distributed Bragg reflector (DBR) design, compatible for fabrication using angled etching techniques. The mirror strength γ of a DBR mirror for specific filling fractions (FFs) has been calculated, and has allowed us to optimise our DBR designs for the maximum mirror strength. Using these optimised DBR cavity designs, we have presented two methods of calculating the Q factor of a cavity, spectrally and using the ringdown, comparing and contrasting these two techniques and finding that the ringdown method to be significantly more practical in the context of simulations, with much higher precision and accuracy compared to calculating Q using spectra for the same simulation time. We used these two calculation methods to calculate the Q factor of DBR cavities with varying length, and observed the saturation of Q factor with cavity length. We have presented a method of analysing loss in a PCNC by varying the simulated imaginary index n_i of the cavity, applying this method to our designed DBR cavities and to higher Q apodised cavities from a collaborator. We have found that overall Q factor exponentially decays with increasing n_i, tending towards 0, and have analysed the decay rate $1/Q$ resulting from the imaginary index, and found it to be linearly dependent on n_i. We attempted to apodise our triangular DBRs with a linearly increasing

FF-dependent γ profile, but were ultimately unable to achieve resonance. Overall, to the best of our knowledge, we have presented the first study of triangular cross-section GaN PCNCs, and the first analysis of the effects of imaginary index on Q factor.

Chapter 7

Conclusion

7.1 Summary

In this thesis, we have investigated and studied the compound semiconductor gallium nitride (GaN) for use in integrated photonics at a wavelength of 1550 nm. We have presented relevant theoretical background related to our research, and provided relevant literature to contextualise our work.

In chapter 4, we simulated and fabricated GaN on sapphire ridge waveguides. We used eigenmode calculations to investigate the effects that waveguide dimensions have on the effective index of the waveguide mode, identifying minimum device geometries required for optical confinement, and the boundaries for a waveguide to become multimode. Although such calculations are perhaps commonplace, they are not available for GaN on sapphire. To the best of our knowledge, we have presented the first in-depth study of the mode index properties of GaN on sapphire ridge waveguides. Commercially available 500 nm thick GaN on sapphire was found to have a wide range of widths in this single-mode regime. Following these simulation-driven designs, GaN on sapphire waveguides were fabricated from 500 nm thick of GaN on a sapphire substrate using a methodology which we have developed, using conventional fabrication techniques. Nickel was found to be an appropriate etch mask for GaN using a lift-off process, with a measured upper bound selectivity of 23. The nickel lift-off process was a key step in the success of fabricating waveguides. Starting with a recipe for etching 2000 nm of GaN, we found greater process control by using a thinner layer of nickel, going from 150 nm to 30 nm. Using thinner nickel improved the device yield from $\sim 20\%$ to $\sim 100\%$. Although the nickel lift-off process had a high yield, the design transferred to the hard mask had a width greater than the designed

devices, and waveguide widths should be adjusted by approximately 350 nm to lithographically tune the dimensions.

In chapter 5, we presented simulation results investigating the capability of GaN triangular cross-section nanobeams as waveguides, with the eigenmodes of these triangular nanobeams calculated using FDE simulation. These triangular nanobeams were suspended in air, and featured high optical confinement as a result of the air cladding. Equilateral triangular nanobeam waveguides were simulated with a range of widths, and a width $w \geq 400\,\text{nm}$ was needed for modes to be supported in the waveguide. We found that increasing the size of the nanobeams allowed the modes to be better confined to the waveguide region, with the effective index n_{eff} increasing with an increased waveguide width. We calculated the approximate zero dispersion point of GaN equilateral triangular nanobeam waveguides at 1550 nm to be 765 nm. For all equilateral waveguide widths considered, the fundamental transverse-electric (TE) and transverse-magnetic (TM) modes were degenerate in n_{eff}. We investigated the condition for this degeneracy, and have determined that an equilateral triangle cross-section is required, with the waveguide becoming birefringent when the cross-section is no longer equilateral, e.g. is isosceles or scalene. In investigating this, we have also presented the mode characteristics of triangular nanobeam waveguides with a range of different etch angles and asymmetry. To the best of our knowledge, this thesis is the first work to describe the degeneracy of TE and TM modes in triangular nanobeam waveguides. Our waveguide simulations also offered insights into assessing the fidelity of the operation of a fabricated device compared to a designed device, providing information on how quickly the effective index changes with deviations away from an equilateral waveguide, in terms of changing etch angle and asymmetry. The effect an angled substrate has on a waveguide mode was also simulated, with a small separation ($\sim 50\,\text{nm}$) being required for a triangular waveguide to be able to support an optical mode, for our waveguide design.

In chapter 6, we described 3D FDTD simulations of width-modulated triangular GaN nanobeam cavities. We outlined a PCNC design which used width-modulated DBR mirrors either side of a central half-wavelength spacer layer, with mirrors designed to satisfy the Bragg condition. To validate our design and verify our design satisfied the Bragg condition, we calculated the mirror strength γ as a function of mirror filling fraction (FF), using the decay envelope of the light in these mirrors. This result then allowed us to tweak our design to ensure the Bragg condition and maximum mirror strength was achieved. With this verified DBR PCNC design, we simulated a range of cavities with varying numbers of mirror segments N either side of the central cavity spacer, i.e. different lengths

of cavities. We evaluated two methods of calculating the Q factor of these cavities: using the spectra of the cavities and the ringdowns of the cavities. We determined that as a result of the spectral resolution of the simulation being of at least a similar magnitude of the spectral FWHM, the spectral method was not able to accurately calculate Q for any cavities other than those with a low Q ($\gtrapprox 400$). This is in contrast to the ringdown method, which we observed to be able to resolve large Qs, with small estimated errors. We calculated that to be able to calculate the Q of a $Q \sim 4000$ cavity using the spectrum with a similar degree of accuracy to the ringdown method, a simulation time of half a year, which is prohibitively long. Using the ringdown method, we observed that the Q factor of our triangular cross-section GaN DBR PCNCs saturates with N, at around $N \sim 90$, $Q \sim 4000$. This saturation behaviour is in agreement with the literature, and is explained by describing the overall Q factor in the cavity as the result of the two associated Q factors and loss mechanisms: the Q into the nanobeam waveguide out of the cavity, $Q_w g$, which increases exponentially with N, and Q_r, the Q from light radiating out of the nanobeam, which is approximately independent of N - leading to an overall Q which saturates at $\sim Q_r, \sim 4000$. We attempted to increase the Q factor of these cavities beyond the saturation point by employing the method of apodisation in which a gradually increasing γ profile results in lower losses and a higher Q, however our design failed and did not resonate. In order to identify the source of the issue, we compared our design to literature and investigated whether changing the central cavity length L would fix the issue. However, we found no change in the cavity for $0 \leq \text{nm}\, L \leq 600\,\text{nm}$. We therefore concluded there must be a fault with the γ profile, and outline suggestions for future work in the coming section on future work. We investigated the effects of optical loss on the Q factor of a PCNC, using the imaginary refractive index n_i of the device material as an analogy for directly simulating loss due to random imperfections in a device, which would be practically impossible to achieve due to the simulation resources required. We found that Q factor decreases exponentially with n_i. To the best of our knowledge, we have presented the first study of triangular cross-section GaN PCNCs, and the first analysis of the effects of imaginary index on Q factor.

7.2 Future Work

The simulations in this thesis were only for one wavelength, 1550 nm. However, a study of the behaviour of optical modes in GaN waveguides at multiple different wavelengths could be undertaken to further develop the understanding of GaN integrated photonics. Both ridge and triangular nanobeam

waveguides could be simulated at different wavelengths, with the mode properties and the boundaries of widths and thicknesses at which higher order modes are supported being of interest.

In chapter 4, we have started the process of taking the commercially relevant material of GaN on sapphire and turning it into usable devices. However, we believe GaN on sapphire waveguides and PICs should be investigated further. GaN on sapphire PCNCs could be simulated and manufactured using our eigenmode results to choose suitable waveguide dimensions, and compared to the triangular PCNCs we have simulated in this thesis; these PCNCs could have mirrors defined by etch holes, or by modulation in nanobeam width as we have presented. As GaN is non-toxic and bio-compatible [115], these PCNCs could be used for biomedical sensors [104] in the body. Or, as quantum emitters have been observed in GaN [106], these cavities could be coupled to colour centres to enhance the emission of light and could be used for quantum communications and quantum information processing [105]. These device suggestions also apply to GaN triangular nanobeam PICs. Other hard masks could also be studied in GaN on sapphire device processing, and may be fruitful. For example, the negative-tone resist HSQ forms a glass when exposed by an electron beam and acts as a hard mask. Using this resist (or equivalent) would allow the device design to be written directly into the mask, removing the lift-off process and lead to more direct process control, and quicker fabrication due to fewer fabrication steps.

In order to fully realise the potential of GaN PICs, devices which use GaN's Pockel's effect and nonlinear optical effects should be made. Second harmonic generation could be demonstrated in GaN on sapphire, like on GaN on silicon in Ref. [36]. The electrical manipulation of light in GaN PICs could be demonstrated using the Pockel's effect in circuits with optical switching, fabricating networks of devices similar to the one simulated in Ref. [68], or the Mach-Zehnder modulator simulated in Ref [69]. Such devices could be used for optical signal processing, such as in optical interconnects. These devices could again be demonstrated in a ridge GaN on sapphire platform, or a triangular nanobeam platform.

The results in chapter 5 of this thesis regarding GaN triangular nanobeams are all results from simulations. GaN triangular nanobeam waveguides could be fabricated, and the properties of the fundamental modes e.g. effective index could be measured and compared to the values we have calculated in this thesis. This type of measurement could be done on a wide range of nanobeams widths and etch angles, to thoroughly compare them to our simulated values. This type of experiment could also verify the minimum nanobeam width needed for confinement of 400 nm, the nanobeam widths at which the nanobeam supports higher modes, and could confirm the degeneracy of the TE

and TM modes for equilateral cross-section nanobeam waveguides. If we were to fabricate triangular nanobeams, we would recommend using angled FIB etching with a rotating stage, due to the ease at which etch angle can be adjusted, and the high degree of etch uniformity. Different geometries of supporting structures such as conical pads, square, or triangular pads could also be investigated and compared. Bends in triangular nanobeams could be investigated in a similar way, with the minimum sizes needed for structural strength balanced with losses. Efficient/minimum bend radii of triangular nanobeams could also be investigated.

In chapter 6, we have shown through simulations that triangular GaN nanobeams can form PCNCs with high Qs. As such, they have the potential to create strong light-matter interactions with a small device footprint. However, there is currently no literature on fabricated triangular GaN PCNCs; the Q factor of triangular GaN PCNCs could be measured, and compared to our simulation results. To take this suggestion further, PCNCs could be fabricated with an increasing number of mirror periods N, and the saturation of Q with N could be measured. The comparison between the value that Q saturates at in these fabricated devices and the simulation results in this thesis would also give an indication of the amount of loss caused by fabrication in these devices. Different cavity designs could also be simulated and fabricated, such as GaN cavities which use holes as mirrors, instead of modulations in width. A more in-depth investigation into the impact of loss (on Q) in a physical device could also take place. This would require fabricating a large number of PCNCs, with varying degrees of imperfections in device geometry systematically implemented. This could be achieved by adding 'roughness' to the mask design of the devices, to varying degrees. By having a systematically increasing roughness and therefore scattering loss, the Q factor as a function of this loss can be measured, and compared to our results.

The reason behind the oscillation in Q with N once Q has saturated is not obvious. It would be interesting to investigate this behaviour further by simulating DBR cavities with smaller intervals in N around this region, and observe this periodic behaviour in more detail. It would also be interesting to study the effect of the length of the centre cavity spacer on Q. Ref. [107] simulated different cavity lengths, but only over a span of 40 nm. We have simulated different cavity lengths in this thesis, but only for cavities which were not resonating. It would be interesting to see the impact of the central cavity length on Q over a wider range of lengths, and on a resonating cavity.

As our attempt at apodising of the cavity mode and increasing Q was not successful, this is an obvious avenue for future work. As we followed the design procedure layed out in Ref. [107], which we

believe to be sound, a systematic approach to evaluating our design is needed. As we have verified that the length of the central cavity spacer is not the source of the problem, we believe the γ profile must likely be the cause. In order to determine the root of the problem with the γ profile, we would start with the constant γ profile at the Bragg condition that we know achieves resonance with a $Q \sim 4000$ (for $N \geq 90$) . We would then adjust the mirror profile slightly, perhaps starting with just one change in FF halfway along the nanobeam, and observe the behaviour of the mode. We would then gradually adjust the γ profile and observe how this effects the cavity mode. At some point, either gradually or abruptly, the cavity will stop resonating, and we can analyse this point to determine the cause. Ref. [107] also states the need for a quadratically tapered filling fraction. Although Ref. [111] and [113] state that a gradual γ profile is required, and the FF profile need not be Gaussian, it would still be an avenue worth pursuing, to eliminate this as a cause of our lack of resonance.

Chapter 8

Appendix

8.1 E-beam Practical User's Guide/Crash Course

In this section, we will outline the procedure for writing using electron-beam lithography. Although the lithography process engineer in your cleanroom will give you training, it is still useful to provide a comprehensive 'how-to' guide of what to expect. As this is one of the most technically demanding (and expensive) tools to use and can be overwhelming, we wish people to be able to make the most of their time using the tool. Remember, as areas on the sample are being exposed in the order of nanometers, a high degree of precision, accuracy, and cleanliness is necessary.

Before loading the sample into the load lock (but after mounting onto the carrier), make a small mark/scratch in the resist on the sample in one of the corners using a (clean) diamond scribe, away from the intended pattern area. Such a scratch provides features to initially focus on with a similar depth to the intended write field. Once the sample has been loaded, find the corner the mark/scratch was made (taking care not to move the beam over the centre of the surface of the sample - stick to skirting around the edges of the chip) and magnify it to an appropriate degree (a field of view of around a couple of microns) and focus on it. Once in focus, magnify further and focus again. Repeat this until a high degree magnification is achieved - roughly until features smaller than 100 nm can be resolved. If a high resolution is not possible just yet, it may be an issue with astigmatism/stigmation. The stigmation of the beam (controlled by the appropriately named stigmator - a set of coils which produce a magnetic field) describes the shape of the beam. A perfect beam would have a Gaussian profile with circular symmetry, but this is not often found on the first try, and must be adjusted to.

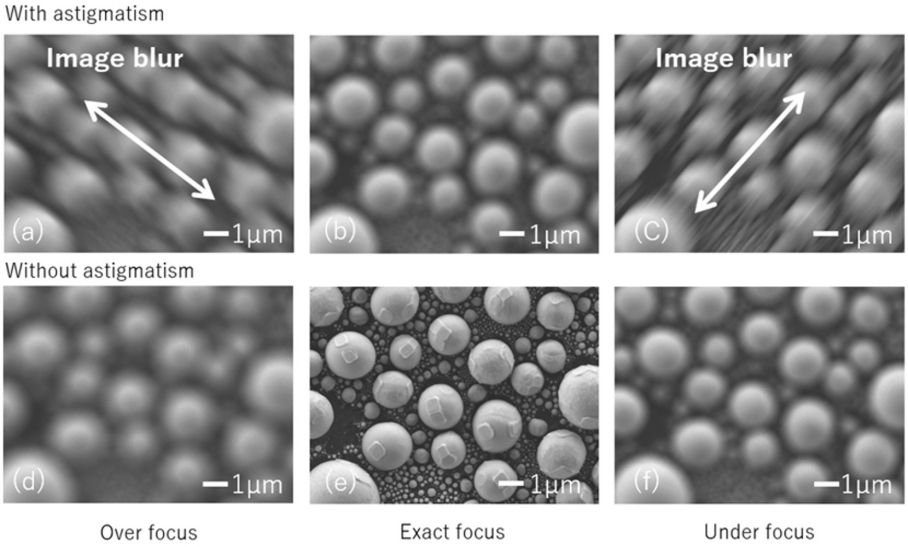

Figure 8.1: Illustration of beam focusing from reference [116], a tool manufacturer, with (a, b & c) and without (d, e & f) astigmatism. With astigmatism, overfocus (a) and underfocus (c) blur in orthogonal directions. Without astigmatism, image blur is isotropic, and not smeared. When astigmatism is corrected, the image in focus is clearer and more detailed.

To determine the level of stigmation (and therefore the level of correction needed), perform a "focus wobble" by oscillating the beam in and out of focus (some e-line tools have a focus wobble function to assist with this). If the stigmation needs correcting, then the image will blur or 'smear' in the horizontal direction, vertical direction, or a mixture of both, seen in the images in figure 8.1, which have been taken from an equipment manufacturer [116] (for further reading, reference [116] also describes how the magnetic field in the stigmator is controlled, including schematics). Adjust the horizontal and vertical stigmation individually to reduce this smearing. Once the smearing has been corrected, focus the beam again - with any luck, the image is clearer. Repeat this process several times until there is no smearing in the image with a focus wobble, and the image blurs isotropically when out of focus.

A final beam focus shortly before the write is advised, which can be carried out by using a 'burn dot'. By changing the electron beam from an imaging raster scan to a 'point' or spot, a small area of resist can be exposed by the beam. This exposed resist region should be visible using the SEM after an exposure time of at least ten seconds for the first dot. Once a dot has been 'burnt', focus on it until a high degree of resolution has been achieved. Then, burn another dot close to the first one, this time for a shorter period of time, approximately five seconds. This dot will likely be smaller than the first one, as the beam is now better in focus. Increase the beam magnification before focusing if needed. Repeat this process several times, considering the feature size of the device compared to the size of the

burn dot. The shape of the burn dot will indicate the shape of the beam that will write your device. We recommend using burn dots to focus close to the intended device, due to the fact that this resist will be similar to the resist in the device region. However, do not burn dots in the device region itself, as this will likely affect the writing.

8.2 When Lift-Off Goes Wrong

Figure 8.2 shows micrographs demonstrating nickel lift-off which has 'gone wrong'. This figure shows a range of issues that may occur with a lift-off process. Large sections of the nickel have delaminated from the GaN in the device regions, with (sections of) waveguides missing from the design/surface, and these device regions are therefore rendered obselete. Also visible is nickel which should have been removed by the acetone, but has not - this nickel was both in large pieces, as shown, or as extra portions of nickel still attached to the waveguide sections - this extra width, when etched, would have a very large mismatch to the propagating optical mode, and would incur large losses. What can also be seen by the roughly circular smudges or marks, is residual acetone/IPA left on the sample surface. This is not likely to be detrimental to the etch, and can be burnt off using an oxygen plasma etch. The results shown in figure 8.2 were the result of using a PMMA/MMA bilayer for the lift-off, with 150 nm of nickel deposited. Switching to a simpler resist recipe of only PMMA as well as a thinner layer of nickel (30 nm) helped with the lift-off process, and led to a higher device yield.

8.3 Tips for Nickel Lift-Off

Here are some tips in case the reader is embarking on a nickel lift-off process: soak the chip in warm (50°C) acetone for approximately 15 minutes. Then, agitate the chip in the acetone to remove nickel from the chip. We found that leaving the chip stationary in the acetone for the allotted time (15 minutes) before agitating the chip had better results than agitating from the offset. Examine, and if nickel is still present, repeat this process. We found that warm acetone was better at removing nickel than room/ambient temperature acetone. We recommend covering the top of your beaker/dish with some form of (clean) lid - an upside down dish works, preventing the acetone from evaporating and keeping the solution warm - the boiling point of acetone is 56°C [117].

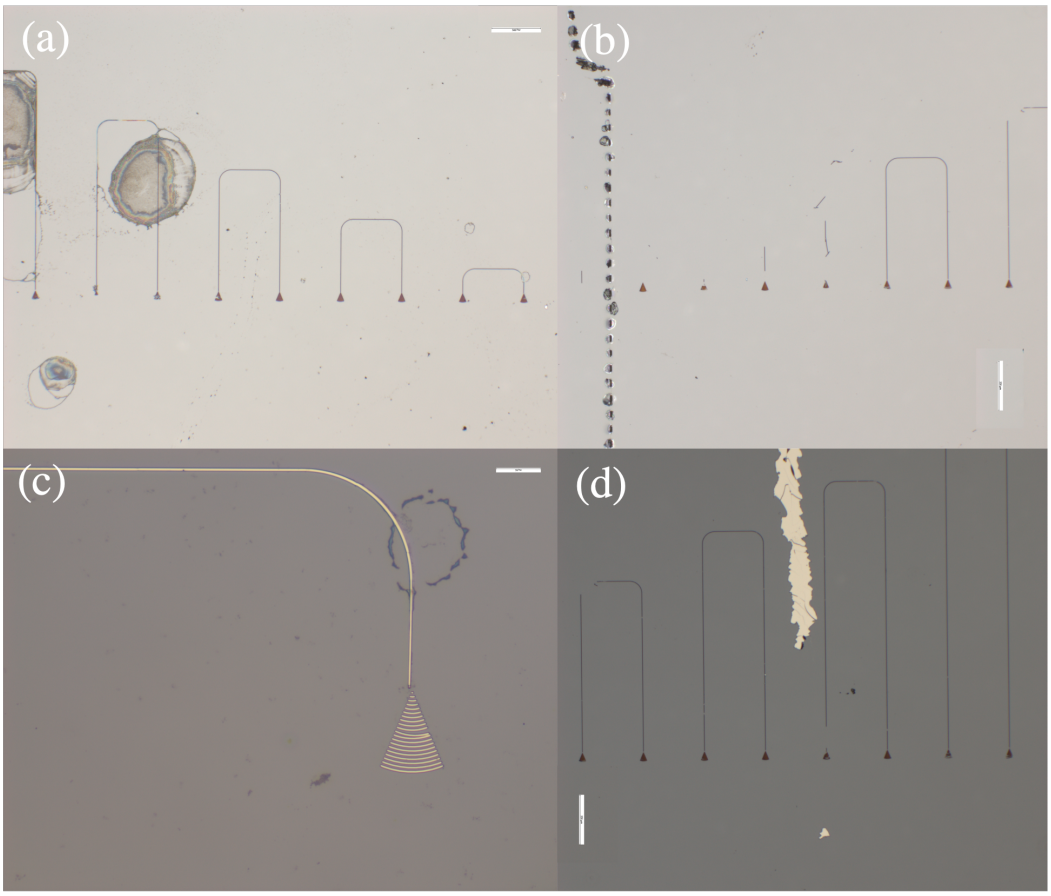

Figure 8.2: Optical micrographs post-lift-off using PMMA/MMA bilayer recipe. These images show delamination of devices, nickel not being removed, and residual solvent marks.

References

[1] C. Baack and G. Walf, "Photonics in future telecommunications," *Proceedings of the IEEE*, vol. 81, no. 11, pp. 1624–1632, 1993. DOI: 10.1109/5.247733.

[2] J. Doylend and A. Knights, "The evolution of silicon photonics as an enabling technology for optical interconnection," *Laser & Photonics Reviews*, vol. 6, no. 4, pp. 504–525, 2012. DOI: 10.1002/lpor.201100023.

[3] L. Eldada, "Optical communication components," *Review of Scientific Instruments*, vol. 75, no. 3, pp. 575–593, 2004. DOI: 10.1063/1.1647701.

[4] S. Fathpour and B. Jalali, *Silicon Photonics for Telecommunications and Biomedicine*. CRC Press, 2011, ISBN: 978-1-4398-0637-1.

[5] R. Katti and S. Prince, "A survey on role of photonic technologies in 5G communication systems," *Photonic Network Communications*, vol. 38, no. 2, pp. 185–205, 2019. DOI: 10.1007/s11107-019-00856-w.

[6] K. Yamada, T. Tsuchizawa, H. Nishi, *et al.*, "High-performance silicon photonics technology for telecommunications applications," *Science and Technology of Advanced Materials*, vol. 15, no. 2, p. 024 603, 2014. DOI: 10.1088/1468-6996/15/2/024603.

[7] *Photonics in Healthcare, spie.org*, 2020. [Online]. Available: https://spie.org/news/photonics-in-healthcare.

[8] E. Damulira, M. N. S. Yusoff, A. F. Omar, and N. H. Mohd Taib, "A Review: Photonic Devices Used for Dosimetry in Medical Radiation," *Sensors*, vol. 19, no. 10, p. 2226, 2019. DOI: 10.3390/s19102226.

[9] C. Dhote, A. Singh, and S. Kumar, "Silicon Photonics Sensors for Biophotonic Applications—A Review," *IEEE Sensors Journal*, vol. 22, no. 19, pp. 18 228–18 239, 2022. DOI: 10.1109/JSEN.2022.3199663.

[10] S. C. Sajan, A. Singh, P. K. Sharma, and S. Kumar, "Silicon Photonics Biosensors for Cancer Cells Detection—A Review," *IEEE Sensors Journal*, vol. 23, no. 4, pp. 3366–3377, 2023. DOI: 10.1109/JSEN.2023.3235920.

[11] X. Wu and Q. Guo, "Bioresorbable Photonics: Materials, Devices and Applications," *Photonics*, vol. 8, no. 7, p. 235, 2021. DOI: 10.3390/photonics8070235.

[12] L. Afsah-Hejri, E. Akbari, A. Toudeshki, T. Homayouni, A. Alizadeh, and R. Ehsani, "Terahertz spectroscopy and imaging: A review on agricultural applications," *Computers and Electronics in Agriculture*, vol. 177, p. 105 628, 2020. DOI: 10.1016/j.compag.2020.105628.

[13] A. Massaro, N. Savino, and A. Galiano, "Agri-Photonics in Precision Agriculture," in *2020 22nd International Conference on Transparent Optical Networks (ICTON)*, 2020, pp. 1–4. DOI: 10.1109/ICTON51198.2020.9203077.

[14] S. Mathanker, P. Weckler, and N. Wang, "Terahertz (THz) Applications in Food and Agriculture: A Review," *Transactions of the ASABE*, pp. 1213–1226, 2013. DOI: 10.13031/trans.56.9390.

[15] J. Y. Tan, P. J. Ker, K. Y. Lau, M. A. Hannan, and S. G. H. Tang, "Applications of Photonics in Agriculture Sector: A Review," *Molecules*, vol. 24, no. 10, p. 2025, 2019. DOI: 10.3390/molecules24102025.

[16] C. Adamopoulos, P. Zarkos, S. Buchbinder, *et al.*, "Lab-on-Chip for Everyone: Introducing an Electronic-Photonic Platform for Multiparametric Biosensing Using Standard CMOS Processes," *IEEE Open Journal of the Solid-State Circuits Society*, vol. 1, pp. 198–208, 2021. DOI: 10.1109/OJSSCS.2021.3118336.

[17] *Barcode scanning — Hamamatsu Photonics*. [Online]. Available: https://www.hamamatsu.com/us/en/applications/industrial-equipment/barcode-scanning.html.

[18] J. K. Doylend and S. Gupta, "An overview of silicon photonics for LIDAR," in *Silicon Photonics XV*, vol. 11285, SPIE, 2020, pp. 109–115. DOI: 10.1117/12.2544962.

[19] B. Kress and T. Starner, "A review of head-mounted displays (HMD) technologies and applications for consumer electronics," in *Photonic Applications for Aerospace, Commercial, and Harsh Environments IV*, vol. 8720, SPIE, 2013, pp. 62–74. DOI: 10.1117/12.2015654.

[20] X. Sun, L. Zhang, Q. Zhang, and W. Zhang, "Si Photonics for Practical LiDAR Solutions," *Applied Sciences*, vol. 9, no. 20, p. 4225, 2019. DOI: 10.3390/app9204225.

[21] X. Zhu, M. Keshavarz Hedayati, S. Raza, U. Levy, N. A. Mortensen, and A. Kristensen, "Digital resonant laser printing: Bridging nanophotonic science and consumer products," *Nano Today*, vol. 19, pp. 7–10, 2018. DOI: 10.1016/j.nantod.2017.10.002.

[22] J. L. O'Brien, A. Furusawa, and J. Vučković, "Photonic quantum technologies," *Nature Photonics*, vol. 3, no. 12, pp. 687–695, 2009. DOI: 10.1038/nphoton.2009.229.

[23] X. Chen, Z. Fu, Q. Gong, and J. Wang, "Quantum entanglement on photonic chips: A review," *Advanced Photonics*, vol. 3, no. 6, p. 064 002, 2021. DOI: 10.1117/1.AP.3.6.064002.

[24] F. Flamini, N. Spagnolo, and F. Sciarrino, "Photonic quantum information processing: A review," *Reports on Progress in Physics*, vol. 82, no. 1, p. 016 001, 2018. DOI: 10.1088/1361-6633/aad5b2.

[25] S. Slussarenko and G. J. Pryde, "Photonic quantum information processing: A concise review," *Applied Physics Reviews*, vol. 6, no. 4, p. 041 303, 2019. DOI: 10.1063/1.5115814.

[26] M. Soler, A. Scholtz, R. Zeto, and A. M. Armani, "Engineering photonics solutions for COVID-19," *APL Photonics*, vol. 5, no. 9, p. 090 901, 2020. DOI: 10.1063/5.0021270.

[27] J. Wang, F. Sciarrino, A. Laing, and M. G. Thompson, "Integrated photonic quantum technologies," *Nature Photonics*, vol. 14, no. 5, pp. 273–284, 2020. DOI: 10.1038/s41566-019-0532-1.

[28] J. Wang and Y. Long, "On-chip silicon photonic signaling and processing: A review," *Science Bulletin*, vol. 63, no. 19, pp. 1267–1310, 2018. DOI: 10.1016/j.scib.2018.05.038.

[29] D. Dai, L. Liu, S. Gao, D.-X. Xu, and S. He, "Polarization management for silicon photonic integrated circuits," *Laser & Photonics Reviews*, vol. 7, no. 3, pp. 303–328, 2013. DOI: 10.1002/lpor.201200023.

[30] S. Pathak, "Chapter 7 - Photonics Integrated Circuits," in *Nanoelectronics*, ser. Advanced Nanomaterials, B. K. Kaushik, Ed., Elsevier, 2019, pp. 219–270, ISBN: 978-0-12-813353-8. DOI: 10.1016/B978-0-12-813353-8.00008-7.

[31] J. Wang, "Chip-scale optical interconnects and optical data processing using silicon photonic devices," *Photonic Network Communications*, vol. 31, no. 2, pp. 353–372, 2016. DOI: 10.1007/s11107-015-0525-z.

[32] W. Bogaerts, D. Taillaert, B. Luyssaert, *et al.*, "Basic structures for photonic integrated circuits in Silicon-on-insulator," *Optics Express*, vol. 12, no. 8, pp. 1583–1591, 2004. DOI: 10.1364/OPEX.12.001583.

[33] J. Sun, E. Timurdogan, A. Yaacobi, *et al.*, "Large-Scale Silicon Photonic Circuits for Optical Phased Arrays," *IEEE Journal of Selected Topics in Quantum Electronics*, vol. 20, no. 4, pp. 264–278, 2014. DOI: 10.1109/JSTQE.2013.2293316.

[34] R. Nagarajan, C. Joyner, R. Schneider, *et al.*, "Large-scale photonic integrated circuits," *IEEE Journal of Selected Topics in Quantum Electronics*, vol. 11, no. 1, pp. 50–65, 2005. DOI: 10.1109/JSTQE.2004.841721.

[35] V. Dolores-Calzadilla, B. Romeira, F. Pagliano, *et al.*, "Waveguide-coupled nanopillar metal-cavity light-emitting diodes on silicon," *Nature Communications*, vol. 8, no. 1, p. 14 323, 2017. DOI: 10.1038/ncomms14323.

[36] C. Xiong, W. Pernice, K. K. Ryu, *et al.*, "Integrated GaN photonic circuits on silicon (100) for second harmonic generation," *Optics Express*, vol. 19, no. 11, pp. 10 462–10 470, 2011. DOI: 10.1364/OE.19.010462.

[37] F. Kish, V. Lal, P. Evans, *et al.*, "System-on-Chip Photonic Integrated Circuits," *IEEE Journal of Selected Topics in Quantum Electronics*, vol. 24, no. 1, pp. 1–20, 2018. DOI: 10.1109/JSTQE.2017.2717863.

[38] W. Bogaerts, D. Pérez, J. Capmany, *et al.*, "Programmable photonic circuits," *Nature*, vol. 586, no. 7828, pp. 207–216, 2020. DOI: 10.1038/s41586-020-2764-0.

[39] A. Mohanty, Q. Li, M. A. Tadayon, *et al.*, "Reconfigurable nanophotonic silicon probes for sub-millisecond deep-brain optical stimulation," *Nature Biomedical Engineering*, vol. 4, no. 2, pp. 223–231, 2020. DOI: 10.1038/s41551-020-0516-y.

[40] J. Campos, R. Mendes, J. Quaresma, *et al.*, "Detonation Measurements Using Single Optical Fibers," Proc. of the 45th International Annual Conference of ICT, 2014.

[41] B. Wohlfeil, G. R. Mehrpoor, A. Dochhan, D. Rafique, M. Eiselt, and J.-P. Elbers, "Photonic Integrated Circuits for Data Center Interconnects," in *2018 Photonics in Switching and Computing (PSC)*, Limassol, Cyprus: IEEE, 2018, pp. 1–3. DOI: 10.1109/PS.2018.8751412.

[42] J. M. Morales, P. Cho, J. R. Bickford, P. M. Pellegrino, G. Leake, and M. L. Fanto, "Development of army relevant wearable Photonic Integrated Circuit (PIC) biosensors," in *Chemical, Biological, Radiological, Nuclear, and Explosives (CBRNE) Sensing XXII*, vol. 11749, SPIE, 2021, pp. 98–106. DOI: 10.1117/12.2587098.

[43] *Bioptx™ Biosensing Band — Rockley: The Future of Health Insights*, Rockley Photonics. [Online]. Available: https://rockleyphotonics.com/bioptx-band/.

[44] M. J. Burek, Y. Chu, M. S. Z. Liddy, *et al.*, "High quality-factor optical nanocavities in bulk single-crystal diamond," *Nature Communications*, vol. 5, no. 1, p. 5718, 2014. DOI: 10.1038/ncomms6718.

[45] N. V. Triviño, R. Butté, J.-F. Carlin, and N. Grandjean, "Continuous Wave Blue Lasing in III-Nitride Nanobeam Cavity on Silicon," *Nano Letters*, vol. 15, no. 2, pp. 1259–1263, 2015. DOI: 10.1021/nl504432d.

[46] S. Nakamura, T. Mukai, and M. Senoh, "Candela-class high-brightness InGaN/AlGaN double-heterostructure blue-light-emitting diodes," *Applied Physics Letters*, vol. 64, no. 13, pp. 1687–1689, 1994. DOI: 10.1063/1.111832.

[47] I. A. I. Akasaki and H. A. H. Amano, "Crystal Growth and Conductivity Control of Group III Nitride Semiconductors and Their Application to Short Wavelength Light Emitters," *Japanese Journal of Applied Physics*, vol. 36, no. 9R, p. 5393, 1997. DOI: 10.1143/JJAP.36.5393.

[48] G. Yu, G. Wang, H. Ishikawa, *et al.*, "Optical properties of wurtzite structure GaN on sapphire around fundamental absorption edge (0.78–4.77 eV) by spectroscopic ellipsometry and the optical transmission method," *Applied Physics Letters*, vol. 70, no. 24, pp. 3209–3211, 1997. DOI: 10.1063/1.119157.

[49] *On web of science (www.webofscience.com), there are 8823 papers for gan on sapphire substrates, 4289 for gan on silicon substrates (as of 17/1/24).*

[50] H. G. Bach, J. Krauser, H. P. Nolting, R. A. Logan, and F. K. Reinhart, "Electro-optical light modulation in InGaAsP/InP double heterostructure diodes," *Applied Physics Letters*, vol. 42, no. 8, pp. 692–694, 1983. DOI: 10.1063/1.94075.

[51] C.-A. Berseth, C. Wuethrich, and F. K. Reinhart, "The electro-optic coefficients of GaAs: Measurements at 1.32 and 1.52 m and study of their dispersion between 0.9 and 10 m," *Journal of Applied Physics*, vol. 71, no. 6, pp. 2821–2825, 1992. DOI: 10.1063/1.351011.

[52] X.-C. Long, R. A. Myers, S. R. J. Brueck, R. Ramer, K. Zheng, and S. D. Hersee, "GaN linear electro-optic effect," *Applied Physics Letters*, vol. 67, no. 10, pp. 1349–1351, 1995. DOI: 10.1063/1.115547.

[53] G. T. Reed, "The optical age of silicon," *Nature*, vol. 427, no. 6975, pp. 595–596, 2004. DOI: 10.1038/427595b.

[54] M. Lipson, "Silicon photonics: The optical spice rack," *Electronics Letters*, vol. 45, no. 12, pp. 576–578, 2009. DOI: 10.1049/el.2009.1232.

[55] G. Z. Mashanovich, M. M. Milošević, M. Nedeljkovic, *et al.*, "Low loss silicon waveguides for the mid-infrared," *Optics Express*, vol. 19, no. 8, pp. 7112–7119, 2011. DOI: 10.1364/OE.19.007112.

[56] Y. Zheng, C. Sun, B. Xiong, *et al.*, "Integrated Gallium Nitride Nonlinear Photonics," *Laser & Photonics Reviews*, vol. 16, no. 1, p. 2 100 071, 2022. DOI: 10.1002/lpor.202100071.

[57] C. P. Dietrich, A. Fiore, M. G. Thompson, M. Kamp, and S. Höfling, "GaAs integrated quantum photonics: Towards compact and multi-functional quantum photonic integrated circuits," *Laser & Photonics Reviews*, vol. 10, no. 6, pp. 870–894, 2016. DOI: 10.1002/lpor.201500321.

[58] J. Wang, A. Santamato, P. Jiang, *et al.*, "Gallium arsenide (GaAs) quantum photonic waveguide circuits," *Optics Communications*, Special Issue on Nonlinear Quantum Photonics, vol. 327, pp. 49–55, 2014. DOI: 10.1016/j.optcom.2014.02.040.

[59] S. Arafin and L. A. Coldren, "Advanced InP Photonic Integrated Circuits for Communication and Sensing," *IEEE Journal of Selected Topics in Quantum Electronics*, vol. 24, no. 1, pp. 1–12, 2018. DOI: 10.1109/JSTQE.2017.2754583.

[60] N. S. N. Suzuki and N. I. N. Iizuka, "Feasibility Study on Ultrafast Nonlinear Optical Properties of 1.55-μm Intersubband Transition in AlGaN/GaN Quantum Wells," *Japanese Journal of Applied Physics*, vol. 36, no. 8A, p. L1006, 1997. DOI: 10.1143/JJAP.36.L1006.

[61] N. Iizuka, Kaneko, Kei, and Suzuki, Nobeo, "Sub-picosecond modulation by intersubband transition in ridge waveguide with GaN/AlN quantum wells," *Electronics Letters*, vol. 40, no. 15, pp. 962–963, 2004. DOI: 10.1049/el:20045434.

[62] N. Iizuka, K. Kaneko, and N. Suzuki, "Sub-picosecond all-optical gate utilizing GaN intersubband transition," *Optics Express*, vol. 13, no. 10, p. 3835, 2005. DOI: 10.1364/OPEX.13.003835.

[63] N. Iizuka, K. Kaneko, and N. Suzuki, "Polarization dependent loss in III-nitride optical waveguides for telecommunication devices," *Journal of Applied Physics*, vol. 99, no. 9, p. 093 107, 2006. DOI: 10.1063/1.2195422.

[64] N. Iizuka, K. Kaneko, and N. Suzuki, "All-optical switch utilizing intersubband transition in GaN quantum wells," *IEEE Journal of Quantum Electronics*, vol. 42, no. 8, pp. 765–771, 2006. DOI: 10.1109/JQE.2006.878189.

[65] Y. Li, A. Bhattacharyya, C. Thomidis, T. D. Moustakas, and R. Paiella, "Nonlinear optical waveguides based on near-infrared intersubband transitions in GaN/AlN quantum wells," *Optics Express*, vol. 15, no. 9, pp. 5860–5865, 2007. DOI: 10.1364/OE.15.005860.

[66] W. Fan, M. Ludwig, I. Rousseau, *et al.*, "Supercontinua from integrated gallium nitride waveguides," *Optica*, vol. 11, no. 8, pp. 1175–1181, 2024. DOI: 10.1364/OPTICA.528341.

[67] A. W. Bruch, C. Xiong, B. Leung, M. Poot, J. Han, and H. X. Tang, "Broadband nanophotonic waveguides and resonators based on epitaxial GaN thin films," *Applied Physics Letters*, vol. 107, no. 14, p. 141 113, 2015. DOI: 10.1063/1.4933093.

[68] A. Stolz, L. Considine, E. Dogheche, D. Decoster, and D. Pavlidis, "Prospective for Gallium Nitride-Based Optical Waveguide Modulators," *IEICE Transactions on Electronics*, vol. 95, pp. 1363–1368, 2012. DOI: 10.1587/transele.E95.C.1363.

[69] R. W. Purnamaningsih, N. R. Poespawati, I. Saraswati, and E. Dogheche, "Design of GaN based optical modulator with Mach-Zehnder interferometer structure," vol. 13, 2014.

[70] L. Liu and J. H. Edgar, "Substrates for gallium nitride epitaxy," *Materials Science and Engineering: R: Reports*, vol. 37, no. 3, pp. 61–127, 2002. DOI: 10.1016/S0927-796X(02)00008-6.

[71] C. Xiong, W. Pernice, C. Schuck, and H. X. Tang, "Integrated Photonic Circuits in Gallium Nitride and Aluminum Nitride," *International Journal of High Speed Electronics and Systems*, vol. 23, no. 01n02, p. 1 450 001, 2014. DOI: 10.1142/S0129156414500013.

[72] T. Sekiya, T. Sasaki, and K. Hane, "GaN freestanding waveguides on Si substrate for Si/GaN hybrid photonic integration," in *2015 Transducers - 2015 18th International Conference on Solid-State Sensors, Actuators and Microsystems (TRANSDUCERS)*, 2015, pp. 2057–2060. DOI: 10.1109/TRANSDUCERS.2015.7181361.

[73] N. Niu, A. Woolf, D. Wang, *et al.*, "Ultra-low threshold gallium nitride photonic crystal nanobeam laser," *Applied Physics Letters*, vol. 106, no. 23, p. 231 104, 2015. DOI: 10.1063/1.4922211.

[74] W. Cai, C. Qin, S. Zhang, J. Yuan, F. Zhang, and Y. Wang, "Monolithic photonic integrated circuit with a GaN-based bent waveguide," *Journal of Micromechanics and Microengineering*, vol. 28, no. 6, p. 065 003, 2018. DOI: 10.1088/1361-6439/aab21d.

[75] F. Tabataba-Vakili, L. Doyennette, C. Brimont, *et al.*, "Blue Microlasers Integrated on a Photonic Platform on Silicon," *ACS Photonics*, vol. 5, no. 9, pp. 3643–3648, 2018. DOI: 10.1021/acsphotonics.8b00542.

[76] *We used the commercially available simulation software ANSYS Lumerical for simulations.* [Online]. Available: https://www.lumerical.com/.

[77] K. Yee, "Numerical solution of initial boundary value problems involving maxwell's equations in isotropic media," *IEEE Transactions on Antennas and Propagation*, vol. 14, no. 3, pp. 302–307, 1966. DOI: 10.1109/TAP.1966.1138693.

[78] Z. Zhu and T. G. Brown, "Full-vectorial finite-difference analysis of microstructured optical fibers," *Optics Express*, vol. 10, no. 17, pp. 853–864, 2002. DOI: 10.1364/OE.10.000853.

[79] S. DiBartolomeo, *All About Calma's GDSII Stream File Format.* [Online]. Available: https://www.artwork.com/gdsii/gdsii/.

[80] P. Androvitsaneas, R. N. Clark, M. Jordan, *et al.*, "Direct-write projection lithography of quantum dot micropillar single photon sources," *Applied Physics Letters*, vol. 123, no. 9, p. 094 001, 2023. DOI: 10.1063/5.0155968.

[81] *Scanning Electron Microscope — Apreo 2 SEM — Thermo Fisher Scientific - UK.* [Online]. Available: https://www.thermofisher.com/uk/en/home/electron-microscopy/products/scanning-electron-microscopes/apreo-sem.html#resources.

[82] S. Hamed Mirsadeghi, E. Schelew, and J. F. Young, "Photonic crystal slot-microcavity circuit implemented in silicon-on-insulator: High Q operation in solvent without undercutting," *Applied Physics Letters*, vol. 102, no. 13, p. 131 115, 2013. DOI: 10.1063/1.4799963.

[83] F. C.-P. Massabuau, P. H. Griffin, H. P. Springbett, *et al.*, "Dislocations as channels for the fabrication of sub-surface porous GaN by electrochemical etching," *APL Materials*, vol. 8, no. 3, p. 031 115, 2020. DOI: 10.1063/1.5142491.

[84] L. O'Faolain, S. A. Schulz, D. M. Beggs, *et al.*, "Loss engineered slow light waveguides," *Optics Express*, vol. 18, no. 26, pp. 27 627–27 638, 2010. DOI: 10.1364/OE.18.027627.

[85] S. A. Smith, C. A. Wolden, M. D. Bremser, A. D. Hanser, R. F. Davis, and W. V. Lampert, "High rate and selective etching of GaN, AlGaN, and AlN using an inductively coupled plasma," *Applied Physics Letters*, vol. 71, no. 25, pp. 3631–3633, Dec. 1997, ISSN: 0003-6951. DOI: 10.1063/1.120463.

[86] I. Kaminow and T. Li, *Optical Fiber Telecommunications IV-B: Systems and Impairments*. Elsevier, May 2002, ISBN: 978-0-08-051319-5.

[87] G. P. Agrawal, *Fiber-Optic Communication Systems*. John Wiley & Sons, Feb. 2012, ISBN: 978-0-470-92282-8.

[88] X. Jiang, H. Wu, and D. Dai, "Low-loss and low-crosstalk multimode waveguide bend on silicon," *Optics Express*, vol. 26, no. 13, pp. 17 680–17 689, Jun. 2018, Publisher: Optica Publishing Group, ISSN: 1094-4087. DOI: 10.1364/OE.26.017680.

[89] A. S. Barker and M. Ilegems, "Infrared Lattice Vibrations and Free-Electron Dispersion in GaN," *Physical Review B*, vol. 7, no. 2, pp. 743–750, 1973. DOI: 10.1103/PhysRevB.7.743.

[90] I. H. Malitson, "Refraction and Dispersion of Synthetic Sapphire," *JOSA*, vol. 52, no. 12, pp. 1377–1379, 1962. DOI: 10.1364/JOSA.52.001377.

[91] H. Chen, H. Fu, X. Huang, *et al.*, "Low loss GaN waveguides at the visible spectral wavelengths for integrated photonics applications," *Optics Express*, vol. 25, no. 25, pp. 31 758–31 773, 2017. DOI: 10.1364/OE.25.031758.

[92] *Kyma Technologies*. [Online]. Available: https://www.kymatech.com.

[93] R. D. Driver, G. M. Leskowitz, L. E. Curtiss, D. E. Moynihan, and L. B. Vacha, "The Characterization of Infrared Transmitting Optical Fibers," *MRS Online Proceedings Library (OPL)*, vol. 172, p. 169, 1989, Publisher: Cambridge University Press. DOI: 10.1557/PROC-172-169.

[94] G. P. Gough, A. D. Sobiesierski, S. Shabbir, *et al.*, "Faraday-cage-assisted etching of suspended gallium nitride nanostructures," *AIP Advances*, vol. 10, no. 5, p. 055 319, 2020. DOI: 10.1063/5.0007947.

[95] H. A. Atikian, P. Latawiec, M. J. Burek, *et al.*, "Freestanding nanostructures via reactive ion beam angled etching," *APL Photonics*, vol. 2, no. 5, 2017. DOI: 10.1063/1.4982603.

[96] S. Majety, V. A. Norman, P. Saha, A. H. Rubin, S. Dhuey, and M. Radulaski, *Wafer-Scale Integration of Freestanding Photonic Devices with Color Centers in Silicon Carbide*, 2024. DOI: 10.48550/arXiv.2405.07498.

[97] P. Latawiec, M. J. Burek, Y.-I. Sohn, and M. Lončar, "Faraday cage angled-etching of nanostructures in bulk dielectrics," *Journal of Vacuum Science & Technology B, Nanotechnology and Microelectronics: Materials, Processing, Measurement, and Phenomena*, vol. 34, no. 4, p. 041 801, 2016. DOI: 10.1116/1.4944854.

[98] S. Majety, P. Saha, Z. Kekula, S. Dhuey, and M. Radulaski, "Triangular cross-section beam splitters in silicon carbide for quantum information processing," *MRS Communications*, 2024. DOI: 10.1557/s43579-024-00557-0.

[99] M. J. Burek, N. P. de Leon, B. J. Shields, *et al.*, "Free-Standing Mechanical and Photonic Nanostructures in Single-Crystal Diamond," *Nano Letters*, vol. 12, no. 12, pp. 6084–6089, 2012. DOI: 10.1021/nl302541e.

[100] M. J. Burek, Y. Chu, M. S. Z. Liddy, *et al.*, "High quality-factor optical nanocavities in bulk single-crystal diamond," *Nature Communications*, vol. 5, no. 1, p. 5718, 2014. DOI: 10.1038/ncomms6718.

[101] I. Bayn, S. Mouradian, L. Li, *et al.*, "Fabrication of triangular nanobeam waveguide networks in bulk diamond using single-crystal silicon hard masks," *Applied Physics Letters*, vol. 105, no. 21, p. 211 101, 2014. DOI: 10.1063/1.4902562.

[102] S. Majety, V. A. Norman, L. Li, M. Bell, P. Saha, and M. Radulaski, "Quantum photonics in triangular-cross-section nanodevices in silicon carbide," *Journal of Physics: Photonics*, 2021. DOI: 10.1088/2515-7647/abfdca.

[103] M. J. Burek, D. Ramos, P. Patel, I. W. Frank, and M. Lončar, "Nanomechanical resonant structures in single-crystal diamond," *Applied Physics Letters*, vol. 103, no. 13, p. 131 904, 2013. DOI: 10.1063/1.4821917.

[104] D.-Q. Yang, B. Duan, X. Liu, A.-Q. Wang, X.-G. Li, and Y.-F. Ji, "Photonic Crystal Nanobeam Cavities for Nanoscale Optical Sensing: A Review," *Micromachines*, vol. 11, no. 1, p. 72, 2020. DOI: 10.3390/mi11010072.

[105] S. Majety, P. Saha, V. A. Norman, and M. Radulaski, "Quantum information processing with integrated silicon carbide photonics," *Journal of Applied Physics*, vol. 131, no. 13, p. 130 901, 2022. DOI: 10.1063/5.0077045.

[106] S. G. Bishop, J. P. Hadden, R. Hekmati, J. K. Cannon, W. W. Langbein, and A. J. Bennett, "Enhanced light collection from a gallium nitride color center using a near index-matched solid immersion lens," *Applied Physics Letters*, vol. 120, no. 11, p. 114 001, 2022. DOI: 10.1063/5.0085257.

[107] Q. Quan and M. Loncar, "Deterministic design of wavelength scale, ultra-high Q photonic crystal nanobeam cavities," *Optics Express*, vol. 19, no. 19, pp. 18 529–18 542, 2011. DOI: 10.1364/OE.19.018529.

[108] J. Joannopoulos, *Photonic Crystals Molding the Flow of Light, Second Edition*. Princeton University Press, 2008, Second Edition, ISBN: 978-0-691-12456-8.

[109] T. Asano, B.-S. Song, and S. Noda, "Analysis of the experimental Q factors (˜1 million) of photonic crystal nanocavities," *Optics Express*, vol. 14, no. 5, pp. 1996–2002, 2006. DOI: 10.1364/OE.14.001996.

[110] P. B. Deotare, M. W. McCutcheon, I. W. Frank, M. Khan, and M. Lončar, "High quality factor photonic crystal nanobeam cavities," *Appl. Phys. Lett.*, vol. 94, no. 12, p. 121 106, 2009. DOI: 10.1063/1.3107263.

[111] Y. Akahane, T. Asano, B.-S. Song, and S. Noda, "High-Q photonic nanocavity in a two-dimensional photonic crystal," *Nature*, vol. 425, no. 6961, pp. 944–947, 2003. DOI: 10.1038/nature02063.

[112] Q. Quan, P. B. Deotare, and M. Loncar, "Photonic crystal nanobeam cavity strongly coupled to the feeding waveguide," *Applied Physics Letters*, vol. 96, no. 20, p. 203 102, 2010. DOI: 10.1063/1.3429125.

[113] T. Asano and S. Noda, "Tuning holes in photonic-crystal nanocavities (reply)," *Nature*, vol. 429, no. 6988, pp. 1–2, 2004. DOI: 10.1038/nature02603.

[114] *Jp hadden, cardiff university school of engineering*. [Online]. Available: https://profiles.cardiff.ac.uk/staff/haddenj.

[115] S. A. Jewett, M. S. Makowski, B. Andrews, M. J. Manfra, and A. Ivanisevic, "Gallium nitride is biocompatible and non-toxic before and after functionalization with peptides," *Acta Biomaterialia*, vol. 8, no. 2, pp. 728–733, 2012. DOI: 10.1016/j.actbio.2011.09.038.

[116] *Stigmator — Glossary — JEOL Ltd.* [Online]. Available: https://www.jeol.com/words/semterms/20201020.111014.php#gsc.tab=0https://www.jeol.com/.

[117] *Acetone*, National Institute of Standards and Technology. [Online]. Available: https://webbook.nist.gov/cgi/cbook.cgi?ID=67-64-1&Type=IR-SPEC&Index=QUANT-IR,12.